EXPERIMENTAL CHARACTERIZATION AND NUMERICAL SIMULATION OF COMPOSITE ADHESIVE JOINTS USING THE COHESIVE ZONE MODEL APPROACH

Carlos Sarrado Molina

Universitat de Girona

Doctoral thesis

Experimental characterization and numerical simulation of composite adhesive joints using the cohesive zone model approach

Carlos Sarrado Molina

2015

Escola Politècnica Superior
Dept. d'Enginyeria Mecànica i de la Construcció Industrial

Doctoral thesis

Experimental characterization and numerical simulation of composite adhesive joints using the cohesive zone model approach

Carlos Sarrado Molina

2015

Doctorate Program in Technology

Advisors:

Dr. Albert Turon Travesa
Universitat de Girona, Spain

Dr. Josep Costa Balanzat
Universitat de Girona, Spain

Thesis submitted for the degree of Doctor of Philosophy by University of Girona

Als meus pares, Antoni i Mª Carmen,
pel seu suport incondicional

Acknowledgements

In first place, I would like to express my gratitude to my thesis advisors, Dr. Albert Turon and Dr. Josep Costa. Their wise advice in our many profitable discussions has been one of the cornerstones of this thesis, but even more valuable has been the trusting and collaborative treating they have offered me. I also acknowledge the AMADE research group for giving me the chance to collaborate in many research projects during these years and for setting up a rich environment for the development of this thesis.

During the development of this Ph.D. thesis, I have been given the opportunity to perform two research stays. I would like to acknowledge Dr. Frank A. Leone and Dr. Carlos G. Dávila from NASA Langley Research Center (Hampton, VA, USA) and Dr. Joris J. C. Remmers from the Eindhoven University of Technology (Eindhoven, The Netherlands) for giving me the opportunity to carry out these research stays and enriching the content of this thesis with useful discussions.

No vull deixar d'agrair l'amistat i el suport rebut per part dels meus companys del grup de recerca AMADE. El seu tracte afable i proper acompanyat d'un gran sentit de l'humor (cadascú a la seva manera, això sí) han fet que aquest camí hagi estat ple de bons moments dels quals en guardaré sempre un gran record.

El meu agraïment més profund el dedico a la meva família i amics. Amb tots ells he tingut la sort de gaudir de magnífiques estones i sentir-me recolzat en tot moment. En especial, vull agrair la paciència i el suport de la meva dona, l'Alba, qui té la virtut, per a mi inprescindible, de dotar-me de confiança en tot allò que faig. També vull agrair al meu germà Àlex la seva

estima i els bons moments que m'ha fet passar des de ben petit, així com al meu oncle Joan, per esperonar-me en tot moment a seguir endavant en aquest camí. Tinc clar que mai no podré agrair prou el suport que sempre m'han ofert els meus pares Antoni i Mª Carmen, així com els valors que han sabut inculcar-me i que conformen la persona que sóc avui. L'orgull que senten pel que faig aquestes poques - però imprescindibles - persones és un dels factors que més em motiven a continuar endavant. Finalment, vull recordar en aquestes línies i expressar el meu agraïment a la meva àvia Pepita. La seva ensenyança està reflectida en aquesta tesi, i el record dels seus consells de ben segur que romandrà en tots aquells que vam tenir el plaer de gaudir-ne.

Anyone who stops learning is old, whether at twenty or eighty. Anyone who keeps learning stays young.

Henry Ford

The work contained in this Ph.D. thesis was conducted in the AMADE research group (Department of Mechanical Engineering and Industrial Construction, University of Girona, Spain). The thesis was carried out under the grant AP2010-0977 from the FPU program from the Spanish *Ministerio de Educación, Cultura y Deporte* and partially funded by the Spanish Government through the *Ministerio de Economía y Competitividad* under the contracts DPI2012-34465 and MAT2012-37552-C03-03.

Part of the research presented in this thesis was developed during the Ph.D. candidate's stay at the NASA Langley Research Center (Hampton, VA, United States of America) and in the Eindhoven University of Technology (Eindhoven, The Netherlands), which were respectively funded by AMADE research group of the University of Girona and the Spanish *Ministerio de Educación, Cultura y Deporte* through the grant EST13/00902.

Publications

The present Ph.D. thesis has been prepared as a compendium of peer-reviewed journal papers, according to the regulations of Universitat de Girona. The thesis is comprised of the following five papers:

- C. Sarrado, A. Turon, J. Renart, I. Urresti. Assessment of energy dissipation during mixed-mode delamination growth using cohesive zone models. *Composites Part A - Applied Science and Manufacturing* 2012; 43(11):212836. doi:10.1016/j.compositesa.2012.07.009

  ISSN: 1359-835X, Impact factor: 3.012, ranked 2/24 in category *Materials science, composites* (1^{st} quartile) †.

- C. Sarrado, A. Turon, J. Renart, J. Costa. An experimental data reduction method for the Mixed Mode Bending test based on the J-integral approach. *Submitted to Composite Science and Technology*; 2015.

  ISSN: 0266-3538, Impact factor: 3.633, ranked 1/24 in category *Materials science, composites* (1^{st} quartile) †.

- C. Sarrado, A. Turon, J. Costa, J. Renart. On the validity of linear elastic fracture mechanics methods to measure the fracture toughness of adhesive joints. *Submitted to International Journal of Solids and Structures*; 2015.

  ISSN: 0020-7683, Impact factor: 2.035, ranked 22/139 in category *Mechanics* (1^{st} quartile) †.

- C. Sarrado, A. Turon, J. Costa, J. Renart. An experimental analysis of the fracture behavior of composite bonded joints in terms of cohesive laws. *Submitted to Composite Science and Technology*; 2015.

† According to the *2013 Journal Citation Reports*

ISSN: 0266-3538, Impact factor: 3.633, ranked 1/24 in category *Materials science, composites* (1st quartile) †.

▷ C. Sarrado, F.A. Leone, A. Turon. Finite-thickness cohesive elements for modeling thick adhesives. *Submitted to Engineering Fracture Mechanics*; 2015.

ISSN: 0013-7944, Impact factor: 1.662, ranked 43/139 in category *Mechanics* (2nd quartile) †.

Other publications that have been derived from this thesis but are not included in this document are listed below:

Journal articles

▷ B.L.V. Bak, C. Sarrado, A. Turon, J. Costa. Delamination Under Fatigue Loads in Composite Laminates: A Review on the Observed Phenomenology and Computational Methods. *Applied Mechanics Reviews* 2014; 66(6):060803. doi:10.1115/1.4027647

ISSN: 0003-6900, Impact factor: 2.000, ranked 25/139 in category *Mechanics* (1st quartile) †.

Book chapters

▷ J. Renart, J. Costa, C. Sarrado, S. Budhe, A. Turon, A. Rodríguez-Bellido (2014). Mode I fatigue behaviour and fracture of adhesively-bonded fibre-reinforced polymer (FRP) composite joints for structural repairs, In A. Vassilopoulos (Ed.), Fatigue and Fracture of Adhesively-Bonded Composite Joints (p. 121), Woodhead publishing, Elsevier.

▷ A. Turon, B. Bak, E. Lindgaard, C. Sarrado, E. Lund (2015). Interface elements for fatigue-driven delaminations in advanced composite

† According to the *2013 Journal Citation Reports*

materials, In P.P. Camanho, S. Hallett, G. Jones (Eds.), Numerical Modelling of Failure in Advanced Composite Materials, Woodhead publishing, Elsevier (*in press*).

Conference proceedings

- C. Sarrado, I. Llanos, I. Urresti, A. Turon. Reliability of cohesive zone models in terms of energy dissipation during mixed-mode delamination growth. 8th European Solid Mechanics Conference. Graz, Austria, July 2012.
- C. Sarrado, A. Turon, A. Quintanas, J. Costa. A new method for measuring cohesive lengths and mixed-mode cohesive laws using digital image correlation. IV ECCOMAS Thematic Conference on the Mechanical Response of Composites. Azores, Portugal, September 2013.
- F.A. Leone, C. Sarrado, C.G. Dávila, D. Girolamo. Finite-thickness cohesive elements with physical stiffness properties. 1st International Conference on Mechanics of Composites. New York, NY, United States, June 2014.
- C. Sarrado, F.A. Leone, A. Turon, C.G. Dávila. A numerical study on adhesive thickness effect on bonded joints using a modified finite-thickness cohesive element. 16th European Conference on Composite Materials (ECCM16). Sevilla, Spain, June 2014.
- A. Turon, B.L.V. Bak, C. Sarrado, J. Costa. Delamination under fatigue loads in composite laminates: a review on the computational methods based on the cohesive zone model approach. 5th European Conference on Computational Mechanics (ECCM V). Barcelona, Spain, July 2014.
- C. Sarrado, A. Turon, J. Costa, J. Renart. Caracterización del efecto de los grosores de adherente y adhesivo en la fractura de uniones adhesivas. MATCOMP 2015. Madrid, Spain, July 2015 (*accepted communication*).

- C. Sarrado, A. Turon, J.J.C. Remmers. A coupled plasticity and damage cohesive element for adhesive joints modelling. 9th European Solid Mechanics Conference (ESMC 2015). Madrid, Spain, July 2015 (*accepted communication*).

- C. Sarrado, J.J.C. Remmers, A. Turon. A phantom-node-based cohesive element formulation with coupled plasticity for the simulation of adhesive joints. 20th International Conference on Composite Materials (ICCM20). Copenhagen, Denmark, July 2015 (*accepted communication*).

Dr. Albert Turon Travesa, associate professor at University of Girona, and Dr. Josep Costa Balanzat, full professor at University of Girona,

hereby CERTIFY that

The work entitled *Experimental characterization and numerical simulation of composite adhesive joints using the cohesive zone model approach*, submitted for the degree of Doctor of Philosophy by Carlos Sarrado Molina, has been conducted under their supervision and that it fulfills the requirements to aim for the *International Mention*.

Girona, May 2015.

Albert Turon Travesa
Universitat de Girona, Spain

Josep Costa Balanzat
Universitat de Girona, Spain

List of Figures

List of Tables

Contents

Summary

The number of applications for fiber-reinforced composite materials has experienced a huge rise in the past few decades. Their outstanding stiffness-to-weight and strength-to-weight ratios make them an excellent choice for those applications that pursue the reduction of structural weight as, for instance, applications in aerospace and automotive industries. Particularly, adhesive joints in composite materials contribute to the reduction of structural weight by removing the additional material that mechanically fastened joints would require. Furthermore, adhesively bonded joints are more efficient than mechanically fastened joints in terms of stress redistribution, so by using adhesive joints improved designs can be achieved.

A good understanding of the material behavior is crucial in order to ensure structural integrity, particularly in safety-critical applications. Extensive experimental testing is therefore required to characterize the material, from the coupon level through to the full-scale structure. At the same time, the use of computational tools for the analysis of composite structures plays a key role in the reduction of the developing costs associated to structural design. An important part of the experimental tests can be replaced by computational simulations provided that robust and reliable simulation methods are available.

In view of the previous requirements, the present thesis aims to further the development of robust experimental and numerical methods for the accurate simulation of the fracture process in adhesive joints between composite materials.

In the experimental field, a new method is proposed for the characterization of adhesive joints that widens the range of applicability of the existing methods and lowers the uncertainty of the results. The suitability

of the existing methods for the characterization of adhesive joints is studied and discussed. Using the proposed method along with other methods available in the literature, a complete characterization of an epoxy film adhesive in carbon/epoxy laminates in terms of cohesive laws is presented. The experimental evidence obtained is analyzed so that some guidelines for the simulation of adhesive joints can be given.

With regard to the numerical simulation of adhesive joints, an assessment of some of the readily available cohesive element formulations is undertaken in order to identify their limitations in predicting mixed-mode fracture. Finally, a new cohesive element formulation is proposed for modeling the initial elastic response, softening and failure of finite-thickness adhesives. The new formulation is shown to provide accurate results while ensuring a thermodynamically consistent description of mixed-mode fracture, at the same time allowing physically measured material properties to be employed and not requiring any further adjustment of the properties nor any further model calibration.

Resum

El nombre d'aplicacions dels materials compòsits ha incrementat notablement al llarg de les darreres dècades gràcies a l'excel·lent rigidesa i resistència que ofereixen en relació al seu pes. Les seves propietats mecàniques fan que siguin idonis per a aquelles aplicacions on la reducció del pes estructural juga un paper determinant, com ara en les indústries aeroespacials i de l'automòbil. En particular, les unions adhesives en materials compòsits contribueixen a la reducció del pes estructural ja que permeten l'estalvi del material que requeriria l'ús d'unions mecàniques com ara les unions cargolades o reblonades. A més, l'ús d'unions adhesives és més eficient, ja que origina una redistribució de tensions a la unió que permet l'obtenció de dissenys millorats.

El coneixement detallat del comportament del material esdevé indispensable a l'hora de garantir la integritat estructural, particularment en aquelles aplicacions que comporten un risc per a la seguretat. Aquest fet implica que es requereixi una àmplia caracterització experimental del comportament del material, la qual implica haver de dur a terme un gran nombre d'assajos que van des de petites provetes fins a l'estructura de mida completa. Al mateix temps, l'ús d'eines computacionals per a l'anàlisi de materials compòsits té un paper transcendental en la reducció dels costos de desenvolupament associats a la fase de disseny estructural, ja que una part important dels assajos experimentals es pot substituir per simulacions computacionals sempre que es disposi d'eines de simulació suficientment robustes i fiables.

En vista dels requeriments anteriors, la present tesi té com a objectiu el desenvolupament de mètodes numèrics i experimentals robustos per a la simulació del procés de fractura en unions adhesives de material compòsit.

Pel que fa al camp experimental, en primer lloc es presenta un nou mètode per a la caracterització d'unions adhesives. El mètode proposat amplia el rang d'aplicació dels mètodes existents i en disminueix la incertesa dels resultats. A partir d'aquí, es realitza un estudi crític sobre la idoneïtat dels mètodes de caracterització d'unions adhesives existents, alhora que es presenta la caracterització exhaustiva d'un adhesiu d'epoxy en laminats de carboni/epoxy en termes de la llei cohesiva del material. Les evidències experimentals obtingudes s'analitzen per tal de proporcionar les directrius necessàries per a la simulació d'unions adhesives.

En relació a la part de simulació numèrica, en primer lloc es presenta una avaluació de les formulacions d'elements cohesius existents per tal d'identificar les seves limitacions en la predicció de la fractura interlaminar sota càrregues de mode mixt. Finalment, es presenta la formulació d'un nou element cohesiu per modelar la resposta elàstica, el dany i la fallada d'adhesius de gruix finit. La formulació proposada proporciona resultats precisos alhora que garanteix la descripció termodinàmicament consistent de la fractura en mode mixt. El model plantejat permet l'ús de propietats del material mesurables experimentalment, sense la necessitat de dur a terme cap ajustament o calibratge addicional.

Resumen

El número de aplicaciones de los materiales compuestos se ha visto incrementado a lo largo de las últimas décadas gracias a la excelente rigidez y resistencia que ofrecen en relación a su peso. Sus propiedades mecánicas los hacen idóneos para aquellas aplicaciones en las que la reducción del peso estructural tiene un papel determinante, como por ejemplo en la industria aeroespacial y automovilística. En particular, las uniones adhesivas en materiales compuestos contribuyen a la reducción del peso de la estructura, ya que permiten el ahorro del material que necesitarían las uniones mecánicas como, por ejemplo, las uniones atornilladas o roblonadas. Además, el uso de uniones adhesivas es más eficiente, ya que ocasiona una redistribución de tensiones en la unión que permite la obtención de diseños mejorados.

El conocimiento detallado del comportamiento del material resulta imprescindible para garantizar la integridad estructural, particularmente en las aplicaciones que conllevan un riesgo para la seguridad. Este hecho implica que se requiera una amplia caracterización del comportamiento del material, la cual implica llevar a cabo un gran número de ensayos que van desde pequeñas probetas hasta la estructura de tamaño completo. Al mismo tiempo, el uso de herramientas computacionales para el análisis de materiales compuestos tiene un papel transcendental en la reducción de los costes de desarrollo asociados a la fase de diseño estructural, dado que una parte importante de los ensayos experimentales puede ser remplazada por simulaciones computacionales si se dispone de herramientas de simulación suficientemente robustas y fiables.

A la vista de los requisitos anteriores, la presente tesis tiene como objetivo el desarrollo de métodos numéricos y experimentales robustos para la simulación del proceso de fractura en uniones adhesivas de material com-

puesto.

En lo que a la caracterización experimental se refiere, en primer lugar se presenta un nuevo método para la caracterización de uniones adhesivas. El método propuesto amplia el rango de aplicación de los métodos existentes y reduce la incertidumbre asociada a los resultados. A partir de aquí, se realiza un estudio crítico sobre la idoneidad de los métodos de caracterización de uniones adhesivas existentes, a la vez que se presenta la caracterización exhaustiva de un adhesivo de epoxy en laminados de carbono/epoxy en términos de la ley cohesiva del material. Las evidencias experimentales obtenidas se analizan con el objetivo de proporcionar las directrices necesarias para la simulación de uniones adhesivas.

En cuanto a la parte de simulación numérica, en primer lugar se presenta una evaluación de las formulaciones de elementos cohesivos existentes con el objetivo de identificar sus limitaciones en la predicción de la fractura interlaminar bajo cargas de modo mixto. Finalmente, se presenta la formulación de un nuevo elemento cohesivo para modelizar la respuesta elástica, el daño y el fallo de adhesivos de grosor finito. La formulación propuesta proporciona resultados precisos a la vez que se garantiza la descripción termodinámicamente consistente de la fractura en modo mixto. El modelo planteado permite el uso de propiedades del material medibles experimentalmente, sin necesidad de ajustes o calibraciones adicionales.

Chapter 1

Introduction

1.1 Background

The progressive discovery of the materials available in nature and knowledge on how to use them clearly marked the evolution of ancient humankind and determined the levels of development in ancient cultures. In the last few centuries, and with the birth of material science, humanity has been able not only to learn about the behavior of the materials derived from nature, but also to create new enhanced materials and processes that have allowed us to pass new milestones and revolutionize human society. Nowadays, a vast amount of materials is readily available in developed countries, so material selection is one of the key steps in the product development stages of any modern industry.

Composite materials appeared as a consequence of the efforts made to enhance material properties. These materials are defined as the combination of two or more materials resulting in a material with better properties than its mere individual components. Nowadays, one of the most widely known type of composite material are Fiber Reinforced Polymers (FRP), which this thesis focuses on. The excellent stiffness-to-weight and strength-to-weight ratios of FRP lead to the ability to produce lightweight structures, which is one of the reasons why aerospace industries have led the increase in FRP usage since the FRP industry began to mature during the 1970s. The presence of FRP in aircraft structures has expanded progressively over the past three decades, as illustrated in Figure 1.1, escalating from less than 10% in aircraft structure weight in the 1980s to the approximate 50%

that can be found nowadays in both the Boeing 787 Dreamliner and the Airbus A350XWB structures.

Assembling complex structures necessarily involves joining their components, which in metallic materials can be done by means of several well-established techniques such as welding, riveting, brazing or gluing, among others. However, in the field of composite structures the assembly process is, in most cases, limited to mechanically fastened or adhesively bonded joints [1]. The use of mechanical fasteners in the assembly of composite structures creates areas of high stress concentration that, in conjunction with the low bearing capacity of composite materials, result in structurally inefficient joints. Conversely, adhesive joints are able to redistribute loads so that stress concentrations can be lowered or suppressed. At the same time, the use of adhesive joints results in higher strength-to-weight ratios, better fatigue behavior and the reduction of manufacturing processes thus

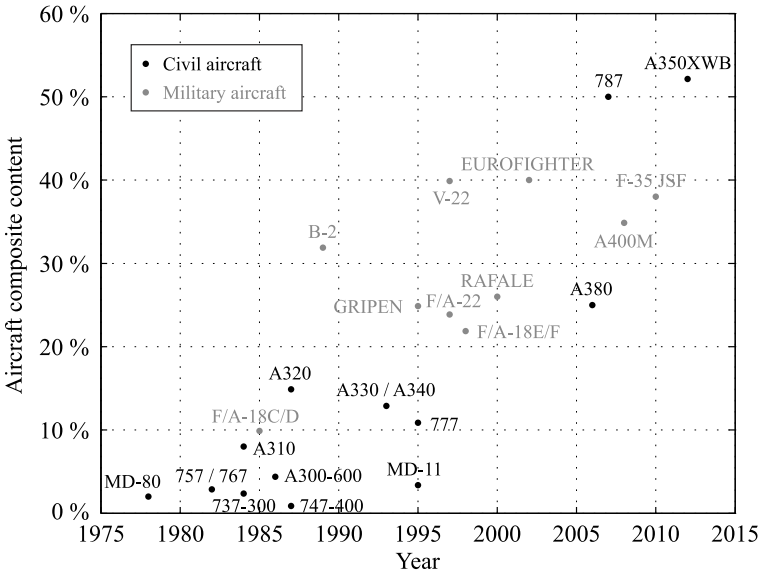

Figure 1.1: Aircraft composite content in percentage of structural weight for some of the most well-known aircraft over the past four decades (*source: Teal Group, Boeing, Airbus, Composite Market Reports*).

contributing to both weight and cost savings [1]. On the other hand, aircraft structures are permanently exposed to damage as a consequence of impacts, lighting strikes, etc. If damage occurs in large structural components, the replacement of the whole component is usually not an option and damage must be repaired in-situ, usually by removing the damaged material and adhesively bonding the repairing material as illustrated in Figure 1.2. Although mechanically fastened joints cannot be fully replaced by adhesive joints as they enable structure disassembly and ease inspection, the presence of adhesively bonded joints in composite structures follows nowadays a growing tendency. However, the reliability of adhesive joints is still limited due to their sensitivity to manufacturing flaws and the difficulties that arise in their inspection, characterization and analysis. Whether adhesive joints are present from the design stage or as a consequence of a repair, their structural integrity must be ensured.

(a) (b) (c)

Figure 1.2: Damage repair in an aircraft structure (*source: The Boeing Co.*).

1.2 Motivation

Despite the growing use of FRP, their application in structural components is still limited by the difficulty in predicting their service life. Extensive experimental testing is required to ensure that load-bearing structures are able to sustain any feasible load combination, particularly in safety-critical applications such as aircraft primary structures. Experimental testing ranges from material characterization tests at a coupon level right through to full-scale tests, which is known as the *Building Block Approach* [2]. A

consequence of this is that the use of FRP load-carrying structures is limited to those industries that can afford such extensive and expensive testing programs. That is also the reason why the aerospace industry, particularly through military aircraft development, was the leader and instigator in the early stages of the rise in FRP usage. However, the use of composite materials has since spread to other industries as the understanding of their behavior improved.

Numerical simulations play a key role in the reduction of the number of mechanical tests required and, consequently, in the reduction of non-recurrent development costs and the expansion of composite materials not only to high-end performance structures, but also to mass production industries. This approach is known as *virtual mechanical testing* and its philosophy is based on replacing actual mechanical tests with numerical simulations, which results in more refined solutions as several designs can be numerically assessed. For numerical models to serve such a purpose, two conditions must be met: the experimental behavior of the material must be known in detail and the numerical models must be robust, reliable and thoroughly validated against the experimental data.

Design in composite materials is usually based on a *damage tolerance* approach, in addition to the conventional strength verification. The heterogeneous nature of composite materials results in inherently flawed materials where either micro or macroscopic cracks are present from the beginning of the service life of a component. Unlike the pure strength approach, the damage tolerance approach allows and accounts for the existence of subcritical cracks and their growth below a critical size between inspection intervals. Therefore, the numerical models used for designing in composite materials must not only be able to assess the strength of the structure, but also to accurately predict crack onset and propagation.

In terms of the analysis of damage processes in adhesive joints, Linear Elastic Fracture Mechanics (LEFM) is the simplest existing approach as it relies on a single parameter - the fracture toughness - to describe the fracture process. Both its simplicity and its good accuracy in the analysis of delamination problems have encouraged the use of LEFM in the analysis of adhesive joints (see e.g. the method described in the ASTM standard for mode I fracture toughness measurement of adhesive joints [3]). However,

small-scale fracture is assumed in LEFM, i.e. the Fracture Process Zone (FPZ) that develops ahead of a crack tip must be small in comparison to the relevant dimensions of the component. Unfortunately, fracture in adhesive joints might involve large-scale fracture because of the large plasticity and damage regions formed near the crack tip and, therefore, their characterization falls outside the scope of LEFM. Alternative experimental data reduction methods for the fracture toughness measurement that do not rely on LEFM are available in the literature. The J-integral approach, first introduced by Rice [4], is defined as a path-independent contour integral that, under certain conditions, equals a non-linear energy release rate. Unlike LEFM, the J-integral is not limited to small-scale fracture processes. Although the J-integral is one of the most widespread methods for the analysis of large-scale fracture in the framework of ductile failure in metals, its application to the analysis of fracture processes in FRP is still limited today.

With regard to the numerical modeling of adhesive joints in a finite element analysis framework, cohesive zone models [5] are an excellent approach. First and independently proposed by Dugdale [6] and Barenblatt [7], cohesive zone models rely on the assumption that all the nonlinear behavior of the material is contained in a thin band ahead of the crack tip. Cohesive zone models are governed by a traction-separation law, which is assumed to be a material property dependent on the loading mode, that describes the softening behavior of the material due to plasticity and damage. Cohesive elements can reproduce in detail the crack growth and the FPZ behavior, so their range of applicability is wider than LEFM-based simulation methods such as the Virtual Crack Closure Technique (VCCT). LEFM-based methods are limited to the simulation of small-scale fracture because they cannot model the FPZ. Unlike cohesive zone models, they cannot capture crack onset as they require an existing crack to compute the fracture energy.

1.3 Objectives

The present thesis aims at developing robust experimental and numerical methods based on the cohesive zone model approach for the accurate sim-

ulation of the fracture process in FRP adhesive joints. To pursue this main goal, the specific objectives of the thesis are, firstly, to provide methods for thoroughly characterizing the experimental fracture behavior of adhesive joints in FRP and, secondly, to develop the computational models required for the accurate simulation of adhesive joints fracture in a finite element analysis framework.

1.4 Thesis structure

In order to achieve the objectives described in Section 1.3, the thesis has been divided into two main research blocks that are reflected in this document as two parts. Part I includes Chapters 2, 3 and 4 and contains the works related to the experimental characterization of adhesively bonded joints, while Part II encompasses Chapters 5 and 6 containing the numerical investigations conducted and the numerical model developed in this thesis for the simulation of adhesive joints in FRP.

With regard to the experimental block of this thesis, in Chapter 2 an experimental data reduction method for the characterization of adhesive joints under mixed-mode loading is presented. Chapter 2 is a reproduction of the manuscript submitted to the journal *Composites Science and Technology* [8].

Chapter 3 contains a study on the validity of LEFM-based experimental data reduction methods for the characterization of adhesive joints. The error committed when using LEFM-based methods is quantified and discussed by comparing the results to those given by the J-integral approach in an experimental test campaign of an FM-300 epoxy film adhesive in carbon/epoxy laminates. This comparison is made for different adhesive and adherend thicknesses under pure modes I and II. The work presented in Chapter 3 is a reproduction of the manuscript submitted to the *International Journal of Solids and Structures* [9].

In Chapter 4 a thorough experimental characterization of an FM-300 epoxy film adhesive in a carbon/epoxy laminate under pure-mode and mixed-mode loading is presented. The bond fracture toughness and its cohesive law are measured for different adherend and adhesive thicknesses. The experimental data reduction method presented in Chapter 2 is used,

along with other J-integral-based methods available in the literature. Chapter 4 is a reproduction of the manuscript submitted to the journal *Composites Science and Technology* [10]. The works presented in Chapters 3 and 4 also resulted in two contributions to conferences: the international conference *Comptest 2015* [11] and the national conference *Matcomp 2015* [12].

With regard to the numerical simulation block of this thesis, Chapter 5 presents an investigation of the effect of the local mixed-mode ratio variation within the FPZ on the numerical simulation results of existing cohesive element formulations. Three different cohesive element formulations are assessed by means of the proposed procedure and their limitations for accurately predicting mixed-mode fracture are investigated. This chapter is a reproduction of the work published in the journal *Composites Part A: Applied Science and Manufacturing* [13]. This work was presented at the international conference *ESMC 2012* [14].

In Chapter 6 a new cohesive element formulation is proposed for modeling the initial elastic response, softening, and failure of finite-thickness adhesives. The new formulation, which has been implemented in the commercial finite element software Abaqus [15], ensures proper dissipation of fracture energy for opening and shear loading modes and mixed-mode loading conditions with any combination of physically measured elastic and fracture material properties. The work presented in Chapter 6 is a reproduction of the manuscript submitted to the journal *Engineering Fracture Mechanics* [16]. This work also resulted in two contributions to the international conferences *MechComp 2014* [17] and *ECCM 2014* [18].

The thesis is concluded in Chapters 7 and 8, where general concluding remarks and recommendations for future research are made.

Part I

Experimental characterization of adhesive joints

Chapter 2

An experimental data reduction method for the Mixed Mode Bending test based on the J-integral approach

Abstract. The Mixed Mode Bending test (MMB) is suitable for measuring the interlaminar fracture toughness of composite materials under mixed-mode loading. Data reduction is usually based on the assumptions of Linear Elastic Fracture Mechanics, which are not fulfilled in configurations involving large scale fracture, such as in adhesive joints. In this work, a J-integral-based method that can be applied in presence of large fracture process zones is presented. The proposed method requires less input information and avoids crack length monitoring during the test, which reduces the uncertainty of the results as compared to traditional methods. The method is shown to accurately compute the fracture toughness in a delamination test campaign and to provide results with lower uncertainty than those of the ASTM standard method.

2.1 Introduction

In the past few decades, laminated Fiber Reinforced Polymers (FRP) have markedly raised their applicability in safety-critical applications, such as aircraft structures, as part of industry efforts to reduce structural weight. For safety reasons, a thorough experimental characterization of the behavior of the different components is required, from a material level right through to a full-scale structure. Given the relatively low interlaminar strength of laminated composite materials, interlaminar fracture is a com-

mon failure mechanism. Therefore, interlaminar fracture toughness is one of the most relevant parameters used in the design and certification of composite structures. Currently, there are well-established standard test procedures for the characterization of fracture toughness for delamination in FRP for pure mode I and mixed-mode loading [3, 19].

The Mixed Mode Bending (MMB) test, first proposed by Reeder and Crews [20–22], is an interlaminar fracture toughness characterization test for unidirectional FRP under mixed-mode loading conditions. The test has been standardized in the ASTM D6671/D6671M-06 [19] and is presently the most widely used test in the characterization of mixed-mode delamination fracture toughness. The MMB specimen, depicted in Figure 2.1, is a rectangular unidirectional composite specimen with a pre-crack of length a_0 on one of its ends, which serves as a delamination initiator. The specimen is fixed to a base and the load is introduced vertically onto the upper lever, which in turn pushes the specimen down at its half span length point and, at the same time, pulls the upper arm of the cracked region up by its end. The mode mixture of the test can be changed by adjusting the lever arm c (Figure 2.1).

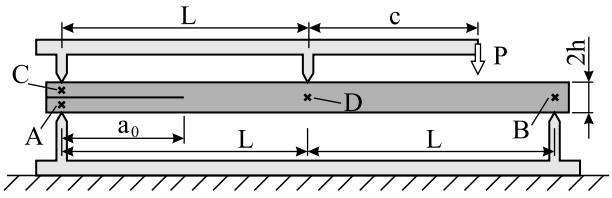

Figure 2.1: MMB specimen.

The data reduction method for the MMB test described in the ASTM standard [19] is based on Linear Elastic Fracture Mechanics (LEFM). The main hypothesis behind LEFM is that the nonlinear deformation at the delamination front or Fracture Process Zone (FPZ) is small in comparison to any of the specimen's dimensions (width, thickness, crack length). This LEFM-based data reduction method has been extensively used in the characterization of delamination in FRP. However, the interlaminar fracture of, for instance, adhesively bonded joints may involve large FPZs. In those cases involving large scale fracture, the use of an LEFM-based data reduc-

tion method for the fracture toughness characterization is fundamentally flawed.

The J-integral approach has been used to characterize fracture processes with large FPZs, especially in the field of metallic materials. The J-integral, first proposed by Rice [4], is a path-independent contour integral that can be interpreted as a nonlinear energy release rate. In the particular case where LEFM applies, the J-integral is equivalent to Griffith's definition of the energy release rate $\mathcal{G}$ [23]. In the specific field of interlaminar fracture of FRP, the J-integral approach has also been used in the characterization of fracture processes involving large FPZs [24–32]. Its application is restricted to elastic materials (either linear or nonlinear) and to plastic materials that are not unloaded (notice that non-unloaded plasticity can be seen as nonlinear elasticity [33]).

Several J-integral closed-form solutions for various interlaminar fracture tests are available in the literature (see the reviews presented in [34–36]). One way to derive these closed-form solutions is to select an integration path and use beam theory assumptions that allow the contour integral to be solved. Following this procedure, J-integral closed-form solutions have been derived for pure-mode I [4, 24, 25], pure-mode II [37–39] or mixed-mode [40–42] tests. Depending on the integration path chosen and the elastic assumptions made, different solutions might be reached (e.g. see solutions in [30] and [31] for the DCB-UBM test). However, depending on the assumptions made, the J-integral solution might require the crack tip position to be known, which is not feasible in the presence of large FPZs. Although an equivalent crack length can be defined in terms of the specimen's compliance, the assumed elastic profile of the specimen might significantly differ from the actual elastic profile at those regions where the contour integral is solved.

On the other hand, simpler closed-form solutions that do not require beam theory assumptions can be derived for some specific tests by properly selecting the integration path. Paris and Paris [43] were the first to propose this kind of solution. They solved the J-integral for the pure-mode I Double Cantilever Beam (DCB) specimen along its external edge and obtained a closed-form solution that relies only on the applied load and the rotation angle at the load introduction point. The lack of beam theory assumptions

makes the method more general and yields a solution that is independent of specific elastic parameters and of the crack length. Crack length independence is indispensable in those situations involving large FPZs, where the crack tip position becomes unidentifiable in practice. It may also be advantageous in those situations where the observation of the specimen's edge becomes cumbersome (e.g. in tests at cryogenic temperatures). Gunderson et al. [44] reported a good agreement between the results of a DCB test obtained with the method proposed by Paris and Paris [43] and those provided by the LEFM-based data reduction method described in the ASTM standard. The method was also extended by Nilsson [45] to account for large displacements. Following a similar procedure, Stigh et al. [46] derived a J-integral closed-form solution for the pure-mode II End Notched Flexure (ENF) test. This solution relies only on the applied force and three rotation angles.

In this work, a similar procedure as in [43] has been used to derive the J-integral closed-form solutions for the MMB test. The resulting equation can be applied in the presence of large FPZs and requires the measurement of the applied load and four rotation angles. In order to test the accuracy of the proposed method, four MMB delamination tests have been conducted for two different mixed-mode ratios. The results from the data reduction method described in the ASTM standard, which has been widely shown to be accurate for delamination specimens, have been used as a reference to validate the proposed method. Accurate results and lower uncertainties have been obtained.

The current paper is structured as follows. Firstly, in section 2.2.1, the J-integral closed-form solution for the MMB test is derived. The requirements of the proposed method are presented and compared to those of the method described in the standard in section 2.2.2. This is followed by a discussion on the range of applicability of the proposed method in section 2.2.3. The test campaign description and the experimental results are presented in sections 2.3 and 2.4, respectively.

2.2 J-integral-based data reduction method of the MMB test

2.2.1 J-integral closed-form solution for the MMB test

The J-integral was first introduced by Rice [4] and can be defined as the decrease of potential energy per increment of cracked surface in a nonlinear elastic material. It is a contour integral defined as

$$J_\Gamma = \int_\Gamma \left(\omega dx_2 - T_k \frac{\partial u_k}{\partial x_1} ds \right) \quad (k = 1, 2) \tag{2.1}$$

where ω is the strain energy density, T_k is the tractions vector perpendicular to the integration path Γ and u_k is the displacements vector.

If computed along a closed contour in an elastic material free of singularities, the J-integral is proved to be path independent and to take the value of zero. For the particular case of the MMB specimen, consider the integration path along its external contour $\Gamma = \sum \Gamma_i$ depicted in Figure 2.2. Given the path independence property of the J-integral , $J_\Gamma = J_{tip}$.

According to Figure 2.2, paths Γ_1, Γ_3 and Γ_6 run through an unloaded

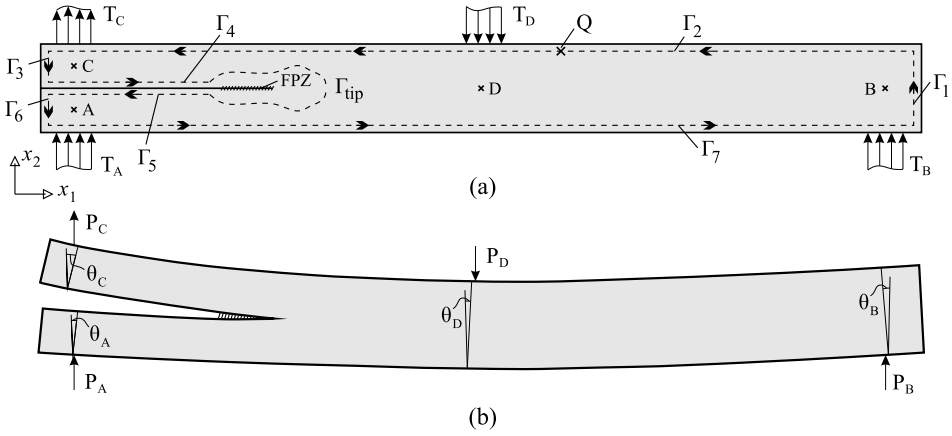

Figure 2.2: (a) Loads and integration path selection in the MMB specimen undeformed configuration. (b) Loads and rotation angles in the MMB specimen deformed configuration.

region of the specimen, whereas paths Γ_4 and Γ_5 run through a free surface parallel to the crack direction ($dx_2 = 0$ and $T_k = 0$). Therefore, $J_{\Gamma_1} = J_{\Gamma_3} = J_{\Gamma_4} = J_{\Gamma_5} = J_{\Gamma_6} = 0$.

Paths Γ_2 and Γ_7 also travel through a free surface parallel to the crack tip. J_{Γ_2} and J_{Γ_7} are zero everywhere except at those points where an external traction is applied, i.e. the load introduction points. The normal vector to paths Γ_2 and Γ_7 are $n = \{0 \quad 1\}$ and $n = \{0 \quad -1\}$, respectively, so the traction vector at any point Q takes the form $T_k = \left\{\sigma_{12}^Q \quad \sigma_{22}^Q\right\}$ if $Q \in \Gamma_2$ and $T_k = -\left\{\sigma_{12}^Q \quad \sigma_{22}^Q\right\}$ if $Q \in \Gamma_7$.

The derivative of the displacements is defined as $\frac{\partial u_k}{\partial x_1} = \left\{\frac{\partial u_1^Q}{\partial x_1} \quad \frac{\partial u_2^Q}{\partial x_1}\right\} = \left\{\epsilon_{11}^Q \quad \tan\theta_Q\right\}$, where θ_Q is the rotation angle at point Q. As a small-displacement formulation is considered, $\tan\theta_Q \approx \theta_Q$.

The first term in Equation (2.1) vanishes for paths Γ_2 and Γ_7 ($dx_2 = 0$). In the case of the traction vector, σ_{12} is zero at any point on the contour of the specimen, whereas σ_{22} is zero at any point on the integration path except at load introduction points, where it takes the value of the externally applied traction. If the tractions in Figure 2.2 are considered as concentrated forces applied in an infinitesimal region dx_1, then $\int \sigma_{22}^Q dx_1 = \frac{P_Q}{b}$, where P_Q is the force applied at point Q and b is the specimen width. Given that the rotation angles are constant at the infinitesimal region where each traction is applied and taking $ds = -dx_1$ for path Γ_2 and $ds = dx_1$ for path Γ_7 (Figure 2.2), the integral in Equation (2.1) can be solved to obtain

$$J = \frac{1}{b}\left(P_A\theta_A + P_B\theta_B + P_C\theta_C - P_D\theta_D\right) \tag{2.2}$$

where P_A, P_B, P_C, P_D and θ_A, θ_B, θ_C, θ_D are the forces and the rotation angles at load introduction points, respectively. These forces can be obtained as a function of the applied force P from the static equilibrium of the MMB setup (Figure 2.1). Replacing their values in Equation (2.2), the J-integral closed-form solution for the MMB specimen is obtained:

$$J = \frac{P}{b}\left[\left(\frac{1}{2} - \frac{c}{2L}\right)\theta_A + \left(\frac{c}{2L} + \frac{1}{2}\right)\theta_B + \frac{c}{L}\theta_C - \left(\frac{c}{L} + 1\right)\theta_D\right] \tag{2.3}$$

where b is the specimen width, L is the specimen half span length and c is the lever arm; as illustrated in Figure 2.1. P is the applied load at the lever arm (in absolute value) and θ is the rotation angle at points A, B, C and D (Figure 2.1). θ is positive in the counterclockwise direction.

The J-integral can be decomposed into loading modes by using the formulation presented by Huber et al. [47] and Rigby and Aliabadi [48]. However, LEFM assumptions are made in the derivations of the mode partitioning in [47, 48] and, therefore, the MMB J-integral mode decomposition presented next is only valid for small FPZs in comparison to the specimen's relevant dimensions. Even though other J-integral mode decompositions exist (see e.g. the work by Bui [49]), to the authors' knowledge all of them rely on LEFM assumptions, which is the framework where mode mixity is actually defined. Operating in a similar fashion as before but using the two-dimensional particularization of the mode-decomposed J-integral formulation (similarly as in a previous work by the authors [13]), the following J-integral closed-form solution for modes I and II is obtained:

$$J_I = \frac{P}{2b}\left(\frac{3c}{L} - \frac{1}{2}\right)(\theta_C - \theta_A) \tag{2.4}$$

$$J_{II} = \frac{P}{b}\left(\frac{c}{L} + \frac{1}{2}\right)\left(\theta_B - 2\theta_D + \frac{1}{2}(\theta_C + \theta_A)\right) \tag{2.5}$$

The mode-decomposed formulation requires the integration path to be symmetric with respect to the crack front. To integrate along the specimen external contour, as in this work, the specimen must be symmetric with respect to the crack plane. This restriction applies only to the J-integral mode decomposition and not to the total J-integral closed-form solution given earlier (Equation (2.3)).

Note that the equations for the DCB and ENF specimens can be seen as a particular solution of Equations (2.3) - (2.5). For the DCB specimen $P_A = -P_C$, $\theta_A = -\theta_C$ and $P_B = P_D = \theta_B = \theta_D = 0$, yielding $J_I = 2\frac{P_C}{b}\theta_C$ and $J_{II} = 0$; which is the same expression originally proposed by Paris and Paris [43]. Similarly, for the ENF specimen $P_C = 0$, $P_A = P_B = \frac{P_D}{2}$ and $\theta_A = \theta_C$, yielding $J_I = 0$ and $J_{II} = \frac{P_D}{2b}(\theta_B - 2\theta_D + \theta_C)$; which is the solution reached by Stigh et al. [46].

2.2.2 Experimental method requirements

The proposed method requires the synchronized monitoring of the applied load and four rotation angles at the load introduction points (see points A, B, C and D in Figure 2.1). These points are far from the crack tip and, therefore, they are located in linear elastic regions where the through-the-thickness rotations are uniform. Consequently, the measurement of the four required angles becomes straightforward in comparison to those J-integral closed-form solutions that require the rotation angle to be measured at the crack tip [41] where strong inelasticities occur. The rotation angles can be measured with different systems, e.g. by using inclinometers, digital image correlation or, as in the current work, by using an image processing algorithm (described in section 2.3).

No other parameters need to be monitored during the test. The elastic properties of the material are not needed either, as no beam theory assumptions are made in deriving the equations. Only the specimen's length and width need to be measured before the test. The compliance calibration of the testing machine required by the standard is not required here as the displacement applied is not involved in the method equations.

It is worth highlighting that, unlike the LEFM-based methods, the crack length needs to be neither monitored nor estimated. Having to monitor the crack length is not desirable in the presence of large FPZs, where the crack tip is not a point, but rather a region and its measurement becomes indeterminate. Besides, as shown in the Appendix, crack length monitoring is a considerable source of uncertainty in the results.

The input parameters required by the method proposed in this work are summarized in Table 2.1 and compared to those of the LEFM-based method described in the ASTM standard [19]. In Table 2.1, E_{11} and E_{22} are the Young's moduli in the longitudinal and transverse directions, respectively, G_{13} is the transverse shear modulus and a is the crack length.

2.2.3 Range of applicability

The proposed data reduction method is suitable for characterizing the interlaminar fracture of MMB specimens regardless of the FPZ size, provided that the FPZ size does not exceed the specimen span length. Unlike LEFM-

	LEFM-based method in ASTM D6671-06 [19]	Proposed method
Geometrical measurements	b, c, L, h	b, c, L
Elastic properties	E_{11}, E_{22}, G_{13}	none
Measurements during test	P, a	P, θ_A, θ_B, θ_C, θ_D

Table 2.1: Inputs required by the standard LEFM-based method and the J-integral method proposed in this work.

based methods, the J-integral method can be used in those materials with large FPZs, such as adhesively bonded joints. The proposed method is expected to yield the same results as LEFM-based methods in those cases involving small FPZs; given that $J = \mathcal{G}$ when LEFM applies [50]. The mode partitioning given by Equations (2.4) and (2.5) is limited to small FPZs, as detailed in section 2.2.1.

The method can be applied to any MMB specimen provided that the two adherends behave elastically and have the same elastic properties. Its applicability is therefore limited to single-material interfaces. As the LEFM-based method described in the ASTM standard is for unidirectional composites, the same limitation applies. The derivation of an LEFM-based data reduction method for bimaterial interfaces is not straightforward either, as the stress singularity becomes oscillating [51, 52].

In addition, if the mode partitioning (Equations (2.4) and (2.5)) is to be obtained, the MMB specimen must be symmetric. This limitation does not apply to the total J-integral (Equation (2.3)).

2.3 Specimens, material and experimental setup

Two AS4/8552 MMB specimens with different thicknesses were used for the test campaign. Each specimen was tested for two mixed-mode ratios: 35% and 70%. The mixed-mode ratios were computed assuming LEFM conditions and following the ASTM standard [19]. The tests were performed in the AMADE research group testing laboratory, which is ISO17025 and NADCAP (non-metallic materials) certified, at the University of Girona.

The specimens were 25 mm wide, 150 mm long and had a 50 mm

precrack. Two different specimen thickness were tested: $2h = 3$ mm ($[0_8/\mathrm{d}/0_8]$) and $2h = 4.5$ mm ($[0_{12}/\mathrm{d}/0_{12}]$), where d denotes the delamination plane. The longitudinal and transverse Young's Moduli were 120.9 GPa and 8.8 GPa, respectively, and the shear modulus was 4.6 GPa. The elastic properties were obtained from [53]. As discussed in the preceding sections, the elastic properties of the specimens are only needed for the ASTM standard data reduction method, and not for the method proposed in this work.

As required by the standard, the specimen was marked on one side to monitor the crack length. The opposite side was marked with four thin red lines at the load introduction points. These marks were used for measuring the rotation angle at these points, as required by the proposed method. Pictures of this side of the specimen were taken during the test (Figure 2.3). These pictures were synchronized with the data acquisition of the applied load and later processed with an in-house Matlab [54] image processing algorithm to obtain the rotation angles. Prior to the tests, the in-house image processing algorithm was validated by comparing its results to the results of a calibrated inclinometer. The maximum deviation of the image processing algorithm was shown to be below ± 0.03 degrees over the whole measurement range. Note that other systems, such as inclinometers, could also be used to measure the four rotation angles.

ASTM standard D6671/D6671M-06 [19] test setup and procedure were used. Two modifications were made in order to have more data available for comparison:

1. In order to have a longer crack propagation, the total length between supports $2L$ was 150 mm, instead of the 100 mm suggested in the standard.

2. The marks made for monitoring crack length along the edge of the specimen were placed every 1 mm, instead of every 1 mm for the first 5 mm and every 5 mm thereafter as suggested in the standard.

2.4 Tests results

The fracture toughness results were obtained using the two different data reduction methods compared in this work: the proposed J-integral-based method (Equations (2.3)-(2.5)) and the LEFM-based method described in the ASTM standard D6671/D6671M-06 [19]. The fracture toughness results of the 3 mm-thick specimen test with an LEFM mode mixture of 70% are shown in Figure 2.4. Their uncertainty, calculated according to the procedure of the Appendix, is shown in Figure 2.5. The fracture toughness and the uncertainty are plotted against the lever displacement, which here can be understood as a testing time, as displacement is applied at a constant rate. In fact, the results do not depend on the lever displacement, but rather on the crack length. However, plotting results against crack length is not convenient in presence of large-scale fracture processes, as crack length becomes indeterminate, and crack length measurement is not required for the J-integral method proposed in this work.

As stated above, the tested specimens fall within the scope of the standard, so the results obtained from the standard data reduction method have

Figure 2.3: Picture taken during the test used for the angle measurement.

been taken as a reference to assess the accuracy of the proposed method. The results provided by the J-integral method are in very good agreement with those provided by the LEFM-based method. The largest difference observed between the results of the two methods is below 7% for both the fracture toughness and its mode decomposition.

The uncertainty associated to the fracture toughness measurement provided by the proposed method is shown to be lower than that of the standard (Figure 2.5). As detailed in the Appendix, most of the uncertainty associated to the standard method comes from the crack length measurement; which is avoided using the method proposed in the current work. In the proposed method, most of the uncertainty stems from the angle measurement system used, so it could be further reduced by using more accurate angle measurement systems. The proposed method allows real time monitoring of J, whereas the LEFM-based method yields a discrete measurement of $\mathcal{G}$ that depends on the number of marks on the specimen.

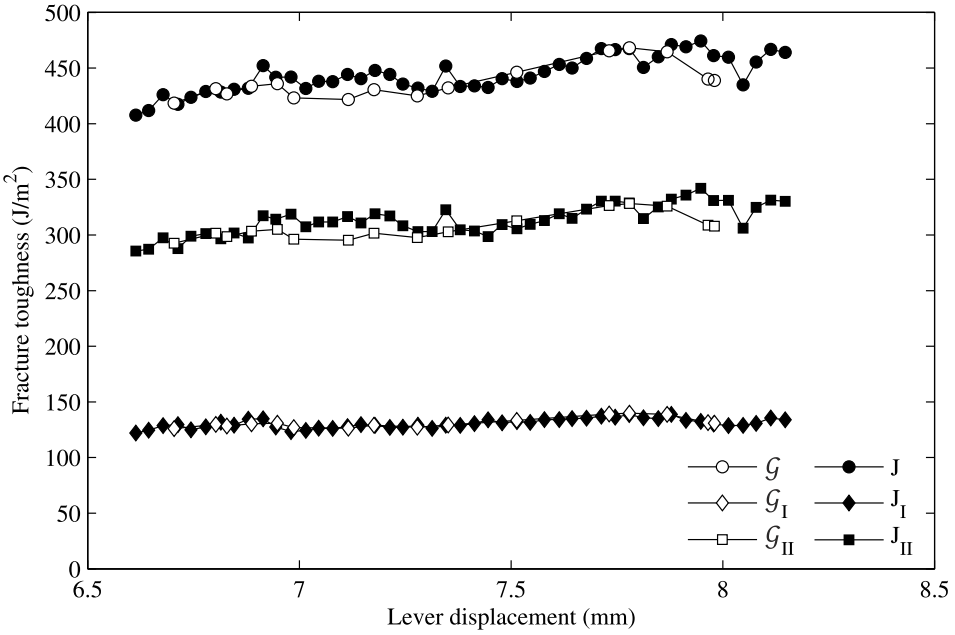

Figure 2.4: Fracture toughness results of the 3 mm-thick specimen MMB 70% test.

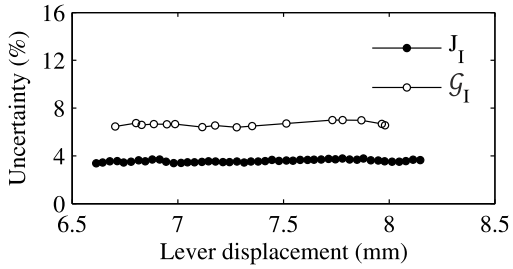

(a) Mode I

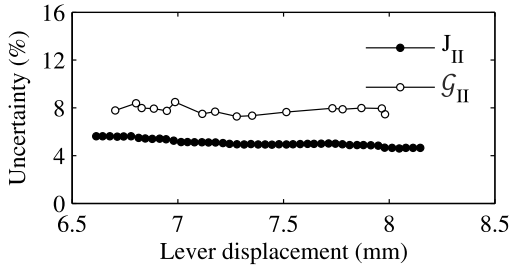

(b) Mode II

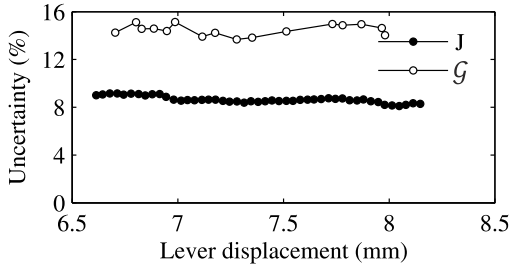

(c) Total

Figure 2.5: Comparison of the uncertainty associated to the measurement of the fracture toughness using the data reduction method proposed in the ASTM Standard [19] and the method proposed in the present work, for the 3 mm-thick specimen MMB 70% test.

In Figure 2.6 a summary of the fracture toughness results for the four MMB tests are presented. The results obtained using the two data reduction methods compared in this work are shown to be similar for all the tests performed, which matches the expectations as LEFM is applicable in this

particular case. The fracture toughness measured for the thicker specimen ($2h = 4.5$ mm) is observed to be higher for the two mode mixtures tested. However, although the two tested specimens were made of the same material, they were not manufactured at the same time. It is not possible to discern whether the difference in the measured fracture toughness is due to the adherend thickness or to the different aging processes the two specimens may have undergone. These considerations are outside the scope of this work.

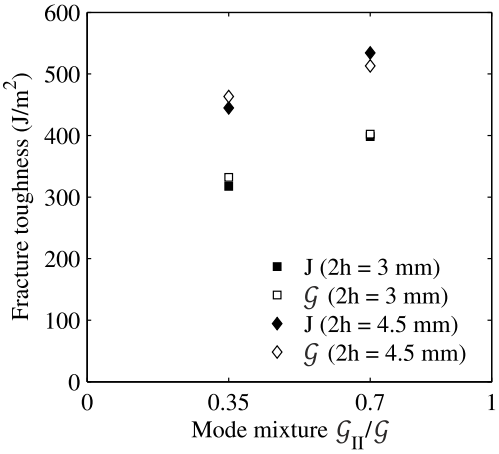

Figure 2.6: Summary of the fracture toughness results of all the MMB tests conducted.

2.5 Concluding remarks

An experimental data reduction method based on the J-integral approach for the Mixed Mode Bending test has been presented. The proposed method has been compared to the LEFM-based method described in the ASTM standard D6671/D6671M-06 in terms of range of applicability, input information required and the accuracy and uncertainty of the results.

The method proposed in this work intrinsically has a wider application range than that of LEFM-based methods, as it can be used to measure

the total fracture toughness in MMB tests involving large fracture process zones. However, the mode decomposition proposed in this work is limited to those cases involving small fracture process zones, where the mode mixity is actually unequivocally defined, and to symmetric specimens with respect to the interface plane.

Unlike LEFM-based methods, the proposed method does not require the characterization of the elastic properties of the material or the testing machine compliance calibration. Furthermore, crack length monitoring or estimation are also avoided. Instead, four rotation angles at load introduction points need to be measured, which can be done in real time. The angle measurement points are located in linear elastic regions far from the crack tip, where rotations are uniform and thus the angle measurement becomes straightforward. The measurement of the rotation angles is more suitable than crack length monitoring in those situations involving large fracture process zones, such as the characterization of adhesively bonded joints, where the position of the crack tip becomes indeterminate.

The results provided by the proposed J-integral method were compared to those produced by the LEFM-based method described in the ASTM standard, which has been thoroughly validated for delamination problems in FRP. Very good agreement between the results of the two methods was observed. The proposed method was also shown to have a significantly lower associated uncertainty than the method described in the standard, as a consequence of the reduction in the input information required and the lack of crack length monitoring during the test.

Appendix. Estimation of the uncertainty of the fracture toughness measurement

The uncertainty associated to the fracture toughness is estimated within a 95% confidence level according to the procedure described in ISO 5725 [55] and in the GUM uncertainty measurement guides [56, 57]. Both documents are in accordance with the requirements of ISO 17025 [58].

The parameters involved in the uncertainty calculation are divided into measurands and measurements. The results of fracture toughness, whose values depend on many parameters and cannot be estimated directly but

through an equation, are called measurands.

The measurements are the parameters that belong to an equation to determine the measurand and whose uncertainty can be estimated directly. The reader is referred to the ASTM D6671/D6671M-06 standard [19] for the equations of the LEFM-based data reduction method and to Equations (2.3) - (2.5) for the method proposed in this work. The uncertainty of the measurements is estimated either from the error of the device that takes the measurement of the parameter or from the standard deviation of an experimental test campaign.

The uncertainties of all the measurements are combined to obtain the overall uncertainty associated to a measurand by taking the square root of the sum of the squares of the measurements uncertainties, i.e. $u_{\mathrm{m}} = \sqrt{\sum_j \left(c_{\mathrm{m,i}} \cdot u_i\right)^2}$. u_{m} is the uncertainty of the measurand m, u_i the uncertainty of the measurement i and $c_{\mathrm{m,i}}$ the sensitivity coefficient, which is obtained from the partial derivatives of the equation defining the measurand with respect to the measurement i as $c_{\mathrm{m,i}} = \frac{\partial m}{\partial i}$. This approach is applicable only for independent measurements. The uncertainty of the total fracture toughness, $u_{\mathcal{G}}$ and u_{J}, is obtained as the sum of the uncertainties of modes I and II.

The uncertainties associated to each measurement for the particular case studied are presented in Table 2.2 and expressed within a 95% confidence interval and described next. For more details on the premises for the estimation of each measurement uncertainty, the reader is referred to [55–57].

The load uncertainty is obtained as $u_{\mathrm{P}} = u_{\mathrm{Pcal}} + u_{\mathrm{Pvis}}$, where u_{Pcal} is the uncertainty of the load cell, obtained from the calibration certificate, and u_{Pvis} is the visual uncertainty of the technician when measuring the crack length. u_{Pvis} is only taken into account in the LEFM-based data reduction method when measuring the visual crack initiation and propagation points. For the J-integral-based method $u_{\mathrm{Pvis}} = 0$, as no crack length measurement is required. u_{Pvis} is determined by the reaction time of the technician in recording the value, which has been estimated in 0.5 seconds. The uncertainty for the estimated human error (95% confidence) is $u_{\mathrm{Pvis}} = \left|P_{\max} - P_{\min}\right| / 2 \cdot (2/3)$, $P_{\max}$ and $P_{\min}$ being the maximum and minimum forces measured at the boundaries of the reaction time inter-

val. u_{Pvis} varies for each propagation point acquired. The maximum value attained during the test is presented in Table 2.2. u_{L} and u_{c} are the uncertainties of the measurement of the half span length and lever length, respectively, of the MMB apparatus, u_{b} and u_{h} are the uncertainties of the specimen width and thickness measurements, respectively, u_{a_0} is the uncertainty associated to the experimental estimation of the visual measurement of the initial crack length, while u_a is measured at each propagation point. $u_{\mathrm{E}_{11}}$, $u_{\mathrm{E}_{22}}$ and $u_{\mathrm{G}_{13}}$ are the uncertainties related to the elastic properties of the adherends: longitudinal and transverse elastic moduli and out-of-plane shear modulus, respectively. They are estimated from the standard deviation of the results of the testing campaign.

u_{s} is the uncertainty associated to the determination of the slope of the load displacement curve. It is calculated from the linear regression of the initial part of the load displacement curve as $u_{\mathrm{s}} = 2 \cdot \sqrt{\frac{(1-r^2)S_\delta^2}{(n-2)S_P^2}}$, where r is the correlation coefficient, n the number of data points and S_δ^2 and S_P^2 are the standard deviations of the displacement and the load, respectively. u_{Csys} is the uncertainty associated to the measurement of the system compliance C_{sys}. Its value is taken from the test campaign that the

Uncertainty	Units	Range (95% of confidence)	$\mathcal{G}$	J
u_{Pcal}	N	$\pm 0.003 \cdot P$	✓	✓
u_{Pvis}	N	$< 0.472^{\dagger}$	✓	-
u_{L}, u_{c}	mm	± 0.5	✓	✓
u_{b}	mm	± 0.03	✓	✓
u_{h}	mm	± 0.002	✓	-
u_{a_0}, u_a	mm	± 0.5	✓	-
$u_{\mathrm{E}_{11}}$, $u_{\mathrm{E}_{22}}$ and $u_{\mathrm{G}_{13}}$	MPa	$\pm 0.1E_{11}, \pm 0.1E_{22}$ and $\pm 0.1G_{13}$	✓	-
u_{s}	N/mm	± 0.0312	✓	-
u_{Csys}	mm/N	$\pm 0.01 \cdot C_{\mathrm{sys}}$	✓	-
u_θ	deg	± 0.03	-	✓

Table 2.2: Uncertainties of the measurements. $\mathcal{G}$ and J denote whether each particular uncertainty affects the LEFM-based or the J-integral-based method, respectively

system compliance is calculated from. It is estimated to be a percentage of the system compliance.

u_θ is the uncertainty associated to the measurement of the rotation angles at points A, B, C and D. Its value has been estimated in ± 0.03 degrees (95% confidence) by comparing the angle measurement image processing algorithm used in this work with the results of a calibrated inclinometer. The maximum deviation between the measurements of the two systems was taken as the uncertainty of the angle measurement.

Chapter 3

On the validity of linear elastic fracture mechanics methods to measure the fracture toughness of adhesive joints

Abstract. The analysis of large-scale fracture processes, such as those involved in the fracture of adhesive joints, falls outside the scope of Linear Elastic Fracture Mechanics (LEFM). However, experimental data produced in testing adhesive joints are usually reduced with LEFM methods. The consequent error has not yet been evaluated. In this work, an experimental characterization under pure-mode loading of an FM-300 epoxy film adhesive is presented for different adhesive and adherend thicknesses. The experimental data is analyzed using both LEFM-based and J-integral-based data reduction methods in order to study their suitability to analyze adhesive joints. LEFM-based data reduction methods are shown to entail a severe fracture toughness overestimation that heavily depends on the size of the fracture process zone. It is concluded that J-integral based methods should be used to characterize adhesive joints and that the use of LEFM is restricted, at best, to the measurement of initiation values. The effect that the adhesive and the adherend thicknesses have on the fracture toughness and the R-curve of the material is studied. Adhesive and adherend thicknesses are shown to have a significant influence on the bond fracture toughness and the source of such influence is discussed.

3.1 Introduction

The use of mechanical fasteners in the assembly of composite structures creates areas of high stress concentration that, in conjunction with the low bearing capacity of composite materials, result in structurally inefficient joints. Conversely, adhesive joints are able to redistribute the loads so that stress concentrations can be lowered or suppressed. At the same time,

the use of adhesive joints results in higher strength-to-weight ratios, better fatigue behavior and a reduction in the manufacturing processes that contributes to both weight and cost savings [1]. Despite their advantages over mechanical fasteners, the reliability of adhesive joints is still limited due to their sensitivity to manufacturing flaws and the difficulties that arise in their inspection, characterization and analysis.

The mechanical properties of a bulk adhesive have been proven hard to correlate with the behavior of a thin adhesive layer because of its confinement between two adherends [59]. The plasticity of the adhesive layer is constrained as is its stress field, which has a direct impact on bond toughness [34, 60, 61]. Pardoen et al. [62] classified the constraint effects of the adhesive layer in internal and external effects. Internal effects refer to the adhesive layer itself, whose thickness variation can cause the transition from small-scale fracture - and therefore a brittle behavior - to a fully developed plastic region. On the other hand, external effects comprise all the elements surrounding the adhesive layer, such as the adherend thickness or its layup, that can affect the size of the plastic zone or the amount of plastic deformation. The research devoted to the characterization of internal effects is extensive [60–64] and shows the significant influence adhesive thickness has on the joint toughness. Fewer works are available in the literature regarding the characterization of the external effects on adhesive joints, but despite this the fracture toughness has also been shown to be influenced by the adherends stiffness [62, 65]. The effect of the adherend thickness has also been reported for specimens with fiber bridging [25, 34] that, despite being different in nature from adhesive joints, can be analyzed in a similar way to adhesive joints as both rely on the analysis of a Fracture Process Zone (FPZ) of relevant dimensions.

Linear Elastic Fracture Mechanics (LEFM) is the simplest existing approach for the analysis of crack growth in adhesive joints, as it relies on a single parameter - the fracture toughness - to describe the fracture process. Both its simplicity and its high accuracy in the analysis of delamination problems have motivated the use of LEFM in the analysis of adhesive joints (see e.g. the methods described in the ASTM D5528-13 and ISO 25217 standards for the mode I fracture toughness measurement of adhesive joints). However, small-scale fracture is assumed in LEFM, i.e. the FPZ that devel-

ops ahead of a crack tip must be small in comparison to any other relevant dimension of the component. Unfortunately, fracture in adhesive joints might involve large-scale fracture because of the large plasticity and damage regions formed near the crack tip and, therefore, their characterization falls outside the scope of LEFM. However, most of the works mentioned above rely on LEFM: they are based either on the stress intensity factor or on estimations of the crack length that require LEFM assumptions.

Alternative methods for the fracture toughness measurement that do not rely on LEFM are available in the literature. The J-integral approach, first introduced by Rice [4], is one of the most widespread methods for the analysis of large-scale fracture. The J-integral is defined as a path-independent contour integral that, for cracks surrounded by large plastic zones, is equal to the energy release rate. Unlike LEFM, the J-integral is not limited to small-scale fracture processes and therefore can be seen as a non-linear energy release rate. In the recent few years, J-integral closed-form solutions independent of LEFM assumptions have been derived for different interlaminar fracture tests [8, 36, 40, 43, 44, 46]. While LEFM-based and J-integral-based experimental data reduction methods are expected to provide the same results in cases of small-scale fracture processes, their results are expected to differ for larger FPZs [34]. However, a comparative study that evidences and quantifies such differences is still missing.

In the current work, an experimental characterization of the FM-300 epoxy film adhesive under pure modes I and II is presented. The effect of the adhesive and the adherend thicknesses on the bond fracture toughness and the R-curve is studied. Test data is reduced by means of both LEFM-based and J-integral-based data reduction methods. The discrepancies between both methods are analyzed and their suitability for the characterization of adhesive joints is discussed.

The experimental tests performed and the data reduction methods applied in this work are described in Section 3.2. The experimental results are presented in Section 3.3 and, in Section 3.4, they are discussed and compared to the observations in the literature.

3.2 Methodology

3.2.1 Material and specimen configuration

The specimens were manufactured using a unidirectional T800S/M21 carbon/epoxy prepreg. Two panels for each batch of specimens were cured and then secondary bonded using FM-300 epoxy film adhesive impregnated in a carrier. A Teflon film was used to form the 60-mm-long insert that triggers the interface debonding. The specimens were 25 mm wide and 250 mm long. Three different adherend thicknesses and two adhesive thicknesses were tested, as outlined in Table 3.1. The two adhesive thicknesses were achieved by using one or two layers of adhesive. The in-plane elastic properties of the adherends are $E_{11} = 134.7$ GPa, $E_{22} = 7.7$ GPa and $G_{12} = 4.2$ GPa [66].

Specimen codes	Specimen total thicknesses (mm)	Layup	Adhesive thickness (mm)
A1T1	3.12 ± 0.06	$[0]_8/d/[0]_8$	0.21 ± 0.02
A2T1	4.60 ± 0.08	$[0]_{12}/d/[0]_{12}$	0.21 ± 0.02
A2T2	4.80 ± 0.10	$[0]_{12}/d/[0]_{12}$	0.37 ± 0.01
A3T1	6.05 ± 0.23	$[0]_{16}/d/[0]_{16}$	0.21 ± 0.02

Table 3.1: Specimen configurations tested. In the layup definition, d denotes the insert location.

3.2.2 Tests and data reduction methods

Double Cantilever Beam (DCB) [67] and End Notched Flexure (ENF) [68] tests were performed to characterize the adhesive joint under pure modes I and II, respectively. The load configuration of each test is depicted in Figure 3.1. A total of 16 tests were carried out. Two DCB and ENF specimens of each material configuration in Table 3.1 were tested.

The DCB tests were performed according to the procedure described in the ISO 25217 test standard. The initial crack length was set to 35 mm for all tests by bonding the load introduction blocks at the corresponding distance. The LEFM-based method described in the ISO 25217 standard

was used. The J-integral method was based on the closed-form solution for the DCB test proposed by Paris and Paris [43]

$$J = 2\frac{P}{b}\theta \tag{3.1}$$

where b is the specimen width, P is the applied load and θ is the rotation angle at the load introduction point. For the tests presented in this work, the angles at both the upper and lower load introduction points of the DCB specimen were monitored in order to remove the initial rigid body rotations from the results (points A and C in the DCB specimen of Figure 3.1).

ENF tests were done based on the procedure described in the test method AITM 1.0006. The distance between supports was set to 120 mm for all the tests performed in order to achieve a longer crack propagation than that of the standard, whereas the initial crack length was set to 35 mm. On one hand, the LEFM-based method described in the AITM 1.0006 test method was used to obtain $\mathcal{G}_{IIc}$. Although the AITM test method covers only initiation values of the mode II fracture toughness, the same equations were used for the propagation values given in this work. On the other hand, the J-integral closed-form solution for the ENF test proposed by Stigh et al. [46] was used for computing J_c as

$$J = \frac{P}{2b}(\theta_A - 2\theta_D + \theta_B) \tag{3.2}$$

where b is the specimen width, P is the applied load and θ_A, θ_B and θ_D are the rotation angles at the load introduction points, as depicted in Figure 3.1. θ_A refers to the arm on the cracked end of the specimen, θ_B refers to the specimen's uncracked end and θ_D refers to its mid-span length point, where the load is applied.

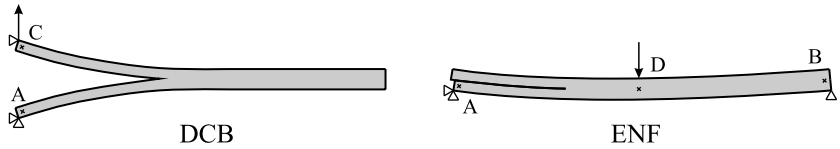

Figure 3.1: Representation of the load introduction in the two test types performed in this work.

3.2.3 Instrumentation

Specimens were marked along one edge with vertical lines every 1 mm to visually monitor the crack length by means of a Canon 550D camera with a macro lens mounted on a traveling fixture.

Two inclinometers were installed at load introduction points for the DCB tests (points A and C in Figure 3.1) and three for the ENF tests (points A, B and D in Figure 3.1). The NA3-30 capacitive dielectric liquid-based inclinometers from SEIKA Mikrosystemtechnik GmbH were used. According to the manufacturer's specifications, the NA3-30 inclinometer has a resolution below 0.005 degrees and a maximum linearity deviation over the whole measurement range (±30 degrees) of 0.06 degrees.

The crack length, the force and displacement from the testing machine and the rotation angles were acquired in real time and synchronized by means of a common displacement channel. The load, displacement and inclinometer rotations were acquired at 20 Hz, while 3 pictures/second were taken with the crack length monitoring camera.

All tests were performed under displacement control at a constant displacement rate in a servohydraulic MTS 858 testing machine using a 5 kN load cell. Given the different compliance of each specimen thickness, the displacement rate applied ranged from 0.5 mm/min to 2.0 mm/min, depending on the specimen type. The displacement rates applied are low enough as to ensure quasi-static crack growth according to test standards [67, 68].

3.3 Results

The results of the 16 test performed - 2 specimens for each DCB and ENF of each specimen type in Table 3.1 - are presented in this section. The results obtained by LEFM-based and J-integral-based data reduction methods, which are denoted by $\mathcal{G}_c$ and J_c, respectively, are compared for the different adhesive and adherend thicknesses tested. An in-depth analysis and a discussion of the results reported in this section are provided in Section 3.4, where the findings of the current work are also compared to the observations available in the literature.

The load-displacement curves of the tests performed are presented in

Figure 3.2. Unstable crack propagation resulted in jumps in the load-displacement curve, which have been removed from the graphs for the sake of clarity. A certain amount of stable crack propagation was obtained in all the tests. Data from only one A3T1 specimen are available for the ENF test (Figure 3.2(b)) as a consequence of a failure in the acquisition of the load channel.

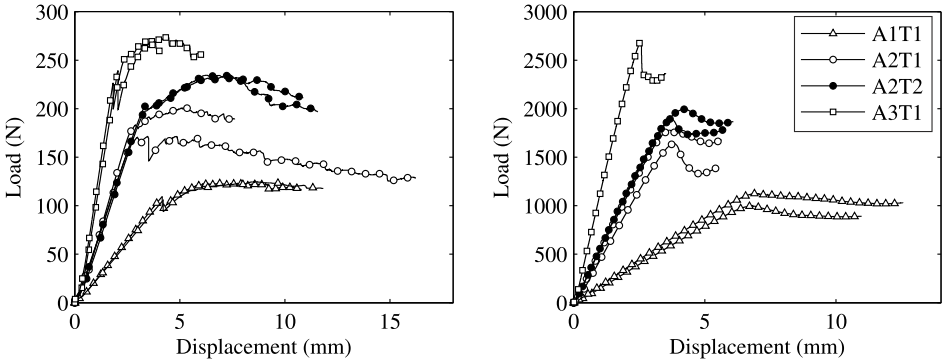

(a) DCB (b) ENF

Figure 3.2: Load-displacement curves (only 1 out of every 1000 points is depicted for clarity).

The results of the ENF tests are presented in Figures 3.3-3.5. The R-curve results of the two adhesive thicknesses tested are compared in Figures 3.3 (a) and (b) using LEFM-based and J-integral-based data reduction methods, respectively. Similarly, the R-curve results of the three adherend thickness tested are shown in Figures 3.3 (c) and (d), also using LEFM and J-integral data reduction methods, respectively. LEFM-based and J-integral-based results are compared in Figures 3.4 and 3.5.

The results of the DCB tests are presented in Figures 3.6-3.8. The R-curve results of the two adhesive thicknesses tested are compared in Figures 3.6 (a) and (b) using LEFM-based and J-integral-based data reduction methods, respectively. Similarly, the R-curve results of the three adherend thickness tested are shown in Figures 3.6 (c) and (d), also using LEFM and the J-integral , respectively, to reduce the experimental data. LEFM-based and J-integral-based results are compared in Figures 3.7 and 3.8.

The fracture toughness results given in this section are plotted against crack extension. However, it should be noted that in presence of large FPZ the crack tip is vaguely defined, so the representation of the x-coordinate might be inaccurate. Nevertheless, the crack length is not used in the computation of J_c and only has an influence on the graphical representation.

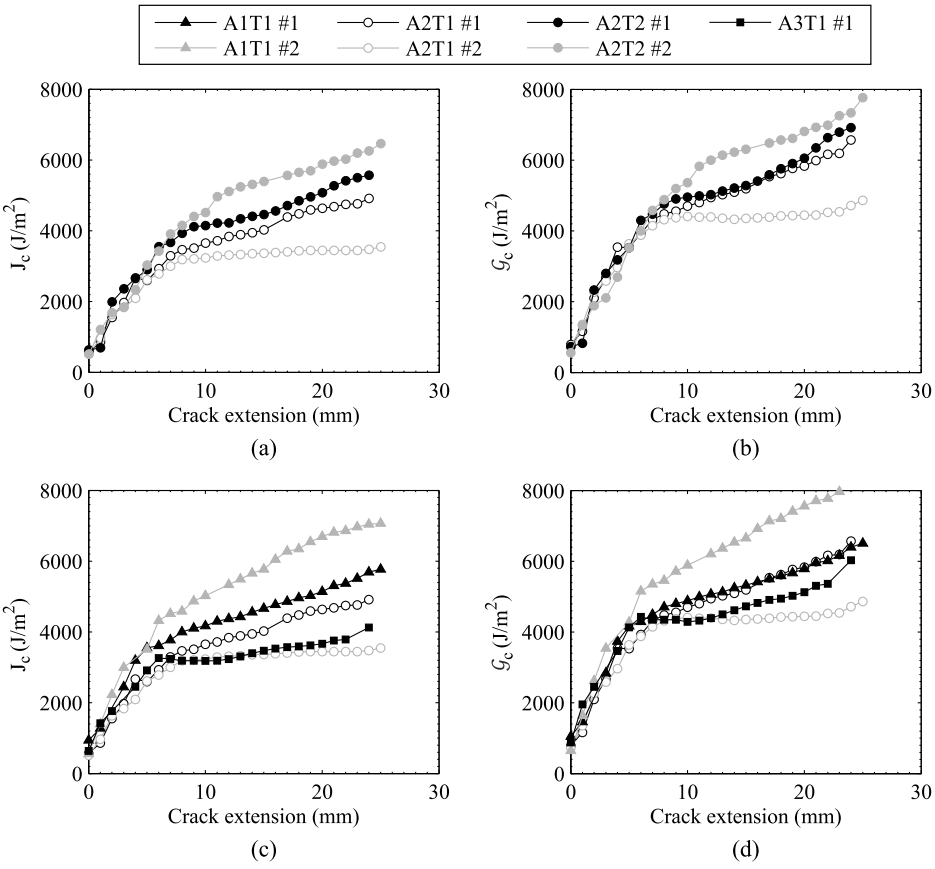

Figure 3.3: Fracture toughness results for ENF tests. Effect of the adhesive (a,b) and adherend (c,d) thicknesses using the J-integral (a,c) and LEFM (b,d) methods.

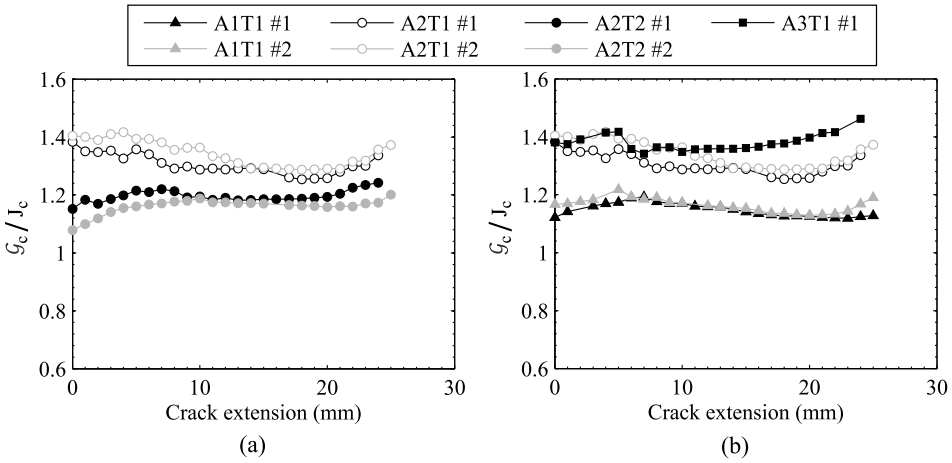

Figure 3.4: Effect of the adhesive (a) and adherend (b) thicknesses on the relative difference between $\mathcal{G}_c$ and J_c for ENF tests.

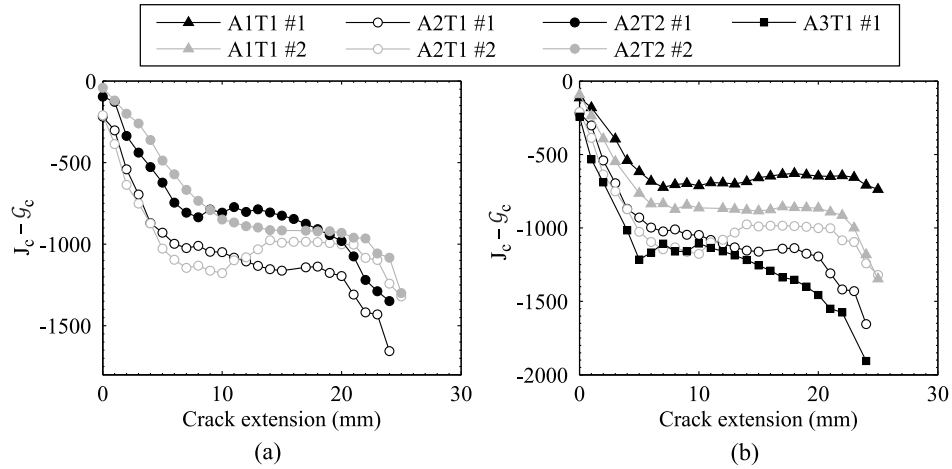

Figure 3.5: Effect of the adhesive (a) and adherend (b) thicknesses on the absolute difference between $\mathcal{G}_c$ and J_c for ENF tests.

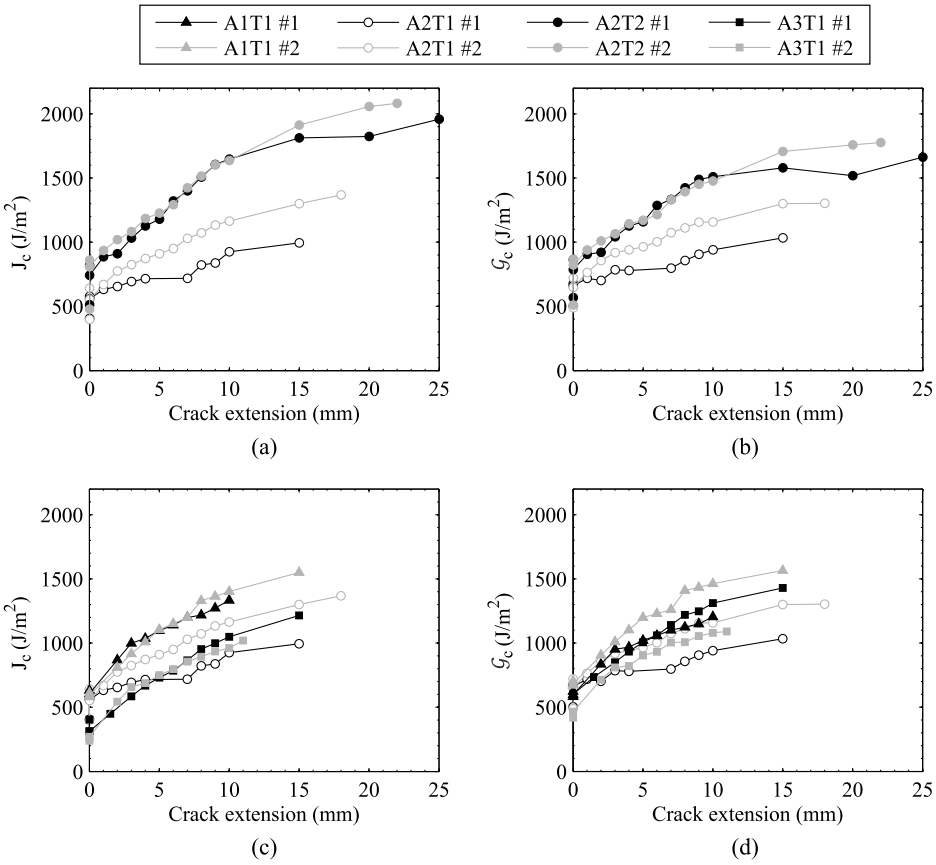

Figure 3.6: Fracture toughness results for DCB tests. Effect of the adhesive (a,b) and adherend (c,d) thicknesses using the J-integral (a,c) and LEFM (b,d) methods.

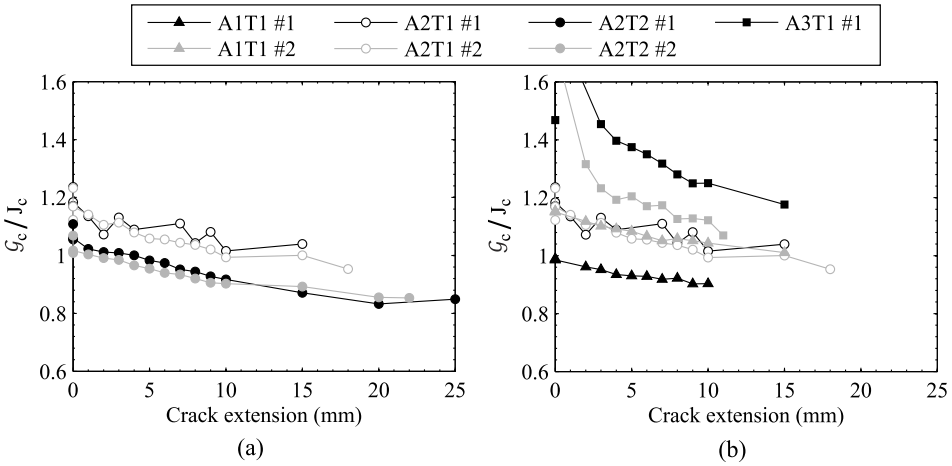

Figure 3.7: Effect of the adhesive (a) and adherend (b) thicknesses on the relative difference between $\mathcal{G}_c$ and J_c for DCB tests.

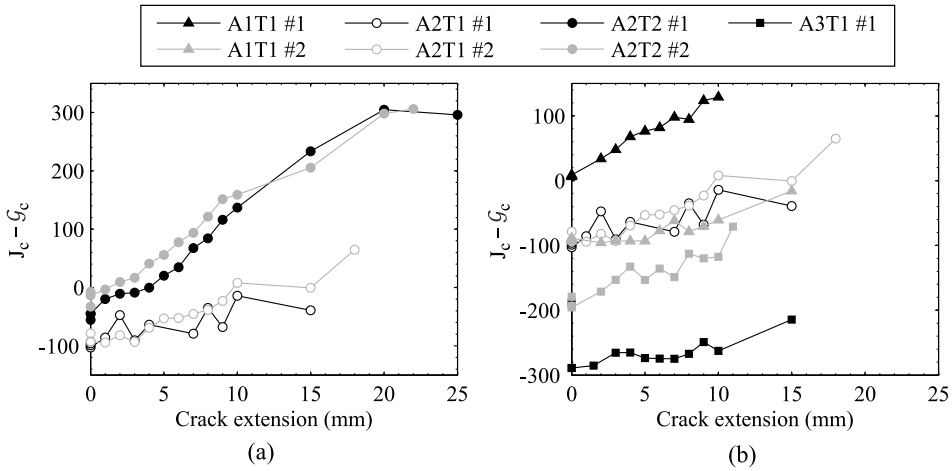

Figure 3.8: Effect of the adhesive (a) and adherend (b) thicknesses on the absolute difference between $\mathcal{G}_c$ and J_c for DCB tests.

3.4 Discussion

The discussion of the results is divided into two areas. Firstly, a discussion on the suitability of LEFM and the J-integral for the analysis of adhesive joints is presented. Secondly, the effect of both the adhesive and adherend thicknesses on the bond fracture toughness is discussed.

3.4.1 Fracture toughness results: $\mathcal{G}_c$ vs J_c

Although in Figures 3.3 and 3.6 similar trends are observed for $\mathcal{G}_c$ and J_c results, substantial discrepancies are obtained from the detailed analysis of the results. As discussed next, the differences between $\mathcal{G}_c$ and J_c heavily depend on and can be fully explained by the length of the FPZ.

LEFM falls into a systematic overestimation of the fracture toughness for pure mode II fracture, as shown in Figure 3.4, that ranges from approximately 15% to 40%. The severity of such overestimation is clearly shown to be dependent on the specimen type or, likewise, on the adherend and adhesive thicknesses. This discrepancy between LEFM and the J-integral results can be explained in terms of the FPZ length: the difference between $\mathcal{G}_c$ and J_c increases as the FPZ length grows. Stiffer adherends are known to entail larger FPZs [34], which in turn results in a higher overestimation of the fracture toughness computed by LEFM, as can be seen in Figure 3.4 (b). LEFM results exhibit an overestimation of approximately 35% for A3T1 specimens, which is reduced to approximately 30% and 15% for A2T1 and A1T1 specimens, respectively. Following the inverse reasoning, the results in Figure 3.4 (a) indicate that thick adhesive layers involve shorter FPZs than thin adhesive layers, as LEFM overestimation of the fracture toughness is less severe. The same discussion applies to mode I fracture, as shown in Figure 3.7. However, the discrepancy between mode I $\mathcal{G}_c$ and J_c results ranges from approximately 10% to 30%, which is less severe than in mode II. This fact can be also explained by the length of the FPZ, which is reported to be smaller under mode I than under mode II [69, 70].

The hypothesis of the increasing deviation of LEFM results as the FPZ grows is also corroborated by the results in Figures 3.5 and 3.8. It can be clearly seen from Figure 3.5 that, for ENF tests, the absolute difference between the LEFM and the J-integral results progressively increases up to a

plateau value. The initial rise corresponds to the FPZ formation, whereas the plateau indicates that the FPZ is fully developed and its length is kept approximately constant thereafter. For large crack extensions, the difference between $\mathcal{G}_c$ and J_c in Figure 3.5 increases further. However, this increase in the difference between $\mathcal{G}_c$ and J_c is due to the FPZ reaching the region near the mid-span length of the specimen, where the external load is applied, and the results are no longer valid. In Figure 3.8, a similar effect of the adhesive and adherend thicknesses to that described for the ENF tests is observed for the DCB tests, albeit with two main differences: the plateau is not obvious as a smaller amount of crack propagation was obtained and the overestimation of the LEFM fracture toughness progressively turns into an underestimation for some of the specimens tested.

In view of the analysis of the results presented in this section, LEFM-based experimental data reduction methods are not suitable for the characterization of fracture toughness in adhesive joints. Rather, J-integral-based methods should be used. However, it can be argued that LEFM-based methods are still valid for the characterization of the initiation values of the fracture toughness. During the early stages of crack growth, the FPZ is still small and the difference in the results given by LEFM and the J-integral might be small enough to fall within the experimental test campaign scatter (see Figure 3.5). However, it must be taken into account that when the crack is observed to grow, a certain amount of FPZ has been already developed, which also leads to a deviation in LEFM results that should be quantified for each particular test. On the other hand, limiting the analysis of adhesive joints to the measurement of the initiation fracture toughness implies a severe underestimation of the load-carrying capability of the joint, particularly under mode II where the propagation fracture toughness is reported to be 5 to 10 times higher than its initiation value (Figure 3.3).

3.4.2 Effect of the adhesive and adherend thickness on the fracture toughness

In Figures 3.3 (a) and 3.6 (a) the fracture toughness of the thick-adhesive specimens is shown to be higher than that of the thin-adhesive specimens. The increase in the fracture toughness with the adhesive thickness can be

explained by the larger plastic regions that can develop in a thicker adhesive. There is general agreement in the literature on the fact that the fracture toughness of an adhesive joint increases with the bondline thickness for thin adhesive layers (below 0.5 - 1 mm) [60, 61, 63, 64]. Under mode I loading, the value of the fracture toughness is reported to exhibit a maximum value when a certain thickness is attained and decrease slightly thereafter, down to a plateau value [60–63]. This plateau is reached for exceptional bondline thicknesses of several millimeters. Both the experimental works in [60, 61, 63] and the models presented in [60, 62] show that the increase in the fracture toughness corresponds to a transition from brittle fracture in very thin adhesive layers to the development of a plastic zone of increasing size as the bondline thickness grows, whereas the maximum value of the fracture toughness is attained when the plastic zone is fully developed.

In Section 3.4.1, the fracture of thick-adhesive specimens has been argued to involve shorter FPZ, as LEFM overestimation of the results is less severe. The previous asseveration might appear to conflict with the discussion given in this section, where thick adhesives are argued to involve larger regions of plastic deformation. However, the amount of plastic deformation can be explained by the higher volume of adhesive in thick adhesive layers, and does not necessarily involve larger FPZs.

Although the scatter in the experimental results for different adherend thickness is high, the adherend thickness is also shown in Figure 3.3 (c) and Figure 3.6 (c) to have an effect on the fracture toughness of the specimen. The thinner the adherend, the higher the fracture toughness is in most of the experiments. While fewer experimental works are available in the literature regarding the external effects on adhesive joints toughness, bond toughness has been also shown to depend on the stiffness of the adherends (see e.g. the work of Wang et al. [65] in mode I tests). More extensive is the research carried out in the field of delamination with fiber bridging, where the R-curve of the material exhibits a different behavior depending on the adherend thickness [25, 34]. This differences are attributed to the size of the FPZ, which is larger for thicker adherends [34]. Extending the previous statement to adhesive joints, higher bond toughness would also be expected for thicker adherends, which contradicts the observed dependence.

However, the numerical study developed by Pardoen et al. [62] showed that, under mode I, the bending of thinner adherends increases the rotations at the crack tip, which promotes shear yielding in the adhesive. As a consequence, even though specimens with thinner adherends have smaller FPZ, the plastic deformation in the crack tip is higher and so can be the bond toughness. This second parameter appears to be dominant in the experiments performed in this work, as thin-adherend specimens exhibit higher bond toughnesses.

Finally, it should be recalled that two specimens were tested for each configuration. More tests of each configuration would be required to analyze the relevance of the effects discussed in this section with respect to the specimen-to-specimen variation of the results.

3.5 Conclusions

An FM-300 epoxy film adhesive with carbon/epoxy adherends has been characterized under pure mode I and II by means of two different experimental data reduction methods based on LEFM and on the J-integral approach. The results from these two methods have been compared and their suitability to analyze adhesive joints has been discussed. The effect of both the adherend and the adhesive thicknesses on the fracture toughness and the R-curve of the adhesive have been investigated.

The results given by LEFM-based data reduction methods have been shown to be highly dependent on the length of the fracture process zone, presenting an increasing overestimation of the fracture toughness as the fracture process zone grows. The deviation of LEFM results with respect to those of the J-integral approach ranges from approximately 10% to 30% in pure mode I and 15% to 40% in pure mode II. Those geometries that imply larger fracture process zones, such as specimens with thicker adherends, result in the highest disagreement between LEFM and J-integral results. The same occurs with the loading mode, where mode II exhibit greater differences between LEFM and the J-integral than mode I as it involves larger fracture process zones. LEFM has been argued as not being suitable for the analysis of adhesive joints fracture, with the early stages of crack growth being the only scenario where LEFM could be expected to provide

a reasonable estimation of the initiation fracture toughness with an error that falls within the experimental scatter.

Both the adherend and the bondline thicknesses have been shown to have a significant impact on the fracture toughness of the adhesive joint. The trend observed is that thinner specimens result in higher fracture toughnesses for both mode I and II. Similarly, thicker adhesive layers also result in higher bond toughness. Both observations have been found to be in agreement with other experimental and numerical works available in the literature.

Chapter 4

An experimental analysis of the fracture behavior of composite bonded joints in terms of cohesive laws

Abstract. Modeling adhesive joints by means of cohesive zone models relies on the definition of cohesive laws, which depend on the loading mode mixity. There is, however, a lack of experimental information on the characteristics of the cohesive law as a function of the mode mixity. Other parameters, such as the adhesive and adherend thicknesses, are known to affect the fracture toughness of a bonded joint, but their effect on the cohesive law has not been clarified. In this work, an experimental characterization of an FM-300 epoxy film adhesive under pure-mode and mixed-mode conditions is presented. The effect that the adhesive and the adherend thicknesses have on the fracture toughness, the R-curve and the cohesive law of the joint is studied. Both the adherend and adhesive thicknesses are shown to have an impact on the bond fracture toughness and the cohesive law of the bonded joint. However, their impact on the cohesive law is minor compared to the influence of the mode mixity, which mainly defines its shape. The implications that the experimental findings in this work have on the numerical simulation of adhesive joints are also discussed.

4.1 Introduction

The mechanical properties of the bulk adhesive and the behavior of a thin adhesive layer confined in between two rigid adherends have been shown to be difficult to correlate [59]. The constraint of the stress field in the adhesive layer determines its plastic deformation, which severely affects the bond toughness [34, 60, 61]. On one hand, the adhesive thickness has been repeatedly shown in the literature to influence the bond toughness [60–64].

On the other hand, although fewer works are available in the literature regarding the characterization of the effect of the adherend thickness, the adherend stiffness also influences the fracture toughness [25, 34, 62, 65].

Adhesive joints usually involve large-scale fracture processes as a consequence of the large plastic and damage region developed ahead of the crack tip. A recent work by the authors [9] showed that limiting the characterization of adhesive joints to a Linear Elastic Fracture Mechanics (LEFM) framework can lead to unacceptable deviations in the fracture toughness measurement. Instead, the J-integral approach [4], defined in the framework of Non Linear Fracture Mechanics (NLFM), can serve that purpose. Different closed-form solutions of the J-integral that do not require LEFM assumptions are available in the literature for different fracture mechanics tests [8, 36, 40, 43, 44, 46], enabling the reliable characterization of adhesive joints under pure and mixed-mode loading.

In a finite element analysis framework, cohesive zone models [5] are an excellent approach for the analysis of adhesive joints fracture. They rely on a traction-separation law, which is assumed to be a material property dependent on the loading mode, that describes the behavior of the material due to plasticity and damage. Cohesive zone models can reproduce in detail the crack growth and the Fracture Process Zone (FPZ) behavior on a predefined interface. Under certain fracture processes involving small FPZs such as delamination in composite materials, accurate results are obtained by assuming any cohesive law shape provided that the amount of energy dissipated equals the fracture toughness of the material [13, 71]. However, in general situations where the FPZ might have a significant size, its generation and propagation can play a key role in the load-displacement curve and in the failure of adhesive joints and, therefore, a detailed analysis of the FPZ behavior is required to accurately simulate the joint response. In such situations, the traction-separation law (or cohesive law) of the material must be known, so it should be experimentally measured.

Cohesive law measurement methods are far more recent than those for fracture toughness measurement and the influence the bond geometry has on the cohesive law is still an ongoing research topic. Sørensen and coauthors [24–27, 30] developed the method for measuring cohesive laws originally proposed by Suo et al. [34] and extended it to mixed mode [26]. They

applied the method to characterize the bridging laws in delamination specimens [25, 27] and to characterize the effect of the loading rate in adhesive joints [24]. All these experiments were performed for a single adhesive and adherend thicknesses. More recently, Leone et al. [32] applied the same method to obtain the cohesive law of FM-300K adhesive under pure modes I and II; also for a single adhesive and adherend thickness. Ji and coauthors characterized the effect of the bondline thickness on the Hysol 9460 adhesive cohesive law under pure mode in both metallic [72] and carbon/epoxy composite joints [73, 74]. They observed a completely different effect of the bondline thickness on metallic and composite joints, which was attributed to the difference in the adherend stiffness. Ji and coauthors extended this study to mixed mode, albeit for metallic joints only [75]. However, the effect of the adherend thickness on the cohesive law of the adhesive has been never studied, and neither has the effect of the adhesive thickness on its cohesive law under mixed mode in composite joints.

In the current work, a thorough experimental characterization of the FM-300 epoxy film adhesive is presented. The R-curves and the cohesive laws of the adhesive joints are measured for four different loading modes: pure mode I, pure mode II and 50% and 75% of mixed mode I-II. The effects of both the adhesive and the adherend thickness on the fracture toughness and on the cohesive law of the joint are investigated for each loading mode by testing three different adherend thicknesses and two different adhesive thicknesses.

The experimental tests performed and the data reduction methods applied in this work are described in Section 4.2. The experimental results are presented in Section 4.3 and, in Section 4.4, they are discussed and compared to the observations in the literature.

4.2 Methodology

4.2.1 Material and specimen configuration

Two panels of unidirectional T800S/M21 carbon/epoxy prepreg for each batch of specimens were cured and then secondary bonded by means of an FM-300 epoxy film adhesive impregnated in a carrier. The specimens were 25 mm wide and 250 mm long. The Teflon insert that triggers in-

terface debonding was 60 mm long. The layup of the specimens and the different adhesive and adherend thicknesses tested are outlined in Table 4.1. Three different adherend thicknesses were manufactured by stacking a different number of layers, whereas the two different adhesive thicknesses were achieved by using one or two layers of adhesive.

Specimen codes	Specimen total thicknesses (mm)	Layup	Adhesive thickness (mm)
A1T1	3.12 ± 0.06	$[0]_8/d/[0]_8$	0.21 ± 0.02
A2T1	4.60 ± 0.08	$[0]_{12}/d/[0]_{12}$	0.21 ± 0.02
A2T2	4.80 ± 0.10	$[0]_{12}/d/[0]_{12}$	0.37 ± 0.01
A3T1	6.05 ± 0.23	$[0]_{16}/d/[0]_{16}$	0.21 ± 0.02

Table 4.1: Specimen configurations tested. In the layup definition, d denotes the insert location.

4.2.2 Tests and data reduction method

Double Cantilever Beam (DCB) [67], End Notched Flexure (ENF) [68] and Mixed Mode Bending (MMB) [19] tests were performed to characterize the adhesive under pure mode I, pure mode II and mixed mode loading, respectively. In Figure 4.1, the configuration of each test is schematically shown.

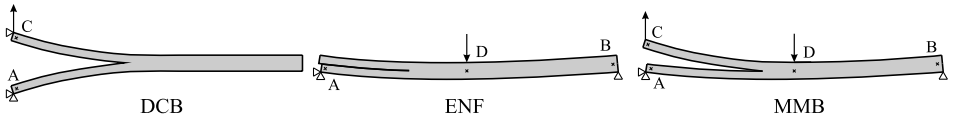

Figure 4.1: Representation of the load introduction in the three test types performed in this work.

Thirty-two tests in total were carried out. Two DCB, ENF, MMB 50% and MMB 70% tests were performed for each material configuration in Table 4.1. The experimental data were reduced using J-integral closed-form solutions available in the literature. Details of the equations used can be found in the description of each particular test.

The cohesive laws were computed according to [26] as

$$\sigma = \frac{\partial J}{\partial \Delta} \tag{4.1}$$

where σ is the cohesive traction, J is the J-integral measured according to the equations for each particular test and Δ is the total crack separation, which in the present work was measured by means of the Digital Image Correlation (DIC) equipment described in Section 4.2.3. The method given by Equation (4.1) is derived assuming that the measurements are taken while the FPZ is being formed [24], so the precracking step outlined in the test standards was skipped.

In this work, mixed-mode cohesive laws were derived by means of Equation (4.1). By doing so, the cohesive traction is assumed to be in the direction of the opening displacement, which has not been confirmed by experimental observations. An alternative method for measuring the mixed-mode cohesive law would be, as described in [26], the partial differentiation of J with respect to normal and tangential separations, which would provide the normal and tangential cohesive tractions separately. However, in the derivation of the method in [26], cohesive laws are assumed to be path independent (i.e. the work of the cohesive tractions is independent from the loading history). Therefore, either the alignment between cohesive tractions and separations or the path independence of cohesive laws needs to be assumed. In view of the lack of experimental evidence that confirm which of the two assumptions is the most appropriate, Equation (4.1) has been used in this work for convenience in the comparison to pure-mode cohesive laws.

DCB test

The procedure described in the ISO25217 test standard [67] was followed to perform the DCB tests. The initial crack length was set to 35 mm for all tests by bonding the load introduction blocks at the corresponding distance. J_c was computed by means of the expression proposed by Paris and Paris [43] as

$$J = \frac{2P}{b}\theta \tag{4.2}$$

where b is the specimen width, P is the applied load and θ is the rotation angle at the load introduction point. The angles at both the upper and lower load introduction points of the DCB specimen were monitored in order to remove the initial rigid body rotations (points A and C in the DCB specimen in Figure 4.1).

ENF test

The three point bending ENF tests were done based on the procedure described in the test method AITM 1.0006 [76]. Longer crack propagation than that obtained in the standard was desired, so the distance between supports was set to 120 mm and the initial crack length was set to 35 mm. The J-integral closed-form solution for the ENF test proposed by Stigh et al. [46] was used for computing J_c as

$$J = \frac{P}{2b}(\theta_A - 2\theta_D + \theta_B) \tag{4.3}$$

where b is the specimen width, P is the applied load and θ_A, θ_B and θ_D are the rotation angles at the load introduction points, as depicted in Figure 4.1.

MMB test

The MMB tests were done according to the procedure described in the ASTM D6671M-13 test standard [19]. The distance between supports was set to 150 mm for all the tests performed in order to achieve a longer crack propagation than that of the standard, whereas the initial crack length was set to 40 mm. The MMB lever arm was set for each particular test according to the ASTM standard [19], depending on the specimen thickness and the aimed mixed-mode ratio. The term *aimed* here refers to the mode mixity defined in an LEFM framework. Its definition is valid for, at least, early stages of crack growth, when the FPZ is still small. For larger FPZ, the mode mixity becomes undefined in an LEFM sense and raises the discussion on how the mixed-mode ratio should be defined under large-scale fracture, which is outside the scope of the current work.

J_c was computed using the J-integral closed-form solution for the MMB test recently proposed by the authors [8] as

$$J = \frac{P}{b}\left[\left(\frac{1}{2} - \frac{c}{2L}\right)\theta_A + \left(\frac{c}{2L} + \frac{1}{2}\right)\theta_B + \frac{c}{L}\theta_C - \left(\frac{c}{L} + 1\right)\theta_D\right] \quad (4.4)$$

where b is the specimen width, P is the applied load, c is the MMB lever arm and θ_A, θ_B, θ_C and θ_D are the rotation angles at load introduction points, as depicted in Figure 4.1. θ_A and θ_C refer to the lower and upper arms on the cracked end of the specimen, respectively, θ_B refers to the specimen's uncracked end and θ_D refers to its mid-span length point.

4.2.3 Instrumentation

Crack length was visually monitored in order to have an approximate value for representation purposes only, as it is not required for the data reduction methods used in this work. It was visually monitored by marking specimens along one edge with vertical lines every 1 mm and tracking the crack front with a Canon 550D camera with a macro lens mounted on a traveling fixture.

The other edge of the specimen was painted with a random black speckle pattern on a white background in order to monitor the crack tip displacement field by means of a Digital Image Correlation (DIC) system. Two cameras from a DIC stereo system were used to monitor the three dimensional displacement field at the crack tip region. Vic-3D 2012, developed by Correlated Solutions Inc and equipped with two cameras (resolution of 2452x2056 pixels^2) and two Rodagon 1:4.0 lenses with a focal length of 60 mm, was used. Extension tubes were employed to adjust the DIC vision area to an approximate size of 12.5x15 mm^2. The lens aperture was set to f/11 to provide a sufficient depth of field for all tests. The shutter time was then adjusted to between 10 and 40 ms for each particular test depending on the lighting conditions. Conversion factors of 6 μm/pixel were approximately achieved for all tests. Given that the maximum resolution of the Vic-3D system is 0.01 pixel, the maximum theoretical spatial resolution for the tests performed is around 0.06 μm. In practice, the maximum noise

level in the displacement field measured from the first images with no actual displacement applied was observed to be between 0.2 and 0.8 μm for all tests.

Depending on the test type, two to four inclinometers were installed at load introduction points. Two inclinometers were used for DCB tests (points A and C in Figure 4.1), three for ENF (points A, B and D in Figure 4.1) and four for MMB (points A, B, C and D in Figure 4.1). The NA3-30 capacitive dielectric liquid-based inclinometers from SEIKA Mikrosystemtechnik GmbH were used. The NA3-30 inclinometer has a measurement range of $\pm 30^\circ$ and, according to the manufacturer's specifications, a resolution below 0.005° with a maximum linearity deviation over the whole measurement range of 0.06°.

A picture of the entire setup for an MMB test can be seen in Figure 4.2, where pictures taken during test by the cameras on either side of the specimen are also presented.

The load, displacement and inclinometer data were acquired at 20 Hz. 3 pictures/second were taken with both the DIC and the crack length monitoring cameras. All the systems were synchronized using a common displacement channel.

The tests were performed under displacement control at a constant displacement rate in a servohydraulic MTS 858 testing machine using a 5 kN load cell. Given the different compliance of the specimens, the displacement rate applied was different for each test and specimen thickness and ranged from 0.5 mm/min to 2.0 mm/min. The displacement rates applied were low enough as to ensure quasi-static crack growth according to test standards [19, 67, 68].

4.3 Results

The results of the 32 tests performed (2 specimens for each DCB, ENF, MMB 50% and MMB 75% of each specimen type in Table 4.1) are presented in this section, while the analysis and discussion of the results are provided in Section 4.4.

The load-displacement curves are presented in Figure 4.3. Stable crack propagation was obtained for most of the tests, except for the following

specimens: one A2T1 specimen, one A2T2 and the two A3T1 from the MMB 50% test (Figure 4.3(c)) and one A2T1 and A3T1 specimen from the MMB75% test (Figure 4.3(d)). Unstable crack propagation resulted in jumps in the load-displacement curve, which have been removed from the graphs for the sake of clarity. Only initiation values of the fracture toughness are therefore available for these specimens, whereas the whole R-curve was obtained for all the other tests performed. The complete cohesive law of the unstable specimens could not be obtained, as the FPZ had not

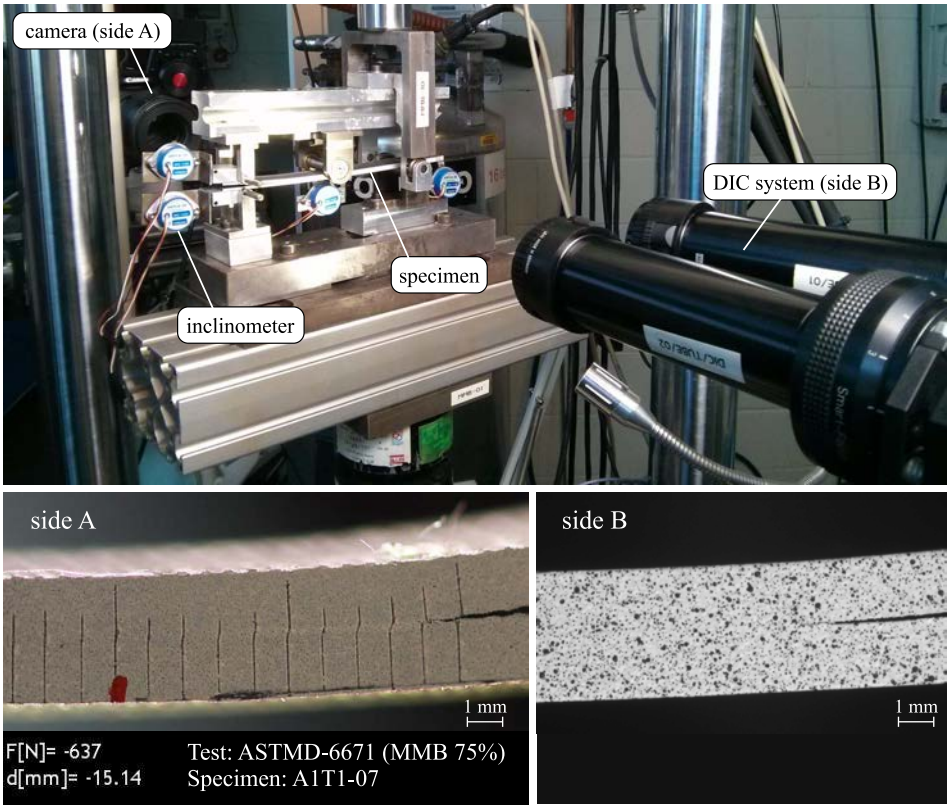

Figure 4.2: Experimental setup for an MMB test and pictures taken by the cameras on either side of the specimen for monitoring the crack length (side A) and measuring the crack opening displacement (side B).

been fully generated when sudden crack propagation occurred. Data from only one A3T1 specimen are available for the ENF test (Figure 4.3(b)) because of a malfunction in the acquisition of the load channel.

The fracture toughness results for each adhesive and adherend thickness are presented in Figures 4.4 and 4.5, respectively. The fracture toughness results are plotted against crack extension. However, it should be noted that in presence of large FPZ the crack tip is vaguely defined, so the representation of the x-coordinate might be inaccurate. Nevertheless, the crack length is not used in the computation of J_c and only has an influence on the graphical representation.

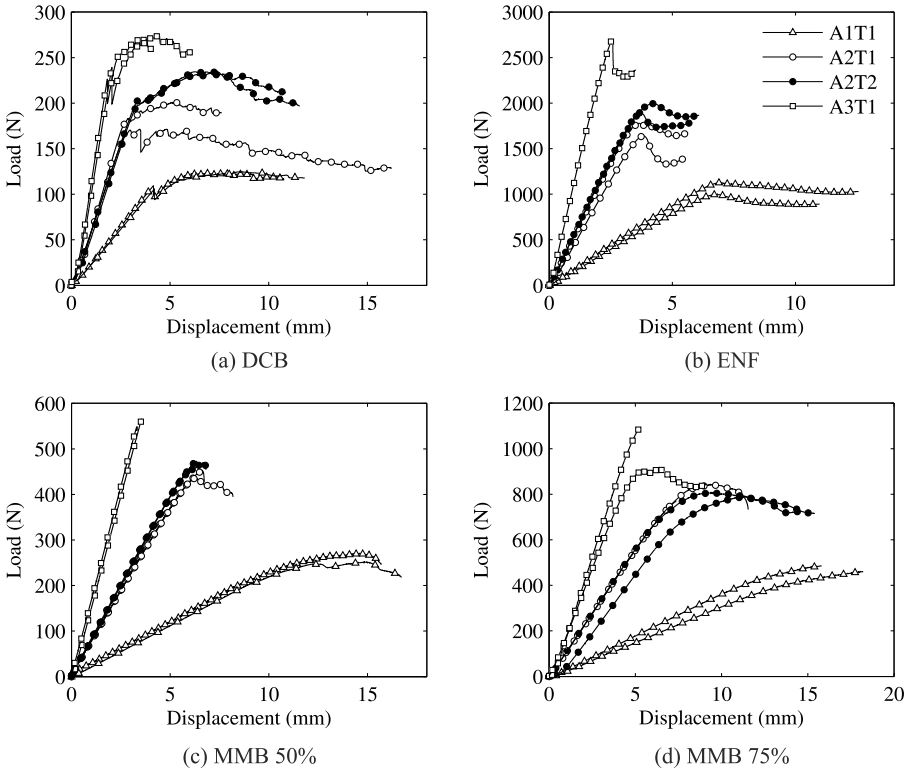

Figure 4.3: Load-displacement curves (only 1 out of every 1000 points is depicted for clarity).

A summary of all the initiation and propagation fracture toughness values is presented in Figure 4.6. Crack initiation has been determined visually, whereas the crack propagation value refers to the average fracture toughness value of the R-curve plateau.

Cohesive laws have been computed from the derivative of the $J - \Delta$ curves, as described in Section 4.2.2. Both the $J - \Delta$ curves and the cohesive laws are presented in Figures 4.7 - 4.10 for the DCB, ENF, MMB 50% and MMB 75% tests conducted, respectively, with the exception of one A1T1 specimen for the MMB 50% test because of a failure in the DIC

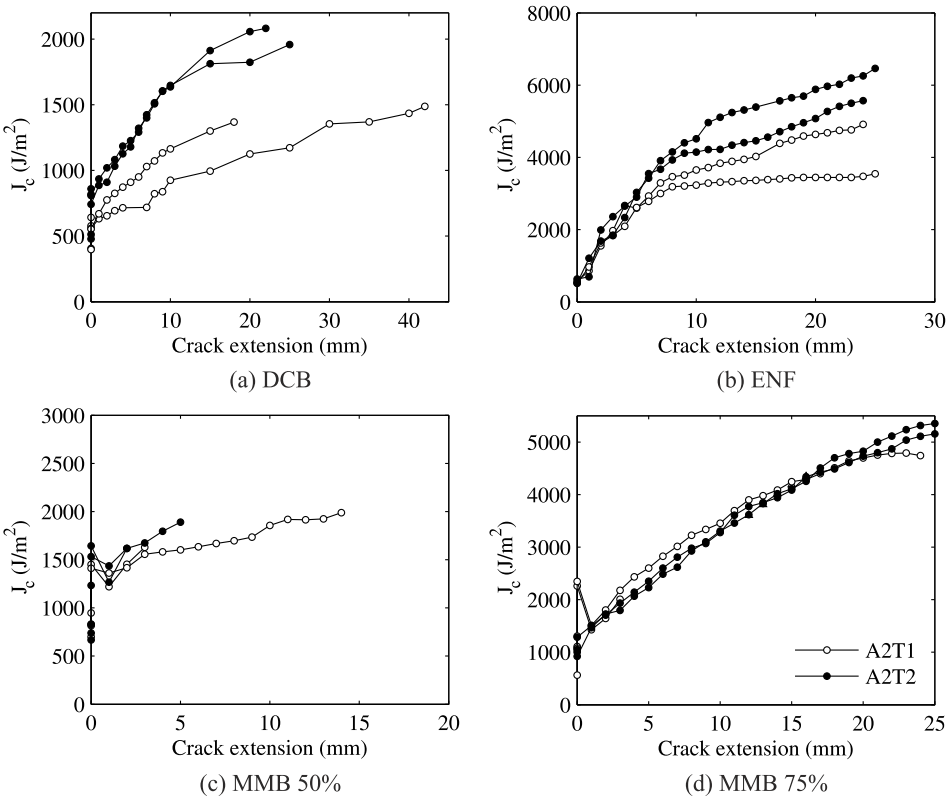

Figure 4.4: Influence of the adhesive thickness on the fracture toughness of the adhesive joint.

data acquisition.

Stick-slip behavior was observed during the early stages of crack growth for many of the DCB tests. Stick-slip behavior can be identified by small jumps of the load in the load-displacement curves (Figure 4.3 (a)). In these cases, the cohesive law measured is not complete, as can be observed in Figure 4.7 (b).

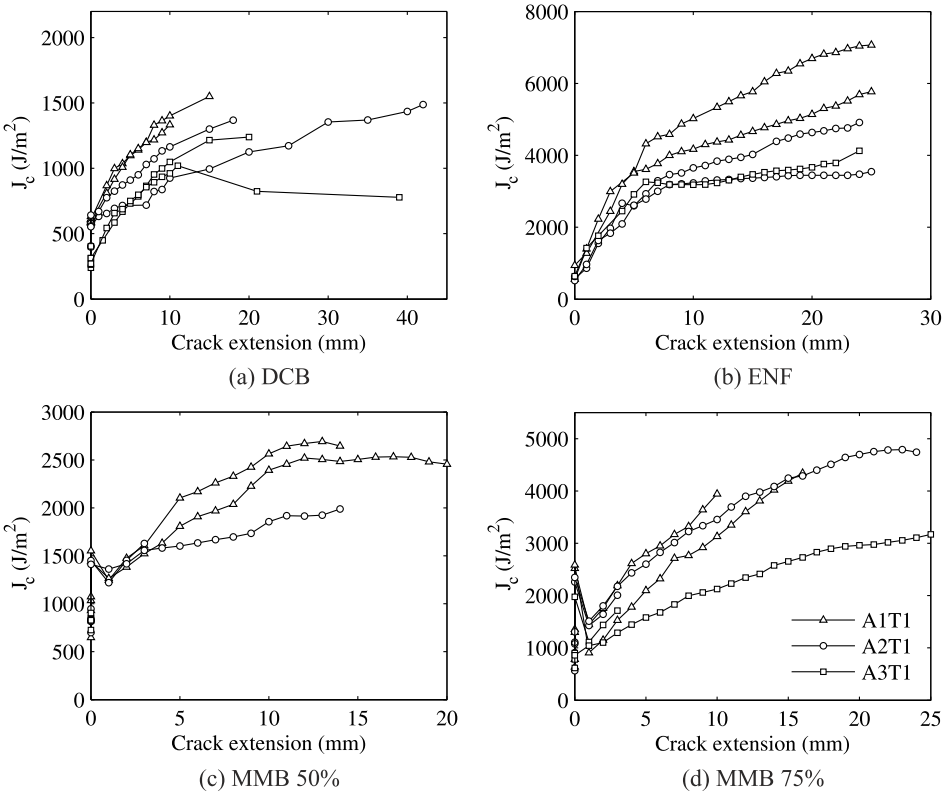

Figure 4.5: Influence of the adherend thickness on the fracture toughness of the adhesive joint.

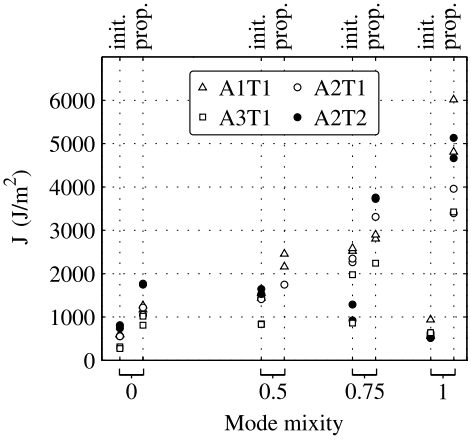

Figure 4.6: Summary of the initiation and propagation fracture toughness values obtained as a function of the aimed mode mixity.

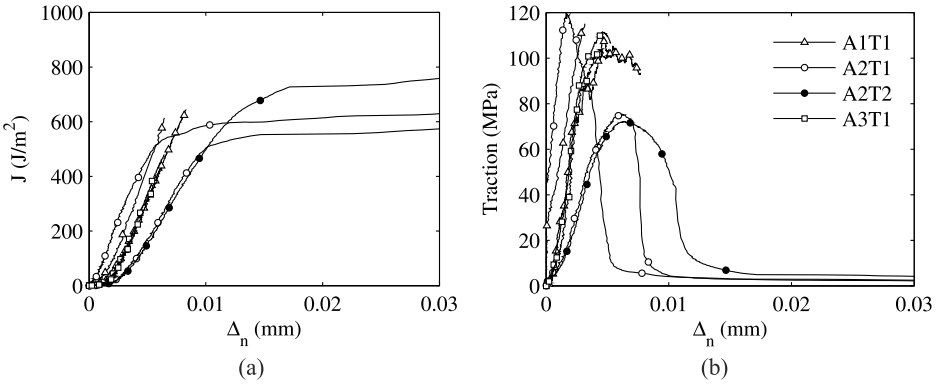

Figure 4.7: J vs. crack tip opening displacement (a) and measured cohesive laws (b) of the DCB tests conducted. Only 1 out of every 50 points is depicted for clarity.

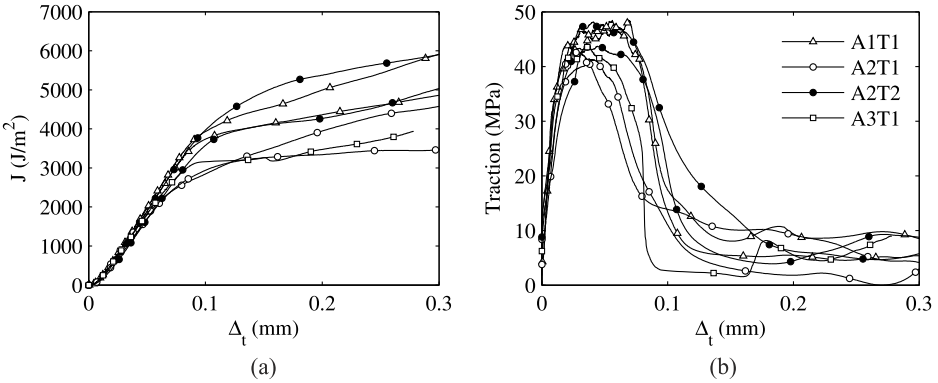

Figure 4.8: J vs. crack tip shear displacement (a) and measured cohesive laws (b) of the ENF tests conducted. Only 1 out of every 100 points is depicted for clarity.

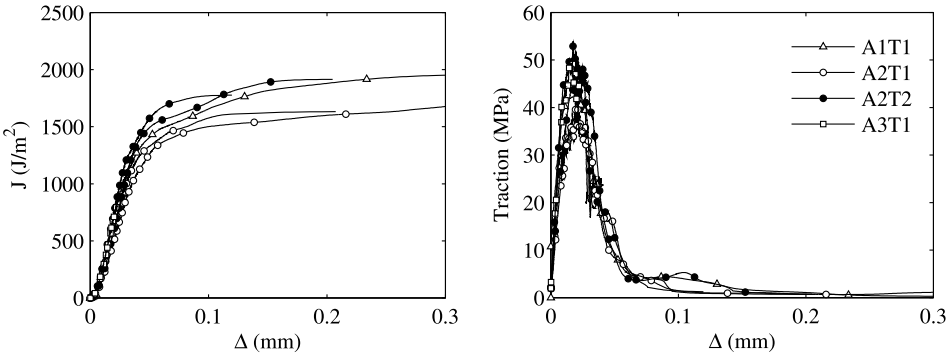

Figure 4.9: J vs. crack tip opening and shear displacements norm (a) and measured cohesive laws (b) of the MMB 50% tests conducted. Only 1 out of every 100 points is depicted for clarity.

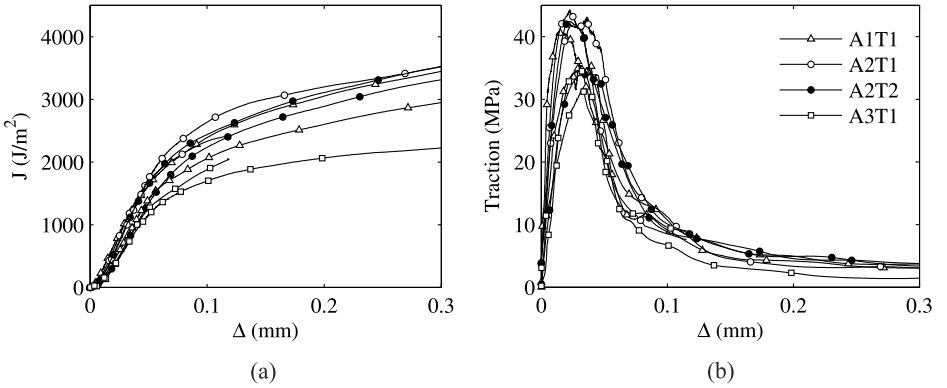

Figure 4.10: J vs. crack tip opening and shear displacements norm (a) and measured cohesive laws (b) of the MMB 75% tests conducted. Only 1 out of every 100 points is depicted for clarity.

4.4 Discussion

The fracture toughness of the thick-adhesive specimens in Figure 4.4 is clearly shown to be higher than that of the thin-adhesive specimens under pure-mode loading, whereas this difference is less pronounced in the mixed mode configurations. The adherend thickness is also shown to have an effect on the fracture toughness of the specimen in Figure 4.5, although a high scatter in the experimental results is observed. The thinner the adherend, the higher the fracture toughness is in most of the experiments. The propagation fracture toughness values in Figure 4.6 are clearly shown to be higher than the initiation values. This difference is emphasized under mode-II-dominant fracture, which is in agreement with the larger FPZ length expected for mode II [69, 70].

In a recent work by the authors [9], the pure-mode results presented in the current work were used along with the results of LEFM experimental data reduction methods in order to assess the validity of LEFM to characterize adhesive joints. In [9], a discussion was given that contrasted the pure-mode results with the observations in the literature for both the effect of the adhesive [60–64] and the adherend [25, 34, 62, 65] thicknesses. Regarding the effect of the adhesive thickness, it was concluded that thicker adhesives can develop larger areas of plastic deformation, and therefore have a higher bond toughness. With regards to the effect of the adherend, thin-adherend specimens result in larger rotations at the crack tip that promote shear yielding, which increases plastic deformation and thus the bond toughness [62].

The effect of the adhesive and adherend thicknesses on the fracture toughness described above must correlate with the measured cohesive laws, which govern the joint behavior. However, as discussed next, the measured cohesive laws also evidence that the effect of the adherend and adhesive thicknesses is small if compared to the effect of the mode mixity, which mainly defines their shape.

The mode I cohesive laws shown in Figure 4.7 (b) exhibit low repeatability that arises from the limitations in the experimental measurement method and equipment. The fact that the measured crack tip opening displacement for the DCB test is one order of magnitude below that of the

ENF and MMB tests should also be taken into account. This fact implies that a small imprecision in locating the crack tip for the measurement of the crack tip opening displacement can result in substantial differences in the horizontal axis of Figure 4.7 (a). Also, as stated in Section 4.3, the stick-slip behavior observed during the early stages of crack growth for many of the DCB tests led to an incomplete measurement of their cohesive law. The method to measure cohesive laws can only be applied during the formation of the FPZ. This limitation of the method implies that material imperfections, such as a resin pocket at the insert tip, may have a significant influence on the measured cohesive law. The previous shortcomings in the measurement of mode I cohesive laws hinder the analysis of their dependence on the adhesive and adherend thicknesses. However, the dependence of the cohesive law on the adhesive and adherend thicknesses might be of little relevance. Mode I cohesive laws show a steep profile both prior to and after damage initiation. That resembles the behavior of an interface that would fall within the scope of LEFM, for which the interlaminar strength would be very large and the crack tip opening displacement corresponding to full damage would tend to zero. The area below the traction-separation curve would therefore be the only parameter required to describe the fracture process. Hence, the shape of the measured mode I cohesive laws denotes a relatively small FPZ in the DCB tests, which is also in agreement with the observations in the literature [69, 70].

On the other hand, mode II cohesive laws (Figure 4.8 (b)) exhibit a plateau in the maximum traction values, which indicates that the interface is undergoing significant plastic deformations prior to damage initiation. This observation is in agreement with the larger plastic deformations under shear loads that similar adhesives have been shown to exhibit in bulk adhesive tests in the literature [77]. The extent of plastic deformations - and also the area below the traction-separation curve - is greater for the thick-adhesive specimens and for the thin-adherend specimens, denoted by a filled circle and a triangle, respectively, in Figure 4.8. This observation is in agreement with the discussion above, where the higher fracture toughness of these two types of specimen is attributed to the greater extent of plastic deformations.

The effect of the adherend and adhesive thicknesses on the cohesive law

is less marked under mixed-mode loading conditions (Figures 4.9 and 4.10 (b)), similar to the trend observed for the fracture toughness. The interpretation of the mixed-mode results is not straightforward. It is relevant to highlight that the mixed-mode ratio at the crack tip is not kept constant during the test, as shown in Figure 4.11. Fracture is mode-II dominant during the first stages of crack growth and progressively changes to mode I as damage grows. A similar evolution of the local mode ratio has already been reported experimentally [41] and numerically [13, 71]. It is further observed in the current work that the local mixed-mode evolution during fracture is heavily dependent on the adherend thickness for the MMB 75% test, but not on the adhesive thickness (Figure 4.11 (b)). This dependence is either nonexistent or small enough to fall within the experimental accuracy for the MMB 50% test (Figure 4.11 (a)). Such local mixed-mode ratio variation can explain why the experimental observations for pure mode differ from those for mixed mode.

The tractions of the fully damaged interface (for large crack opening

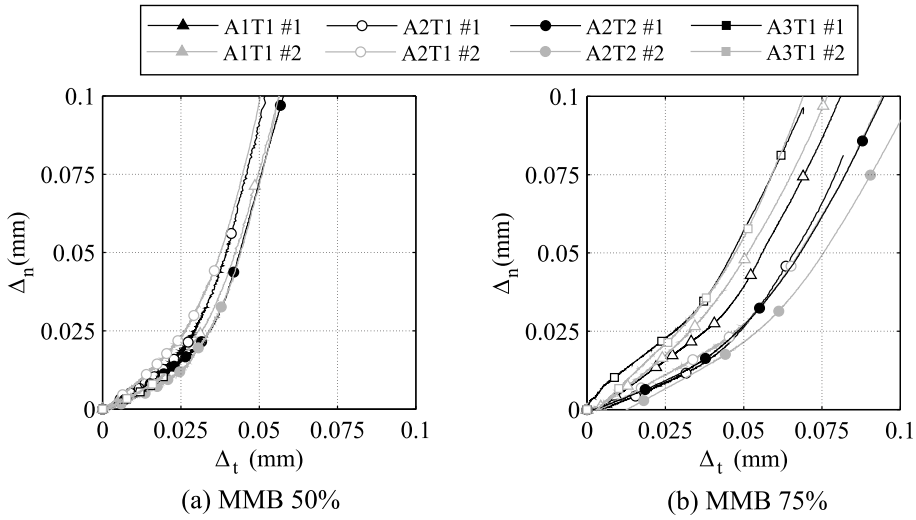

Figure 4.11: Mode I (Δ_n) against mode II (Δ_t) crack tip opening displacements for the MMB (a) 50% and (b) 75% tests (only 1 out of every 200 points is depicted for clarity).

displacements) tend to a steady value, as can be seen from Figures 4.7 - 4.10 (b). This value is zero for mode I fracture (Figure 4.7 (b)) and almost zero for the MMB 50% (Figure 4.9 (b)), which indicates that the interface is not able to transfer loads after being damaged. However, the remaining traction progressively increases for the MMB 75% (Figure 4.10 (b)) and the ENF (Figure 4.8 (b)) tests. Such remaining traction might be an indicative of the presence of friction in the fractured interface, as it becomes higher for shear-dominated fracture.

In regards to the detailed modeling of adhesive joints and their FPZ, it can be concluded from the previous observations that the behavior of each loading mode must be accurately accounted for in the traction-separation law that feeds the numerical model. The existing cohesive models rely on the definition of initiation and propagation parameters that depend on the mode mixity, but they do not take into account the change in the shape of the cohesive law [5]. This shape variation as a function of the mode mixity is qualitatively shown in Figure 4.12. It can be observed how the behavior of mode-I fracture resembles the behavior of LEFM, but also that this behavior rapidly disappears as the mixed-mode increases. The

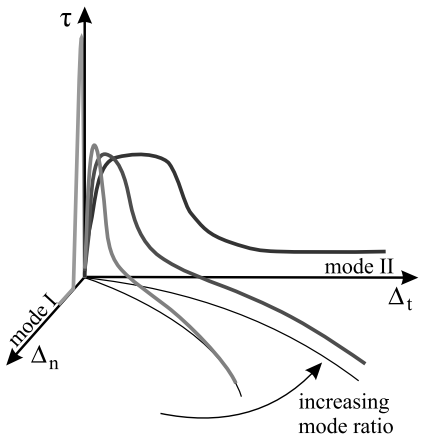

Figure 4.12: Idealized FM-300 cohesive laws as a function of the aimed mode mixity. Mode I cohesive laws resemble the behavior of LEFM, which rapidly disappears as the interface plasticity increases for increasing mode mixity.

interlaminar strength rapidly decreases for low mode mixtures, whereas the fracture toughness increases together with plastic deformations previous to damage. The remaining interface traction, i.e. the cohesive law tail, is also shown to increase with the mode mixity. The qualitative representation of the mixed-mode cohesive laws in Figure 4.12 follows a nonlinear path in the $\Delta_n - \Delta_t$ space, which is done for consistency with the experimental evidence shown in Figure 4.11.

4.5 Conclusions

The fracture behavior of adhesive joints made of an FM-300 epoxy film adhesive with carbon/epoxy adherends has been characterized by means of J-integral-based experimental data reduction methods. The effect of both the adherend and the adhesive thicknesses on the fracture toughness, the R-curve and the cohesive law of the adhesive have been investigated for four different loading modes: pure modes I and II and mixed modes of 50% and 75%.

Both the adherend and the bondline thicknesses have a significant impact on the fracture toughness of the adhesive joint. However, the shape of the measured cohesive laws is mainly defined by the mode mixity. Failure is more brittle under mode I loading, whereas a progressive increase in plasticity prior to damage initiation is observed as the percentage of mode II increases. The remaining tractions that the interface is able to sustain are zero for mode mixtures of 50% and below and increase for high percentages of mode II, which can be explained by friction in the fractured interface. The effect of the adhesive and adherend thicknesses is also reflected in the measured cohesive laws. However, this effect is minimal compared to the influence of the mode mixity and its quantification is on the threshold of the used experimental measurement capabilities.

Cohesive law measurement is still a challenging research topic because of the difficulties that arise from the existing measurement methods. The crack tip opening displacements that must be directly measured are small, so measurement methods with better resolutions would be desirable. In addition, the method to measure cohesive laws can only be applied during the formation of the FPZ, which makes the measured cohesive law sensitive

to material imperfections in the particular region where the FPZ is being formed.

Part II

Numerical simulation of adhesive joints

Chapter 5

Assessment of energy dissipation during mixed-mode delamination growth using cohesive zone models

Abstract. The use of cohesive elements to simulate delamination growth involves modeling the inelastic region existing ahead of the crack tip. Recent numerical and experimental findings indicate that the mixed-mode ratio varies at each material point within the inelastic region ahead of the crack tip during crack propagation, even for those specimens whose mixed-mode ratio is expected to be constant. Although the local variation of the mode mixity may adversely affect the predicted numerical results, most existing formulations do not take it into account. In this work, the mode-decomposed J-integral is implemented as a finite element post-processing tool to obtain the strain energy release rates and the mixed-mode ratio of the inelastic region as a whole, allowing the assessment of crack propagation in terms of energy dissipation and mixed-mode ratio computation. Different cohesive elements are assessed with this method.

5.1 Introduction

The well-known advantages of composite materials, such as their excellent resistance and stiffness to weight ratios, have to coexist with some limitations. The difficulty of predicting composite failure is a major disadvantage that requires the use of conservative design margins and high developmental costs due to the large amount of testing needed. The development of advanced computational tools leads to the reduction of the number of tests needed and their associated costs. Among several failure mechanisms that exist in fiber-reinforced composites, delamination is one of the most critical

[78] as it limits the performance of composite materials in safety-critical structures. Consequently, the use of reliable numerical models to provide designers with the knowledge needed of when delamination may appear and how it may propagate would lead to improved designs and reduced development costs.

The most widely-used approach [79] to simulate delamination within the framework of finite elements and Linear Elastic Fracture Mechanics (LEFM) is the Virtual Crack Closure Technique (VCCT) [80]. LEFM-based techniques require the preexistence of a crack and their application is limited to materials whose Fracture Process Zone (FPZ), *i.e.* the damaged inelastic region ahead of the crack tip, is small enough in comparison with the relevant dimensions of the component. However, for materials with larger FPZ, LEFM is not applicable and the study of delamination requires the modeling of the FPZ. Cohesive Zone Models can be used to simulate delamination with no restriction in the FPZ size and no need of an existing crack. Therefore, the main advantages of cohesive elements with respect to VCCT are their wider range of application and the capability of capturing crack initiation as well as crack propagation.

The concept of modeling fracture with cohesive laws was introduced by Dugdale [6] and Barenblatt [7] and its main assumption is that the inelasticity of the FPZ can be collapsed into a surface ahead of the crack tip. Tractions and separations at this surface are linked by a cohesive law that relates them to a damage variable evolving from zero (intact material) to one (totally damaged material). Cohesive zone models are widely used in delamination analysis and many different cohesive element formulations have been proposed in the past years [81–90]. However, two main difficulties concerning cohesive elements robustness and their application to large-scale structures still exist. Firstly, fine meshes are required to appropriately model the FPZ, which leads to high, and sometimes unaffordable, computational requirements. Secondly, recent findings indicate that the mixed-mode crack propagation predicted by cohesive elements might be unreliable as a consequence of an improper estimation of the energy dissipated during the fracture process. The current paper addresses this last difficulty.

When a crack grows under mixed-mode loading, a mixed-mode ratio

is defined as the ratio between the mode II and the total strain energy release rates. In LEFM-based techniques, this definition is unique as the crack tip is unequivocally defined (see Figure 5.1 (a)). However, when using cohesive elements to simulate delamination, the mixed-mode ratio is computed locally at each integration point within the FPZ (see Figure 5.1 (b)), which allows the mixed-mode ratio to vary along the FPZ. The variation of the mixed-mode ratio within the FPZ has been recently observed in both numerical simulations [71] and experimental tests [41].

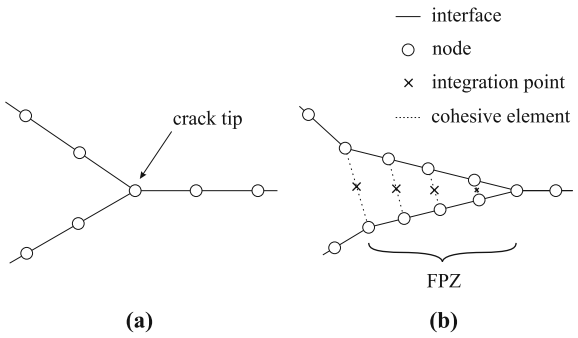

Figure 5.1: Crack tip representation when using (a) LEFM-based techniques and (b) cohesive elements.

Cohesive formulations are mainly driven by two measurable material properties (depicted in Figure 5.2): the fracture toughness ($\mathcal{G}_c$) and the interlaminar strength (τ^0). Generally, the interface properties are different for modes I and II, so a mixed-mode law needs to be implemented to define the cohesive law for any value of the mixed-mode ratio.

When the FPZ is small enough for LEFM to be applicable, crack growth should only be driven by fracture toughnesses and the interlaminar strengths should not affect the dissipated energy. However, as observed by Sørensen et al. [29] and confirmed in a recent work by Harper et al. [91], in some cases the interlaminar strengths severely affect the numerical results. Turon et al. [71] studied this phenomenon on the cohesive zone formulation they presented in [88], and they observed that under some conditions their formulation may not dissipate the expected amount of energy. Prior to the work of Turon et al. [71], it had not been observed that, although the ap-

plied mixed-mode ratio was kept constant, the mixed-mode ratio computed locally at each integration point varied severely along the FPZ. The local variation of the mixed-mode ratio caused the incorrect estimation of the dissipated energy.

The goals of the current work are, firstly, to investigate how the recently-observed mixed-mode variation is related to the improper energy dissipation in different cohesive formulations and, secondly, to assess the accuracy of the numerical results provided by these formulations when using different interlaminar strengths. The assessed formulations are those available in the commercial finite element codes Abaqus [15] and Ansys [92] and the formulation proposed by Turon et al. [88].

The assessment of energy dissipation during mixed-mode delamination growth is made by means of the mode-decomposed J-integral approach [47, 48]. As detailed later in the Methodology section, the J-integral in notched specimens for which LEFM is applicable is equivalent to the strain energy release rates at the crack tip [93]. The J-integral approach was first introduced by Rice [4] and it has been widely used as a non-linear energy release rate parameter to characterize crack propagation in metals. Additionally, the J-integral approach has been recently used in conjunction with quasi-brittle materials to characterize experimentally traction-separation laws [24, 25, 94]. In the current paper, the J-integral approach

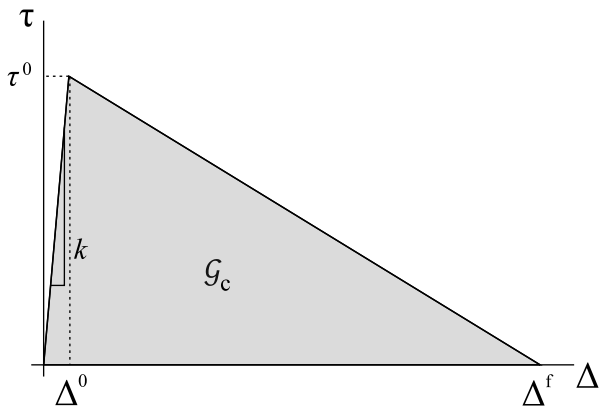

Figure 5.2: Fixed mixed-mode ratio cohesive law.

is also applied together with quasi-brittle materials. The new contribution of this work is the implementation of the J-integral approach as a finite element post-processing tool in its mode-decomposed form. By means of this tool, the mode-decomposed energy release rates during the simulation of delamination with cohesive elements are computed. These energy release rates refer to the FPZ as a whole, so an "average" mixed-mode ratio of the FPZ can be computed from a global point of view and not at each material point as done with cohesive elements. The information provided by the J-integral post-processing tool is used to assess the energy dissipation and the mixed-mode ratio computation of the cohesive formulations analyzed.

Three different definitions of the mixed-mode ratio have been given so far in this work. As these definitions will be referred to in all this work, it is worth to gather them together here to emphasize the existing differences among them:

- ▷ LEFM mixed-mode ratio or applied mixed-mode ratio (B_{LEFM}): it is computed using LEFM closed-form solutions. This is the mixed-mode ratio applied to the specimens and so the expected mixed-mode ratio for delamination growth.

- ▷ Local mixed-mode ratio (B_{coh}): is the value computed at any integration point within the FPZ. Its definition depends on the cohesive formulation.

- ▷ Global mixed-mode ratio (B_{J-int}): this new definition is based on the mode-decomposed strain energy release rates obtained by means of the mode-decomposed J-integral approach, as detailed in the methodology section. It is called "global" mixed-mode ratio because it represents the mixed-mode ratio of the FPZ as a whole, which differs from the local definition of cohesive formulations (at each integration point).

A Mixed Mode Bending (MMB) specimen was simulated using the three aforementioned cohesive formulations. Different interlaminar strengths were used and different mixed-mode ratios were applied. The results obtained show that, although in some of the cases the dissipated energy is not correctly estimated, in all of them the global mixed-mode ratio (B_{J-int}) is

in close agreement with the applied mixed-mode ratio (B_{LEFM}). Thus, the estimation of the mixed-mode ratio is not the reason for the incorrect energy dissipation. The non-constant value of the local mixed-mode ratio (B_{coh}) observed by Turon et al. [71] is shown to be consistent with the constant global mixed-mode ratio (B_{J-int}) obtained.

The cohesive formulation implemented in Abaqus [15] was found to predict incorrectly the dissipated energy and the associated load-displacement response under mixed-mode loading. On the other hand, one of the formulations implemented in Ansys [92] provides accurate numerical results, proper energy dissipation and correct mixed-mode ratio estimation for any value of interlaminar strengths used. Finally, the formulation proposed by Turon et al. [88] was already shown to correctly compute the dissipated energy and yield accurate numerical results in [71]. In the current work it is shown that the mixed-mode ratio estimation is correct and that its local variation is consistent with the constant mixed-mode ratio applied.

The paper is structured as follows. The methodology used to apply the J-integral approach in conjunction with cohesive elements is presented, preceded by an overview of both the J-integral formulation and its mode decomposition. After that, the results obtained are summarized, followed by a discussion about the energy dissipation and the mixed-mode ratio estimation of the three formulations assessed. Finally, some concluding remarks are given.

5.2 The J-integral approach: definition and mode decomposition

In this section, the general formulation of the J-integral approach is presented, followed by an overview of the mode-decomposed J-integral formulation used to finally obtain the mode-decomposed strain energy release rates. For further details of the derivation of the J-integral and the justification of its path independence the reader may refer to [4, 95]. If more details of the mode-decomposed formulation are needed, refer to [47, 48].

The path-independent contour integral known as J-integral was first introduced by Rice [4], who defined it as the decrease of potential energy per increment of cracked surface in a nonlinear elastic material. Consider

a solid homogeneous body with elastic behavior in a state of static equilibrium under the action of tractions T_k. For the particular case of the two-dimensional plane elastic problem, the J-integral is defined as

$$J_\Gamma = \int_\Gamma \left[\omega dy - T_k \frac{\partial u_k}{\partial x} ds \right] (k = 1, 2) \tag{5.1}$$

where Γ is a closed path surrounding the notch tip and bounding a region R (see Figure 5.3), u_k is the displacements vector and ds an infinitesimal arc length along Γ. The elastic energy ω of the body is defined as

$$\omega = \int_0^{\epsilon_{kl}} \sigma_{ij} d\epsilon_{ij} \tag{5.2}$$

where σ_{ij} and ϵ_{ij} are the stress and strain tensors, respectively.

The tractions vector T_k is given by

$$T_k = \sigma_{ij} n_i \tag{5.3}$$

where n_i denotes the normal vector to the bounding path Γ (see Figure 5.3).

If the closed contour Γ is free of singularities, the integral computed according to Equation (5.1) is proved to be path independent and its value is zero for any arbitrary contour Γ chosen [4, 95]. Then, from Figure 5.3,

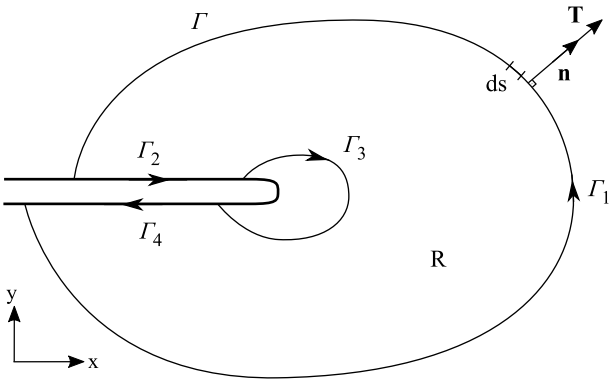

Figure 5.3: Integration paths for the J-integral computation.

$$J = J_{\Gamma_1} + J_{\Gamma_2} + J_{\Gamma_3} + J_{\Gamma_4} = 0 \tag{5.4}$$

In the particular case of the notch depicted in Figure 5.3, paths Γ_2 and Γ_4 are located horizontally along free surfaces with respect to the crack tip's coordinate system, so the terms T_k and dy in Equation (5.1) are zero, therefore

$$J_{\Gamma_2} = J_{\Gamma_4} = 0 \tag{5.5}$$

As formally proved in [50, 95], the J-integral computed along an arbitrary small contour surrounding the crack tip is equal to the strain energy release rate $\mathcal{G}$, as long as the material is linear elastic and LEFM applies. However, an arbitrary small path around the crack tip (Γ_3 in Figure 5.3) would contain the crack tip singularity, so the J-integral computation along this path is not feasible. From Equations (5.4) and (5.5) it is deduced that the J-integral computed along paths Γ_1 and Γ_3 must yield the same value with opposite sign. Thus, for a notch like that depicted in Figure 5.3, $\mathcal{G}$ can be obtained by means of the J-integral approach by computing Equation (5.1) along a remote arbitrary path Γ_1.

The J-integral can also be decomposed into loading modes by using the formulation presented by Huber et al. [47] and later corrected by Rigby and Aliabadi [48]. The formulation presented next is its two-dimensional particularization.

Consider a symmetric integration path with respect to crack's plane as depicted in Figure 5.4, where points P and P' are placed on the symmetric paths Γ and Γ', respectively. The required field quantities for the J-integral evaluation u_k , σ_{ij} and ϵ_{ij} transformed into the crack front coordinate system should be decomposed in a sum of symmetric and antisymmetric parts regarding the crack front coordinate axes x, *i.e.*

$$u_k = u_k^I + u_k^{II} = \frac{1}{2}\begin{bmatrix} u_1^P + u_1^{P'} \\ u_2^P - u_2^{P'} \end{bmatrix} + \frac{1}{2}\begin{bmatrix} u_1^P - u_1^{P'} \\ u_2^P + u_2^{P'} \end{bmatrix} \tag{5.6}$$

$$\sigma_{ij} = \sigma_{ij}^I + \sigma_{ij}^{II} = \frac{1}{2}\begin{bmatrix} \sigma_{11}^P + \sigma_{11}^{P'} & \sigma_{12}^P - \sigma_{12}^{P'} \\ \sigma_{12}^P - \sigma_{12}^{P'} & \sigma_{22}^P + \sigma_{22}^{P'} \end{bmatrix} + \frac{1}{2}\begin{bmatrix} \sigma_{11}^P - \sigma_{11}^{P'} & \sigma_{12}^P + \sigma_{12}^{P'} \\ \sigma_{12}^P + \sigma_{12}^{P'} & \sigma_{22}^P - \sigma_{22}^{P'} \end{bmatrix} \tag{5.7}$$

$$\epsilon_{ij} = \epsilon_{ij}^{I} + \epsilon_{ij}^{II} = \frac{1}{2}\begin{bmatrix} \epsilon_{11}^{P} + \epsilon_{11}^{P'} & \epsilon_{12}^{P} - \epsilon_{12}^{P'} \\ \epsilon_{12}^{P} - \epsilon_{12}^{P'} & \epsilon_{22}^{P} + \epsilon_{22}^{P'} \end{bmatrix} + \frac{1}{2}\begin{bmatrix} \epsilon_{11}^{P} - \epsilon_{11}^{P'} & \epsilon_{12}^{P} + \epsilon_{12}^{P'} \\ \epsilon_{12}^{P} + \epsilon_{12}^{P'} & \epsilon_{22}^{P} - \epsilon_{22}^{P'} \end{bmatrix} \tag{5.8}$$

where the superscripts I and II denote respectively the symmetric and antisymmetric components and make reference to the crack opening modes I and II.

Then, the mode M J-integral along a path Γ can be computed as

$$J_{\Gamma}^{M} = \int_{\Gamma} \left[\left(\int_{0}^{\epsilon} \sigma_{ij}^{M} d\epsilon_{ij}^{M} \right) dy - T_{k}^{M} \frac{\partial u_{k}^{M}}{\partial x} ds \right] (M = I, II) \tag{5.9}$$

Finally, when LEFM applies, the strain energy release rates read

$$\begin{aligned} \mathcal{G}_{I} &= J_{\Gamma}^{I} \\ \mathcal{G}_{II} &= J_{\Gamma}^{II} \\ \mathcal{G} &= \mathcal{G}_{I} + \mathcal{G}_{II} \end{aligned} \tag{5.10}$$

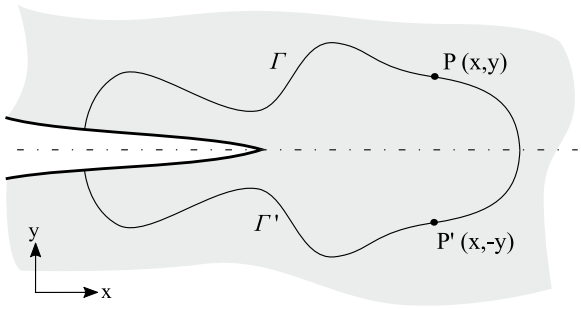

Figure 5.4: Symmetric integration paths for the mode-decomposed J-integral computation.

5.3 Methodology

5.3.1 Application of the J-integral approach in conjunction with cohesive elements

In quasi-brittle materials, a Fracture Process Zone (FPZ) is formed in the vicinity of the crack tip, so if a cohesive zone model is used to represent this inelasticity, the stress singularity is suppressed. In Figure 5.5 a cohesive zone is represented together with the integration paths for the J-integral computation. Paths Γ_{coh} and Γ_{ext} are equivalent to Γ_3 and Γ_1 from Figure 5.3, respectively, and Γ_{coh} is the combination of paths Γ_2 and Γ_4 from Figure 5.3. Thus, similarly to Equation (5.4),

$$J = J_{ext} + J_{coh} + J_{tip} = 0 \tag{5.11}$$

However, if no singularity on the crack tip exists as a consequence of the presence of a cohesive zone, the value of the J-integral along an arbitrary small path Γ_{tip} is zero, whilst the J-integral along the path Γ_{coh} is no longer zero because of the existence of cohesive tractions. Then, from Equation (5.11), the value of J_{coh} can be computed by evaluating the J-integral along a remote arbitrary path J_{ext}. If the mode-decomposed formulation is used (Equation (5.9)), the strain energy release rates $\mathcal{G}_I$ and $\mathcal{G}_{II}$ can be obtained from the remote elastic field. The global mixed-mode ratio B_{J-int} can be

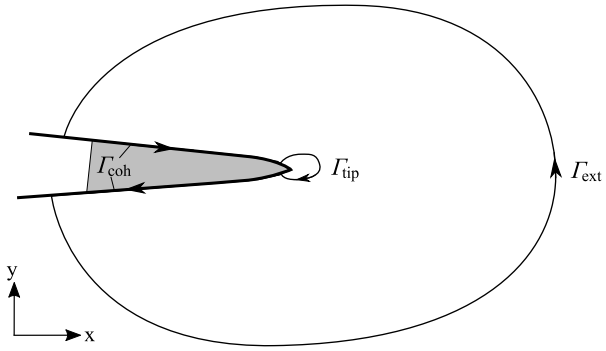

Figure 5.5: Integration paths involved in the computation of the J-integral in quasi-brittle materials.

then computed according to

$$B_{J-int} = \frac{\mathcal{G}_{II}}{\mathcal{G}_I + \mathcal{G}_{II}} = \frac{J_{ext}^{II}}{J_{ext}^{I} + J_{ext}^{II}} \tag{5.12}$$

Note the distinction made between the global mixed-mode ratio (B_{J-int}), computed by means of Equation (5.12), the applied mixed-mode ratio (B_{LEFM}), which is computed using LEFM closed-form solutions, and the local mixed-mode ratio (B_{coh}), which can vary within the cohesive zone as it is computed at integration point level. The definition of the local mixed-mode ratio depends on the formulation of the cohesive model, as summarized next for the cohesive formulations assessed.

5.3.2 Cohesive formulations assessed

The formulations assessed in this work are those implemented in the commercial finite element codes Abaqus v6.9-3 [15] and Ansys v11.0 [92] and the formulation proposed by Turon et al. [88]. Although new versions of the two finite element codes exist, no changes to the cohesive element formulations have been introduced. The main relevant features to this work of each cohesive formulation are presented next.

There are two different cohesive formulations available in Ansys: an exponential traction-separation law adapted from Xu and Needleman [83] and the linear law proposed by Alfano and Crisfield [86]. The Xu and Needleman traction-separation law implemented in Ansys is derived from a potential function and different fracture toughnesses cannot be specified for modes I and II. Given that in most composite materials the pure-mode fracture toughnesses are considerably different, this cohesive law is not suitable to be used with these kinds of materials. The Ansys formulation assessed in the current work is the adaptation from Alfano and Crisfield [86], where different power laws were proposed as propagation criterion. However, in the version implemented in Ansys only the following linear propagation criterion can be chosen:

$$\frac{\mathcal{G}_I}{\mathcal{G}_{Ic}} + \frac{\mathcal{G}_{II}}{\mathcal{G}_{IIc}} = 1 \tag{5.13}$$

where $\mathcal{G}$ is the SERR and $\mathcal{G}_{Ic}$ and $\mathcal{G}_{IIc}$ are the pure-mode fracture toughnesses. The mixed-mode ratio in Ansys is computed implicitly in the damage variable, from the instantaneous value of the nodal displacements.

On the other hand, the Abaqus cohesive zone formulation is an adaptation of the formulation presented by Camanho et al. [87] with a different local mixed-mode ratio evaluation, which is defined as the ratio between the accumulated mode-II and total dissipated energies at an integration point (the mixed-mode ratio depends on the loading history of the element). Two different propagation criteria can be chosen in Abaqus, the power law given by

$$\left(\frac{\mathcal{G}_I}{\mathcal{G}_{Ic}}\right)^{\alpha} + \left(\frac{\mathcal{G}_{II}}{\mathcal{G}_{IIc}}\right)^{\alpha} = 1 \tag{5.14}$$

or the Benzeggagh-Kenane criterion [96] given by

$$\mathcal{G}_c = \mathcal{G}_{Ic} + (\mathcal{G}_{IIc} - \mathcal{G}_{Ic})B^{\eta} \tag{5.15}$$

where α and η are mixed-mode material parameters to be obtained experimentally. The Benzeggagh and Kenane criterion was chosen in this work as it has been shown to be the most suitable criterion for mixed-mode fracture toughness computation for epoxy and PEEK composites [87].

Finally, in the formulation presented by Turon et al. [88] the mixed-mode ratio is defined instantaneously as a function of the nodal displacements as

$$B_{coh} = \frac{\mathcal{G}_{II}}{\mathcal{G}_I + \mathcal{G}_{II}} = \frac{\Delta_{sh}^2}{\langle \Delta_3 \rangle^2 + \Delta_{sh}^2} \tag{5.16}$$

where Δ_3 and Δ_{sh} are the mode I and II displacement jumps, respectively, and $\langle x \rangle$ is the Macauley operator defined as $\langle x \rangle = max(x, 0)$. The damage propagation criterion follows the Benzeggagh-Kenane law (Equation (5.15)).

Regarding thermodynamic consistency, Turon's et al. formulation was mathematically guaranteed in [71] to be thermodynamically consistent. By preventing the healing of the material when the local mixed-mode ratio changes, the additional constraint

$$\frac{k_{sh}}{k_3} = \frac{\mathcal{G}_{Ic}}{\mathcal{G}_{IIc}} \left(\frac{\tau_{sh}^0}{\tau_3^0} \right)^2 \tag{5.17}$$

was obtained. It relates interlaminar strengths (τ_3^0, τ_{sh}^0), pure-mode fracture toughnesses ($\mathcal{G}_{Ic}$, $\mathcal{G}_{IIc}$) and penalty stiffnesses (k_3, k_{sh}). These parameters are illustrated in Figure 5.2. The subscripts $(.)_3$ and $(.)_{sh}$ make reference to modes I and II, respectively. When the additional constraint given by Equation (5.17) is satisfied, the expected energy dissipation of the cohesive elements proposed by Turon et al. is obtained [71].

In the linear cohesive law formulation implemented in Ansys, the following constraint is explicitly imposed to guarantee thermodynamic consistency:

$$\frac{\Delta_3^0}{\Delta_3^f} = \frac{\Delta_{sh}^0}{\Delta_{sh}^f} \tag{5.18}$$

where Δ^0 and Δ^f are the damage initiation (d=0) and damage propagation (d=1) displacements jumps, respectively (see Figure 5.2). The subscripts $(.)_3$ and $(.)_{sh}$ refer to modes I and II, respectively.

Replacing and rearranging terms in Equation (5.18), the same condition than in Equation (5.17) is obtained. Therefore, thermodynamic consistency in Turon et al. [71] and Alfano and Crisfield [86] formulations is guaranteed by the same additional constraint. However, the fact that both formulations use the same additional constraint to guarantee thermodynamic consistency does not mean that this constraint would have the same effect on other cohesive formulations. The procedure presented in [71] to guarantee thermodynamic consistency is general enough to be applied to any cohesive formulation, but the conclusion reached might differ depending on the cohesive formulation.

5.3.3 Finite element model of a Mixed Mode Bending specimen

The simulations performed in the current work were done using the finite element model of the unidirectional, 2D Mixed Mode Bending (MMB) specimen [21, 22] described next and represented in Figure 5.6.

The applied mixed-mode ratio B_{LEFM} can be set to any value between pure modes I and II by adjusting the lever arm c. The value of c and the force-displacement curve can be obtained using the LEFM closed-form solutions from the ASTM Standard [19]. Two-dimensional plane strain elements were used: CPE4I in Abaqus [15] and PLANE182 in Ansys [92]. The interface was modeled using 4-node cohesive elements: COH2D4 for the Abaqus formulation [15], CONTA171 for Ansys formulation [92] and Turon's et al. cohesive elements implemented as Abaqus user elements [15, 88]. The element size for all the models is 0.1x0.1 mm^2 for the solid elements and 0.1 mm long for the zero-thickness cohesive elements. The mesh is fine enough according to [97], as the cohesive zone length for the most restrictive simulation is about 0.5 mm and there will always be at least 5 cohesive elements along the fully developed cohesive zone.

The specimen is 150 mm long and 20 mm wide. The initial crack length is 45 mm and the two arms of the cracked region are each 1.5 mm thick. The material and interface properties used are those given in Table 5.1, where E_{11} is the Young modulus in fiber direction, E_{22} and E_{33} are the Young moduli in longitudinal and through-the-thickness directions respectively, G_{ij} are the shear moduli, ν_{ij} are the Poisson ratios, τ_3^o and τ_{sh}^o are the interlaminar normal and shear strengths respectively, $\mathcal{G}_{Ic}$ and $\mathcal{G}_{IIc}$ are the fracture toughnesses and η is the Benzeggagh-Kenane mixed-mode parameter [96]. A penalty stiffness of $k = 10^6$ N/mm^3 is used [87].

With the use of the J-integral approach applied remotely to the crack tip, an exact modeling of the crack tip stress and strain fields is not necessary, *i.e.* relatively coarse meshes can be used, no special-purpose crack tip elements are needed and the method can be applied to arbitrary structured finite element meshes [93]. Thus, mesh size was chosen by taking into ac-

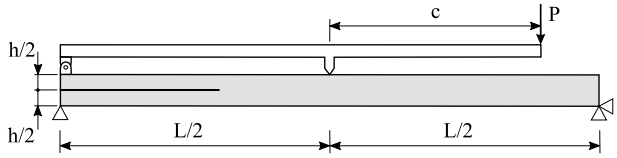

Figure 5.6: Geometry and boundary conditions of the Mixed Mode Bending (MMB) specimen.

E_{11}	$E_{22} = E_{33}$	$G_{12} = G_{13}$	G_{23}	$\nu_{12} = \nu_{13}$	ν_{23}
120.0 GPa	10.5 GPa	5.25 GPa	3.48 GPa	0.30	0.51
τ_3^o	τ_{sh}^o	$\mathcal{G}_{Ic}$	$\mathcal{G}_{IIc}$	η	
15, 30, 45 MPa	30, 50.6, 90 MPa	0.277 kJ/m^2	0.788 kJ/m^2	1.634	

Table 5.1: Material and interface properties.

count only that the number of elements along the cohesive zone is enough to represent the FPZ properly [97], for the most restrictive combination of interlaminar strengths used.

Integration paths selection for the J*-integral computation*

The J-integral can be obtained by computing numerically the integral given by Equation (5.9) along the appropriately selected integration paths, shown in Figure 5.7. Note that $J_{\Gamma_4} = J_{\Gamma_5} = 0$, as well as $\Gamma_6 \cap \Gamma_7$ and $\Gamma_1 \cap \Gamma_2 \cap \Gamma_3$ are equivalent to Γ_{coh} and Γ_{ext} in Figure 5.5, respectively. Then,

$$\mathcal{G} = J_{coh} = J_{\Gamma_1} + J_{\Gamma_2} + J_{\Gamma_3} \tag{5.19}$$

and similarly for the mode-decomposed J-integral.

Care must be taken when selecting the location of paths Γ_1, Γ_2 and Γ_3. Although the J-integral is path independent, these paths must avoid zones of stress concentration such as those points where boundary conditions are applied. Moreover, the path Γ_1 must be located in the left hand side of the boundary condition u_{II} (*i.e.* between the crack tip and u_{II}). Otherwise

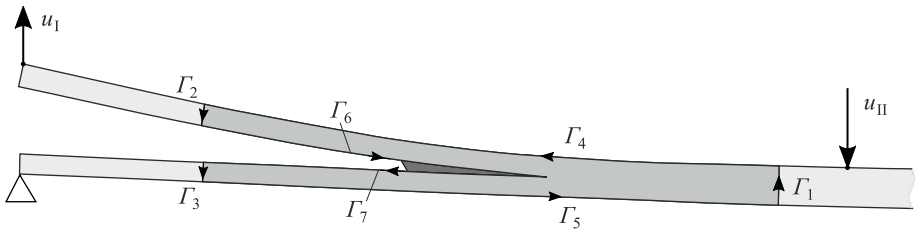

Figure 5.7: Selected J-integral integration paths in the MMB specimen.

the path Γ_4 would contain the boundary condition and J_{Γ_4} would not be zero any longer.

5.4 Finite element simulations results

The structural response (*i.e.* force-displacement curves) of an MMB specimen using three different cohesive formulations is presented in this section. Simulations with different τ_3^0/τ_{sh}^0 ratios were performed for each cohesive formulation. The energy dissipation when delamination grows and the mixed-mode ratio from a global point of view (B_{J-int}) are obtained by means of the J-integral post-processing tool introduced previously.

The force-displacement curves obtained using Abaqus cohesive elements are shown in Figure 5.8, followed by the evolution of the strain energy release rates for the case of $\tau_3^0 = \tau_{sh}^0 = 30$ MPa in Figure 5.9. A small simulation time increment was used to prevent convergence issues, so in Figure 5.9 only one out of every five available increments is depicted for clarity.

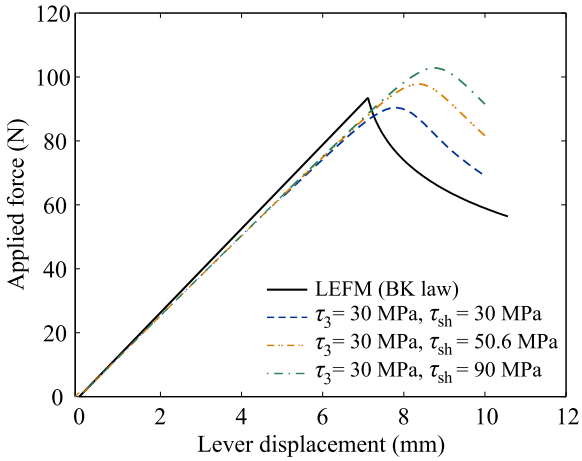

Figure 5.8: Influence of interlaminar strengths in the force-displacement response of an MMB specimen loaded with a mixed-mode ratio of $B_{LEFM} = 50\%$, using Abaqus cohesive elements COH2D4.

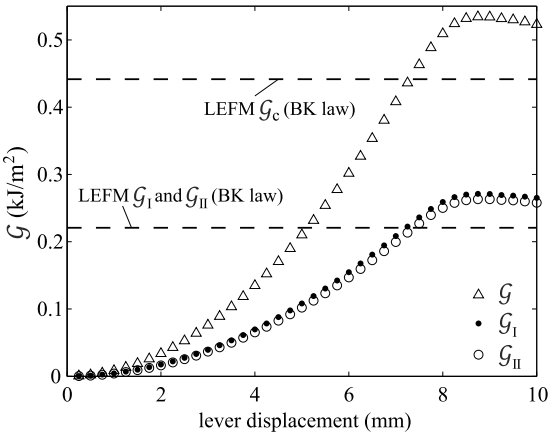

Figure 5.9: Evolution of mode-decomposed strain energy release rates computed by means of the J-integral approach for an MMB specimen with Abaqus cohesive elements COH2D4. $B_{LEFM} = 50\%$ and $\tau_3 = \tau_{sh} = 30$ MPa.

The force-displacement curves obtained using the Abaqus cohesive formulation do not match the analytical LEFM curve. Besides, a strong dependence of the results to the interlaminar strengths is observed. The strain energy release rates are overestimated, as can be seen in Figure 5.9. The $\mathcal{G}$-displacement curves for other τ_3^0/τ_{sh}^0 ratios simulated have been omitted, since they show an even higher overestimation of the strain energy release rates, as can be foreseen from the higher area under their respective force-displacement curves shown in Figure 5.8. Note also that during the whole simulation time $\mathcal{G}_I \approx \mathcal{G}_{II}$, which gives an average global mixed-mode ratio B_{J-int} of 48.63% with a standard deviation of 0.44%. Then, the global mixed-mode ratio (B_{J-int}) matches the applied one (B_{LEFM}), so the computation of the local mixed-mode ratio B_{coh} is not related to the global mixed-mode ratio. Therefore, the local mixed-mode ratio definition is not the cause of the incorrect energy dissipation. The reasons for the improper energy dissipation of this cohesive formulation will be discussed in the next section.

The force-displacement curves obtained using Ansys cohesive elements for different τ_3^0/τ_{sh}^0 ratios are presented in Figure 5.10. The numerical results are in close agreement with the analytical LEFM curve generated us-

ing the linear propagation criterion, regardless of the interlaminar strengths used. In Figure 5.10, the results are compared to the LEFM analytical solutions using both the linear and the Benzeggagh-Kenane (BK) interpolation laws. The inclusion of the BK law [96] in Figure 5.10 is appropriate for comparison with the other two formulations assessed, where the BK law is used.

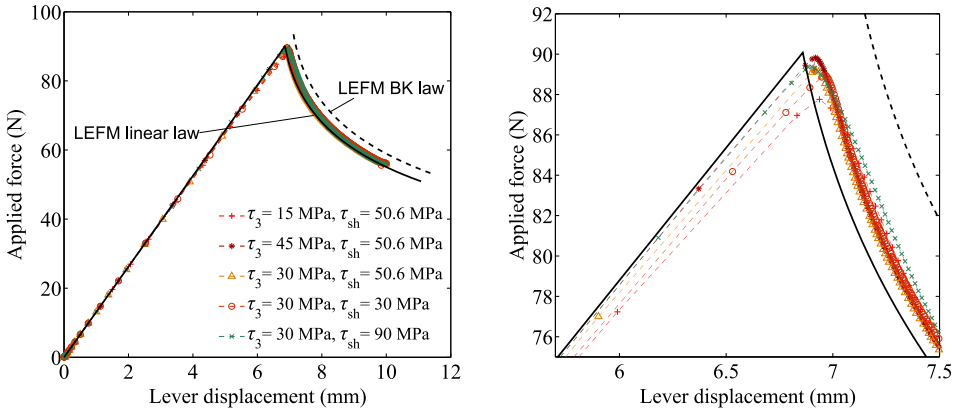

Figure 5.10: Influence of interlaminar strengths in the force-displacement response of an MMB specimen loaded with a mixed-mode ratio of $B_{LEFM} = 50\%$, using Ansys cohesive elements CONTA171. Global responses (left) and detail at peak force (right).

In Figure 5.11, the $\mathcal{G}$-displacement curve is presented for only one of the τ_3^0/τ_{sh}^0 ratios used, given that the response of all the cases simulated is practically identical. When self-similar crack growth occurs (*i.e.* when the value of $\mathcal{G}$ reaches $\mathcal{G}_c$), the simulation time increment is reduced drastically. For the sake of clarity, from this instant on only one out of every ten available increments has been depicted in Figure 5.11. The mixed-mode strain energy release rates are correctly computed by the Ansys cohesive formulation if compared to the mixed-mode fracture toughness given by a linear propagation criterion. The computed global mixed-mode ratio B_{J-int} has a mean value of 49.24% with a standard deviation of 0.26%, which is close to the applied mixed-mode ratio B_{LEFM}. Further discussion about the reasons for the results independence on interlaminar strengths is

given in the next section.

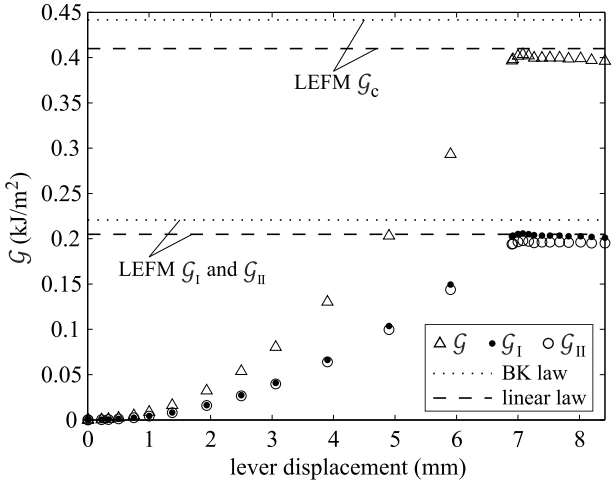

Figure 5.11: Evolution of mode-decomposed strain energy release rates computed by means of the J-integral approach for an MMB specimen with Ansys cohesive elements CONTA171. $B_{LEFM} = 50\%$, $\tau_3 = 30$ MPa and $\tau_{sh} = 50.6$ MPa.

Concerning Turon's et al. cohesive zone formulation [88], it was enhanced in [71] to properly account for mixed-mode energy dissipation. That work showed that, when Equation (5.17) is satisfied, the formulation properly accounts for mixed-mode energy dissipation and yields accurate numerical results. However, the mixed-mode ratio at an integration point level was observed to change during simulation time and it remained unclear if the original model properly estimated the mixed-mode ratio and if this was the underlying reason for improper energy dissipation. Figure 5.12 illustrates this variation within the cohesive zone. The value of the local mixed-mode ratio B_{coh} and the damage variable d are depicted at an arbitrary instant during self-similar crack growth. Once the crack begins to grow in a self-similar way, the curves shown in Figure 5.12 keep their shapes and move along the x coordinate. Further discussion about the consistence of the local mixed mode variation is given in next section.

In the current work, several τ_3^0/τ_{sh}^0 were simulated to confirm what was observed by Turon et al. in [71] and to reveal whether the mixed-mode ratio

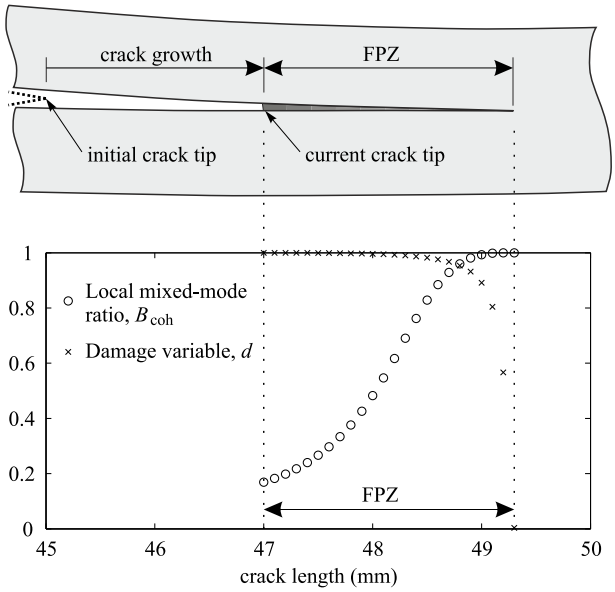

Figure 5.12: Local mixed-mode ratio and damage variable evolution along the fracture process zone during self-similar crack growth for an MMB specimen loaded with a global mixed-mode ratio of $B_{LEFM} = 50\%$.

obtained using the J-integral approach agrees with the LEFM solution. The force-displacement curves presented in Figure 5.13 are similar to those presented by Turon et al. in [71]. It can be observed that the results do not match the analytical LEFM solution unless the interlaminar strengths are selected according to Equation (5.17). Since the same penalty stiffnesses are used for modes I and II, the only combination of τ_3^0 and τ_{sh}^0 of those simulated that satisfy Equation (5.17) is $\tau_3^0 = 30$ MPa and $\tau_{sh}^0 = 50.6$ MPa. It can be observed that the simulations using these values match the LEFM curves, regardless of the mixed-mode ratio B_{LEFM} applied. In Figure 5.13 only the results for two different applied mixed-mode ratios are shown for clarity. However, simulations were performed for many different applied mixed-mode ratios ranging from 0.2 to 0.7 and similar results were obtained.

In Figure 5.14, the evolution of the $\mathcal{G}$-displacement curves of four of the

cases depicted in Figure 5.13 are presented. Subfigures (a) and (b) contain the results of two unadjusted interlaminar strengths cases, where an under and overestimation of strain energy release rates is observed, respectively. On the other hand, subfigures (c) and (d) present the results of adjusted interlaminar strengths cases with two different applied mixed-mode ratios. The strain energy release rates obtained in these cases are in close agreement with LEFM predictions.

It can be extracted from Figure 5.14 that the global mixed-mode ratio B_{J-int} has a mean value of 50.00% with a standard deviation of 0.30% when

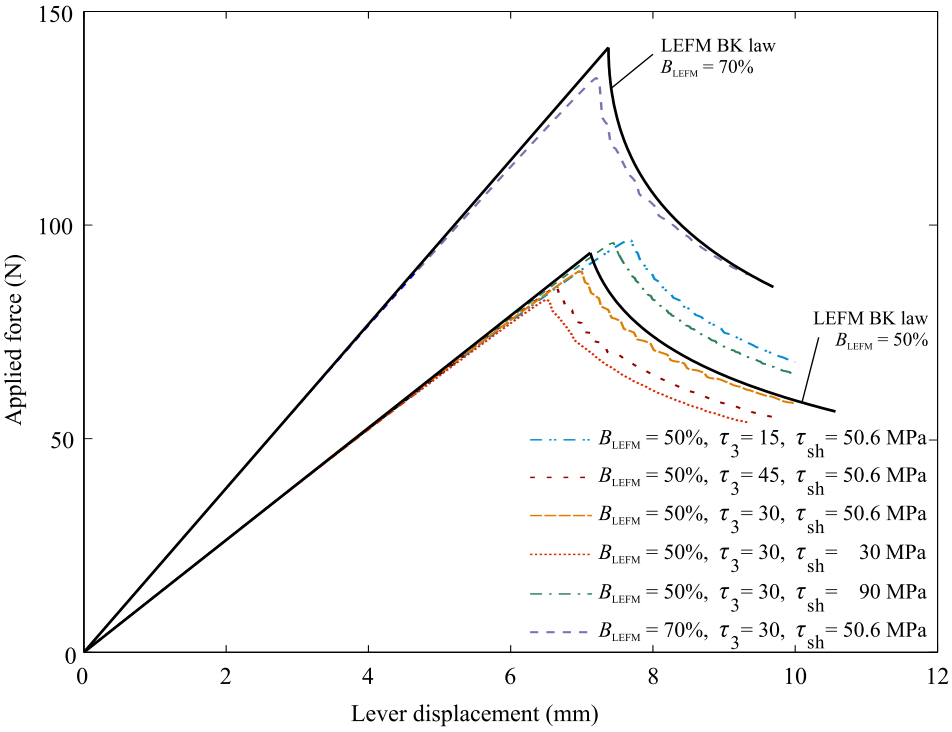

Figure 5.13: Influence of interlaminar strengths in the force-displacement response of an MMB specimen loaded with mixed-mode ratios of $B_{LEFM} = 50\%$ and $B_{LEFM} = 70\%$, using Turon's cohesive elements with different τ_3^0/τ_{sh}^0 ratios.

$B_{LEFM} = 50\%$ is applied, and a mean value of 70.18% with a standard deviation of 0.37% when $B_{LEFM} = 70\%$. Therefore, the computed global mixed-mode ratio, B_{J-int}, and the applied mixed-mode ratio, B_{LEFM}, are similar during the whole simulation time, whatever the τ_3^0/τ_{sh}^0 ratio is.

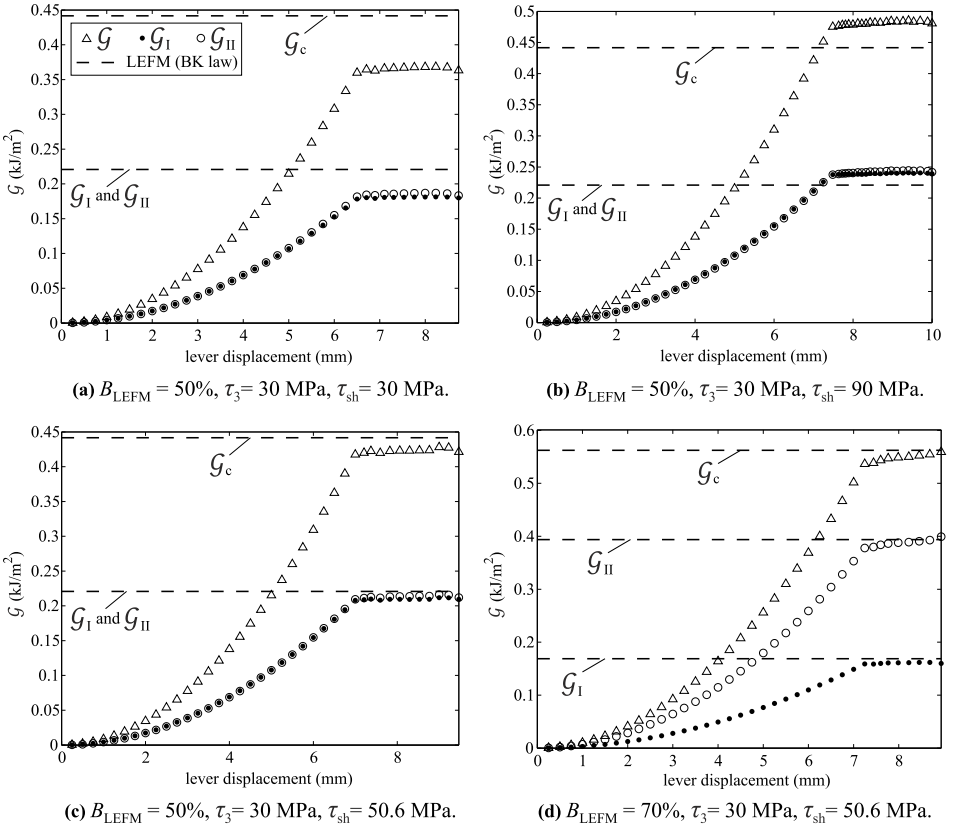

(a) $B_{\text{LEFM}} = 50\%$, $\tau_3 = 30$ MPa, $\tau_{\text{sh}} = 30$ MPa.

(b) $B_{\text{LEFM}} = 50\%$, $\tau_3 = 30$ MPa, $\tau_{\text{sh}} = 90$ MPa.

(c) $B_{\text{LEFM}} = 50\%$, $\tau_3 = 30$ MPa, $\tau_{\text{sh}} = 50.6$ MPa.

(d) $B_{\text{LEFM}} = 70\%$, $\tau_3 = 30$ MPa, $\tau_{\text{sh}} = 50.6$ MPa.

Figure 5.14: Evolution of mode-decomposed strain energy release rates computed by means of the J-integral approach for MMB specimens with Turon's cohesive elements.

5.5 Discussion

The cohesive formulation implemented in Abaqus does not provide accurate results under mixed-mode loading. Non-negative energy dissipation is not explicitly guaranteed when the damage variable and the mixed-mode ratio at an integration point change simultaneously, so conceptually there could be healing of the material as a consequence of particular local mixed-mode variations.

The results obtained using Ansys' linear cohesive law are in agreement with LEFM predictions. The thermodynamic consistency of the model, which was discussed in a previous section and guaranteed by Equation (5.18), makes the results insensitive to the local mixed-mode variation and so the energy is dissipated as expected. It has to be taken into account that the results are in agreement with LEFM predictions if compared to a mixed-mode fracture toughness given by a linear propagation criterion but, as investigated in [87], the BK law is more appropriate when dealing with epoxy and PEEK composites.

The formulation proposed by Turon et al. was shown to provide accurate numerical results in [71], as long as the interlaminar strengths used are adjusted according to Equation (5.17). However, it was unclear if the reason for the improper energy dissipation was the variation of the local mixed-mode ratio. In this work it has been shown that the computed global mixed-mode ratio (B_{J-int}) and the applied mixed-mode ratio (B_{LEFM}) are similar during the whole simulation time regardless of the interlaminar strengths chosen. Therefore, not only is the mixed-mode ratio being correctly captured, but also its computation is not the reason for the incorrect energy dissipation when non-adjusted interlaminar strengths are used.

For the cohesive element formulations evaluated in this study, those that are thermodynamically consistent have been shown to be insensitive to the local variation of the mixed-mode ratio. All the simulations performed in this work are such that the cohesive zone length is small in comparison with the relevant dimensions of the structure. It is worth noting that the results presented here cannot be directly extrapolated to larger fracture process zones, for which further research is still needed.

Regarding the variation of the local mixed-mode ratio B_{coh} along the

FPZ observed by Turon et al. [71] and illustrated in Figure 5.12, it is consistent with what has been presented and discussed in this paper. It stems from its definition based on nodal displacements (Equation (5.16)). One might consider the non-damaged part of the MMB specimen as a beam of thickness h (see Figure 5.6) under bending. According to beam's theory, the through-the-thickness stresses of such a beam (responsible of mode I opening) would be negligible and the shear stresses would be maximum, which yields a pure mode II on the less damaged zone of the FPZ, as observed. On the other hand, the boundary conditions applied to the MMB specimen make the curvature of the upper arm higher than the lower one. At the non-damaged region of the specimen, the difference between curvatures does not exist since the two arms are together, but at the most damaged point of the FPZ, the curvatures of the two arms are different enough to give a high mode I separation. Because of this difference in arm curvatures, mode I becomes progressively dominant as the distance to the beginning of the FPZ increases, giving the curve of B_{coh} depicted in Figure 5.12.

5.6 Concluding remarks

The mode-decomposed J-integral approach implemented as a finite element post-processing tool was used to obtain the strain energy release rates from the elastic field remote to the crack tip and, thus, to compute the mixed-mode ratio from a global point of view.

Different cohesive zone formulations were assessed under mixed-mode conditions in terms of dissipated energy and mixed-mode ratio estimation. The results obtained showed that for all the cohesive zone formulations assessed the mixed-mode ratio is properly computed, so it is not related to the incorrect energy dissipation observed. It was shown that the variation of the local mixed-mode ratio along the fracture process zone observed in [71] is consistent with beam's theory and with the constant global mixed-mode ratio.

Regarding the accuracy of each formulation, it was observed that one of the formulations implemented in Ansys [86, 92] and the one proposed by Turon et al. [88] provide accurate numerical results, dissipate the energy

correctly and estimate properly the mixed-mode ratio. The main difference between these two formulations is that in Ansys a linear propagation criterion for mixed mode is used, whilst in the formulation proposed by Turon et al. the BK law is implemented. The BK propagation criterion is more appropriate when modeling epoxy and PEEK composites [87]. The formulation implemented in Abaqus does not yield accurate numerical results, since the dissipated energy is not correctly computed. This fact was shown to be unrelated to the mixed-mode ratio estimation. The difference between the Abaqus formulation and the other two formulations assessed is that non-negative energy dissipation is not explicitly guaranteed when the damage variable changes at the same time as the local mixed-mode ratio, which causes the model to create a fictitious energy generation and yield inaccurate numerical results.

Chapter 6

Finite-thickness cohesive elements for modeling thick adhesives

Abstract. A new cohesive element formulation is proposed for modeling the initial elastic response, softening, and failure of finite-thickness adhesives. By decoupling the penalty stiffness of the cohesive zone model formulation and the physical adhesive modulus, the new formulation ensures proper dissipation of fracture energy for opening and shear loading modes and mixed-mode loading conditions with any combination of elastic and fracture material properties. Predictions are made using the new element formulation for double cantilever beam, end-notched flexure, mixed-mode bending and single lap joint specimens with varying adhesive thicknesses. Good correlation between all predictions and experimental results was observed.

6.1 Introduction

The need to produce lightweight composite structures has also increased the use of adhesive joints in their assembly. Compared to mechanically fastened joints, adhesive joints lower stress concentration areas, provide better strength-to-weight ratios and, at the same time, reduce the manufacturing processes required, resulting in cost savings [1]. In the framework of finite element analyses, cohesive elements excel at modeling damage evolution within predefined adhesive interfaces. Unlike analysis methods based on linear elastic fracture mechanics (LEFM), cohesive zone models are able to accurately reproduce the fracture process zone (FPZ) that develops ahead of a crack tip and, therefore, accurately simulate the load redistribution due to damage and the fracture behavior of adhesive joints.

Cohesive elements are governed by a traction-separation law that can

take different shapes. The simplest pure-mode traction-separation law is the linear softening law shown in Figure 6.1, which is defined by two physical material parameters, the strength and the fracture toughness, and one numerical parameter, the penalty stiffness. The interface strength sets the stress level at which the cohesive element will begin to soften, whereas the fracture toughness is the energy dissipated during the fracture process. The penalty stiffness, which sets the stiffness of the undamaged element, must be defined to implement the cohesive law in a finite element framework. In order to tie rigidly together the nodes across an undamaged interface and to prevent interpenetration, the penalty stiffness is set as a very high numerical parameter.

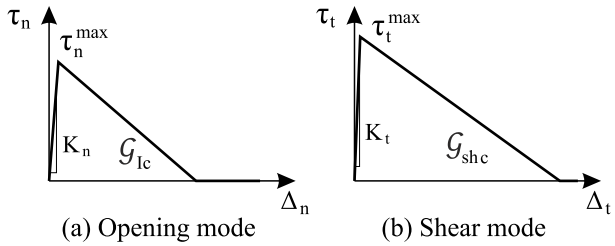

Figure 6.1: Parameters to define a) mode I (opening) and b) shear mode linear softening cohesive laws.

Under mixed-mode loading conditions, the strength, the fracture toughness, and the penalty stiffness must be defined for the opening and the shear modes, together with a mixed-mode interpolation criterion. Although several cohesive element formulations are available in the literature [81, 82, 86–88, 90], few have been thoroughly validated under changing mixed-mode conditions. The mixed-mode ratio is known to change throughout the FPZ even in those situations where LEFM applies and predicts a constant mode ratio [13, 71], such as the delamination analysis of a mixed-mode bending (MMB) specimen [21, 22]. Turon et al. [71] showed that the use of the existing cohesive element formulations did not result in accurate predictions under mixed-mode loading and proposed a methodology to correct this behavior. Turon et al. [71] observed that, under changing mixed-mode conditions, the pure-mode strengths, fracture toughnesses and penalty stiffnesses cannot be independently defined, and that they need to fulfill a constraint

to ensure proper energy dissipation. For the particular cohesive element formulation proposed by Turon et al. [88], this constraint takes the form

$$K_n = K_t \frac{\mathcal{G}_{sh_c}}{\mathcal{G}_{Ic}} \left(\frac{\tau_n^{max}}{\tau_t^{max}} \right)^2 \tag{6.1}$$

where $\mathcal{G}_{Ic}$ and $\mathcal{G}_{sh_c}$ are the opening and shear fracture toughness, τ_n^{max} and τ_t^{max} are the opening and shear interlaminar strengths and K_n and K_t are the opening and shear penalty stiffnesses, respectively.

Because the strength and the fracture toughness are physical properties and the penalty stiffness is a numerical parameter, one of the pure-mode penalty stiffnesses can be adjusted to fulfill the constraint given by Equation (6.1) and guarantee the proper energy dissipation without changing any physically measured material properties. Following that strategy, Turon et al. [98] recently proposed a new cohesive formulation that internally adjusts the penalty stiffness so that Turon's constraint is fulfilled and, at the same time, physically measured properties can be used.

However, in the simulation of adhesively bonded joints, the adhesive layer has a finite thickness that in many occasions cannot be neglected. Finite-thickness cohesive elements can be used to simulate adhesive joints by setting the initial stiffness equal to the actual stiffness of the adhesive. Thus, when using finite-thickness cohesive elements, the initial stiffness is no longer a numerical parameter, but a material property and, therefore, there is no numerical parameter that can be freely adjusted to satisfy Turon's constraint. In fact, this constraint may conflict with some experimental observations if applied to the simulation of finite-thickness adhesive layers. For instance, if the Poisson's ratio of an adhesive is $\nu = 0.5$, then

$$K_n = 2(1+\nu)K_t = 3K_t \tag{6.2}$$

If the material fails according to the von Mises criterion, then

$$(\tau_n^{max})^2 = 3(\tau_t^{max})^2 \tag{6.3}$$

Therefore, under these assumptions Equation (6.1) imposes $\mathcal{G}_{Ic} = \mathcal{G}_{sh_c}$, which is usually incorrect [32].

In the present work, a new approach is proposed to fulfill Turon's constraint while using the actual physical properties of the adhesive. The

physical elastic moduli of the adhesive and the interface penalty stiffnesses are decoupled, so that the finite-thickness cohesive element is the result of a zero-thickness cohesive interface embedded within a linear elastic bulk material. The total deformation of the element is the sum of the linear elastic deformation of the bulk and the deformation of the interface due to damage. Turon's constraint can be fulfilled by internally adjusting one of the interface penalty stiffnesses.

6.2 Finite-thickness cohesive element formulation

A finite-thickness cohesive model based on the formulation proposed by Turon et al. [98] is presented in this section. In Section 6.3.1, the formulation is validated by simulating pure-mode and mixed-mode standard fracture toughness tests and comparing their results to LEFM predictions and experimental data available in the literature. The limitations of the formulation in terms of the cohesive element thickness are then discussed. Finally, in Section 6.3.2, single lap joint (SLJ) tests with different adhesive thicknesses are simulated and the numerical results are compared against experimental data. The proposed formulation is shown to yield accurate results for both the standard fracture toughness tests, where the adhesive thickness has little effect on the response, and for the SLJ test, where the adhesive thickness has an appreciable effect on the failure load.

6.2.1 Stiffness decoupling and numerical implementation

The finite-thickness cohesive element proposed herein can be described as a zero-thickness cohesive interface embedded within a linear elastic bulk material. The total displacement of the element is decomposed into the linear elastic deformation of the bulk and the displacement jump of the cohesive interface, as illustrated in Figure 6.2.

Stress equivalence is assumed across the cohesive interface, i.e. the total traction of the interface τ is defined either as

$$\tau = K^{(int)}(1-d)\Delta^{(int)} \tag{6.4}$$

or

$$\tau = K\Delta^{(bulk)} \tag{6.5}$$

where d is the interface damage variable, which degrades the interface penalty stiffness $K^{(int)}$, K is the bulk adhesive stiffness and $\Delta^{(int)}$ and $\Delta^{(bulk)}$ are the interface and bulk adhesive displacement jump vectors, respectively. $\Delta^{(bulk)}$ is computed as

$$\Delta^{(bulk)} = \Delta - \Delta^{(int)} \tag{6.6}$$

for each component depicted in Figure 6.2. Combining Equations (6.4-6.6), the relationship between the element displacement jump vector (Δ) and the interface displacement jump vector ($\Delta^{(int)}$) can be obtained for the opening and shear loading modes as

$$\Delta_n^{(int)} = \Delta_n \frac{K_n}{K_n + K_n^{(int)} \left(1 - d\frac{\langle \Delta_n \rangle}{\Delta_n}\right)} \tag{6.7}$$

$$\Delta_t^{(int)} = \Delta_t \frac{K_t}{K_t + K_t^{(int)} (1 - d)} \tag{6.8}$$

where $\Delta_n^{(int)}$ and $\Delta_t^{(int)}$ are the opening and shear components of the interface displacement jump vector, respectively, Δ_n and Δ_t are the opening and shear components of the element displacement jump vector, respectively, K_n and K_t are the adhesive opening and shear stiffnesses, respectively, $K_n^{(int)}$ and $K_t^{(int)}$ are the interface opening and shear penalty stiffnesses, respectively, and d is the interface damage variable. $\langle x \rangle$ is the Macauley operator, which takes the value of x if $x \geq 0$ and 0 otherwise. The Macauley

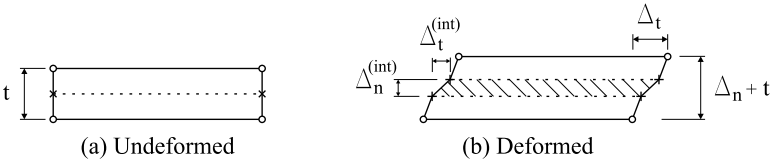

Figure 6.2: Schematic representation of the decoupling between the bulk adhesive and the embedded interface in an a) undeformed and b) deformed state.

operator is used to restore the original interface stiffness in case of interpenetration. The adhesive stiffnesses are computed as

$$K_n = \frac{E_{adh}}{t} \tag{6.9}$$

$$K_t = \frac{G_{adh}}{t} \tag{6.10}$$

where E_{adh} and G_{adh} are the adhesive Young's and shear moduli, respectively, and t is the adhesive thickness. Because the stiffnesses of the interface are decoupled from those of the bulk material, the interface stiffnesses are numerical parameters whose purpose is to ensure that the interface behaves as though rigidly tied together prior to damage. The interface opening stiffness is set arbitrarily high and the interface shear stiffness is computed so as to fulfill Turon's constraint given by Equation (6.1).

The user must only provide the physical material properties, whereas the numerical parameters (i.e. the penalty stiffness) are internally set to fulfill Equation (6.1) and therefore ensure proper energy dissipation [71]. Additionally, the penalty stiffness is removed from the stiffness matrix, which has a positive and remarkable impact on the minimum stable time increment calculation on explicit analyses [15, 99] and on the convergence of the numerical solution algorithms in implicit analyses [97, 100].

The interface damage variable is a function of the interface displacement jumps and is calculated using the cohesive element formulation of Turon et al. [98]. Because the interface displacement jumps are also a function of the current damage variable, as shown in Equations (6.7) and (6.8), the iterative loop depicted in Figure 6.3 is required to reach equilibrium. One pass of this loop involves calculating the interface displacement jump with the previous damage variable and updating the damage variable using the new interface displacement jump. Equilibrium is reached when the change in interface displacement jump is less than a given tolerance. Convergence is ensured using this procedure. The interface displacement jump increases monotonically with the damage variable ($\partial\Delta^{(int)}/\partial d > 0$). Because the damage variable also increases monotonically from 0 to 1, the solution is found when either the damage variable ceases to increase or when the damage variable reaches 1.

The proposed cohesive formulation has been implemented both as an Abaqus [15] user element (UEL) and user material (UMAT) subroutines.

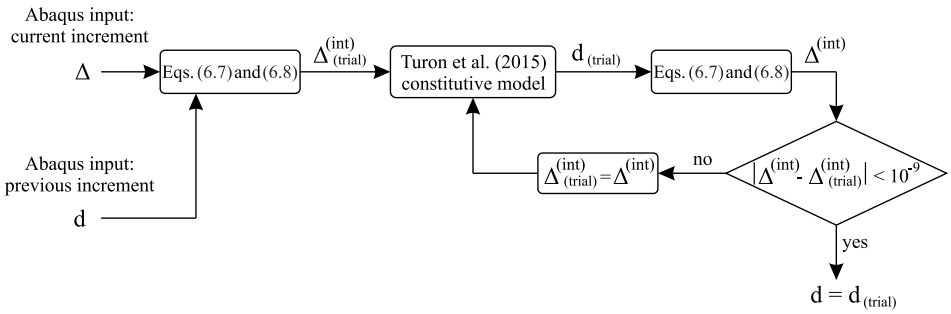

Figure 6.3: Iterative procedure for the computation of the interface displacement jumps.

6.2.2 Computational limitation of the adhesive thickness

The stress equivalence assumption given by Equations (6.4) and (6.5) results in a single through-the-thickness stress state for the cohesive element. The elastic energy stored in the bulk adhesive cannot be transferred to the neighboring elements and can only be released through the fracture of the element. If the elastic energy stored in the element is larger than the fracture energy, the element traction-separation response will exhibit a snapback behavior [101]. Because the proposed cohesive element is intended to simulate thick adhesive interfaces with a single cohesive element along the adhesive layer thickness and, therefore, the mesh is not refined along thickness direction, the element will exhibit a snapback behavior for thicknesses greater than [101]

$$t_{max} = \frac{2\mathcal{G}_c E_{adh}}{\left(\tau^{max}\right)^2} \tag{6.11}$$

The maximum adhesive thickness t_{max} should be checked for the two limiting cases given by the mode I and the mode II interface properties.

The snapback behavior implies that the damage state of the element suddenly changes from undamaged to totally damaged when the strength

of the element is reached. The fact that no partially damaged elements can exist means that the length of the numerical FPZ is essentially zero for $t \geq t_{max}$.

It is generally accepted [97] that at least three to five cohesive elements must be within the numerical FPZ length to accurately reproduce the interface behavior. In such cases where the element thickness is above t_{max} and the numerical FPZ length becomes zero, there is no mesh refinement along the length of the layer of cohesive elements that can achieve the previous condition and, therefore, the results might be inaccurate. In practice, Bažant and Oh [101] recommend the element thickness be below $t_{max}/2$ for the crack band model. Given the similarity of the model proposed in the current work to the Bažant and Oh [101] crack band model, the same threshold can be taken as a reference.

If very thick adhesives are to be modeled or coarse meshes need to be used, a possible solution to overcome the thickness limitation issue would be lowering the interlaminar strength τ^{max} [97], which would enlarge the FPZ and allow for a higher thickness limit t_{max}. However, it must be kept in mind that this solution would also involve spuriously adjusting a measurable material property and would require a set of simulations for finding a proper adjustment for each particular case study.

6.3 Finite element models and numerical results

6.3.1 Fracture mechanics tests

Numerical simulations of double cantilever beam (DCB), end-notched flexure (ENF) and mixed-mode bending (MMB) tests with different adhesive thickness have been conducted using the finite-thickness cohesive formulation proposed in this work. The geometry and properties of the simulated specimens were taken from the experimental study performed by Girolamo et al. [32, 102], as well as the experimental results for comparison purposes. The specimens were 200 mm long and 25 mm wide. The two 2.5-mm-thick, carbon/epoxy adherends were co-bonded by means of a 0.254-mm-thick FM-300M adhesive layer with a pre-crack of 55 mm. The material and interface properties are detailed in Table 6.1. The interface properties are directly obtained from the experimental characterization in [32]. The shear

penalty stiffness $K_t^{(int)}$ was set sufficiently high to ensure that both $K_t^{(int)}$ and $K_n^{(int)}$ are above 10^6 N/mm^3 after fulfilling the constraint given by Equation (6.1).

The specimens were modeled using the two-dimensional, plane strain CPE4I Abaqus elements for the adherends and the COH2D4 Abaqus cohesive elements for the interface. The proposed cohesive element formulation was applied via a custom UMAT material subroutine. Regarding the mesh refinement, 0.1-mm-long cohesive elements were used to ensure that more than five elements are within the numerical FPZ [97]. The thickness of the cohesive elements was that of the adhesive layer.

A comparison between the LEFM closed-form solution, the experimental results and the modeled behavior of the ENF specimens is shown in Figure 6.4 (a). The results of the ENF tests show an underestimation of the peak load with respect to the LEFM closed-form solution. However, the numerical results are in close agreement to the experimental data in [32] in terms of peak load. The FPZ was reported in [32] to be remarkably long in the ENF tests, which implies that LEFM assumptions do not hold and, therefore, LEFM results overestimate the peak load. The predicted peak load results provided by the proposed finite-thickness cohesive formulation for the ENF specimen are within 5% of the average experimental values regardless of the fracture process zone size. The predicted peak loads occur at lower displacements for the ENF specimens with thicker adhesive layers because of the increased bending stiffness of the thicker adhesive layer. The initial compliance of the specimen is also accurately captured by the

E_{11}	142.0 GPa	$\mathcal{G}_{Ic}$	1.25 kJ/m^2	E_{adh}	2921 MPa
$E_{22} = E_{33}$	7.8 GPa	$\mathcal{G}_{sh_c}$	7.9 kJ/m^2	G_{adh}	1016 MPa
$G_{12} = G_{13}$	4.0 GPa	τ_n^{max}	89.0 MPa		
G_{23}	2.8 GPa	τ_t^{max}	47.5 MPa		
$\nu_{12} = \nu_{13}$	0.34	η	2.6		
ν_{23}	0.40	$K_t^{(int)}$	10^6 N/mm^3		

Table 6.1: Properties of the carbon/epoxy adherends and the 0.254-mm-thick FM-300M adhesive [32].

numerical model, as the experimentally measured adhesive stiffness is used in the simulations.

The cohesive model results for the DCB and the MMB 70% cases shown in Figures 6.4 (b) and (c), respectively, are also shown to be in very good agreement with LEFM predictions. The simulations of the DCB specimen were repeated with a different modeling technique. Instead of the finite-thickness cohesive elements, the adhesive layer was modeled using a stack of three elements: two solid elements for the linear elastic behavior of the

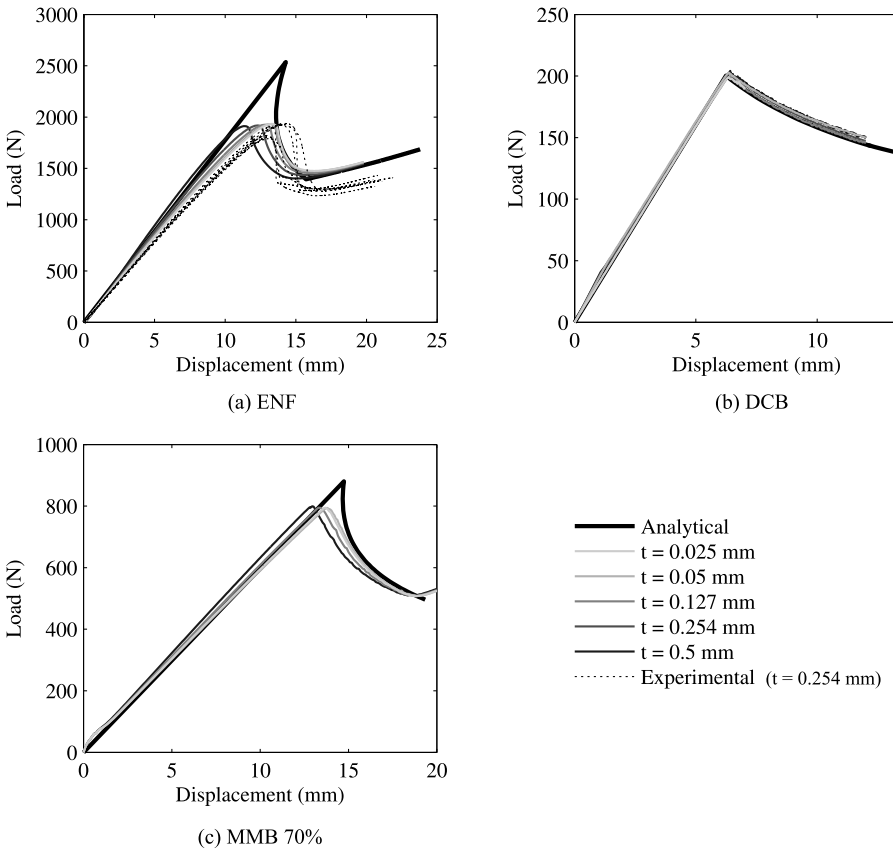

Figure 6.4: Load-displacement response of the a) ENF, b) DCB, and c) MMB 70% tests with different adhesive thickness.

adhesive and a zero-thickness cohesive element [98] between them, as shown in Figure 6.5. The results were compared in terms of fracture process zone length to those obtained with the finite-thickness cohesive elements. In Figure 6.6, the normalized FPZ length with respect to the zero-thickness adhesive layer FPZ length is plotted against the normalized adhesive thickness with respect to the limit given by Equation (6.11).

The FPZ length of the finite-thickness cohesive element progressively decreases as the adhesive thickness grows, until t_{max} is reached. The FPZ length is zero thereafter, as expected. For the interface modeled using solid elements and zero-thickness cohesive elements, the thickness limitation is not observed. The differences observed in the FPZ lengths recovered using the two modeling techniques are in agreement with the recommendation given by Bažant and Oh [101] of using element thicknesses below $t_{max}/2$. As can be observed from Figure 6.6, the difference in the numerical FPZ lengths for the DCB modeled using the two techniques is relatively low for adhesive thicknesses below $t_{max}/2$. All the simulations of the DCB, ENF, and MMB tests presented in Figure 6.4 were performed for a ratio t/t_{max} below 0.5.

6.3.2 Adhesive thickness effect on a single lap joint test

The effect that the bondline thickness has on the structural response of a single lap joint is studied using the proposed finite-thickness cohesive element. The experimental tests in [103] were simulated and the numerical

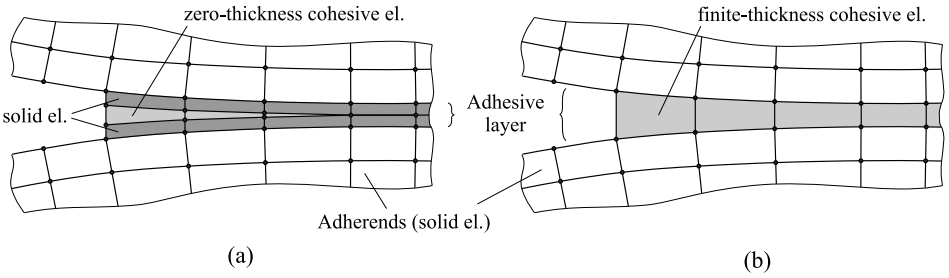

Figure 6.5: Adhesive layer modeled by means of (a) two solid elements and a zero-thickness cohesive element or (b) a single finite-thickness cohesive element.

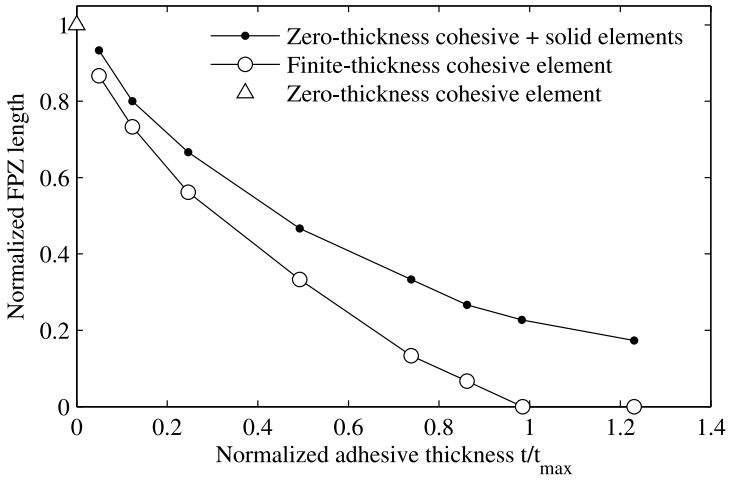

Figure 6.6: FPZ length as a function of the adhesive thickness for the DCB test.

and experimental results were compared.

The SLJ specimens were composed of two steel adherends joined with a Hysol EA9321 adhesive layer. The overlap length was 25 mm and specimens with adhesive layer thicknesses varying from 0.2 mm to 1.0 mm were tested. Each adherend was 95 mm long, 25 mm wide and 2 mm thick. The Young's modulus of the steel adherends was assumed to be 210 GPa and their Poisson's ratio 0.3. The interface properties presented in Table 6.2 were directly taken from the experimental characterization in [103]. The interlaminar shear strength reported in [103] depends on the adhesive thickness, so the value shown in Table 6.2 is the result of the linear extrapolation of the failure load to a zero adhesive thickness. The Benzeggagh-Kenane mixed-mode interpolation parameter η was not reported in [103], so two extreme values of η were assumed in the simulations.

Regarding the finite element models, the two-dimensional, plane strain CPE4I Abaqus element was used for the adherends and the proposed finite-thickness cohesive element was used for the adhesive. Cohesive elements with a length of 0.1 mm were used to ensure that more than five elements are within the numerical FPZ [97]. The thickness of the cohesive elements

E_{adh} (MPa)	G_{adh} (MPa)	$\mathcal{G}_{Ic}$ (kJ/m^2)	$\mathcal{G}_{sh_c}$ (kJ/m^2)	τ_n^{max} (MPa)	τ_t^{max} (MPa)	η (-)	$K_t^{(int)}$ (N/mm^3)
3870	1423	0.45	0.90	45.97	18.7	1.5 - 5.0	10^6

Table 6.2: Properties of the Hysol EA9321 adhesive (taken directly from [103] unless stated in the text).

was that of the adhesive layer.

Both the experimental and the numerically predicted failure loads of the SLJ specimens are shown in Figure 6.7 as a function of the bondline thickness. The numerical results are in good agreement with the observed experimental behavior for both values of the mixed-mode interpolation parameter η. The numerical results using the actual value of η would fall within the results of the two extreme η assumed.

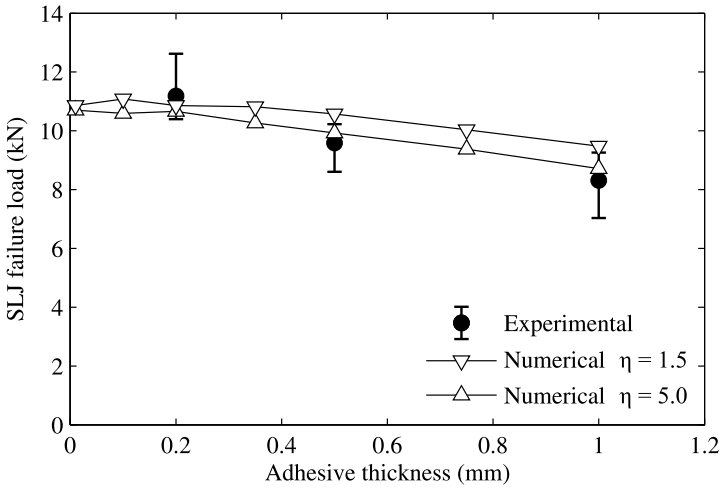

Figure 6.7: Experimental and numerical variation of the failure load of the SLJ specimen as a function of the adhesive thickness.

6.4 Conclusions

A new formulation for cohesive elements has been proposed that allows for a more accurate representation of the initial elastic response, softening and ultimate failure of adhesive materials with a finite thickness in a finite element model. The need for these modifications arose from Turon's observation that there exists a necessary constraint between the penalty stiffness, strength and fracture toughness material properties of cohesive elements in order for fracture energy to be dissipated correctly [71]. To address this issue, the cohesive penalty stiffness and the physical adhesive stiffness were decoupled. The thick adhesive is modeled as containing an embedded zero-thickness cohesive plane and stress equivalence is assumed between the bulk of the adhesive and across cohesive fracture plane. Good correlation was observed between model predictions and experimental data for DCB, ENF, MMB and SLJ specimens. These predictions were achieved without any nonphysical material inputs required from the end user because Turon's constraint is internally satisfied within the cohesive element formulation. The inclusion of progressive damage modeling methods in nonlinear finite element analyses often introduces a number of convergence related difficulties. For implicit analyses, the presence of the artificially high cohesive penalty stiffnesses in the global stiffness matrix often causes convergence problems. Likewise, the usage of very high penalty stiffnesses in explicit analyses often leads to prohibitively short minimum stable time increments. The decoupling of the physical and penalty stiffnesses in the proposed formulation removes the penalty stiffness from both the element and global stiffness matrices, addressing both of these issues.

Part III

Concluding remarks

Chapter 7

Conclusions

In the initial part of this thesis, a new experimental data reduction method for the mixed mode characterization of adhesive joints has been presented. The proposed method has been used, along with other methods available in the literature, for two different purposes: firstly, to discuss the suitability of the existing methods to characterize adhesive joints in FRP and, secondly, to perform an experimental campaign for characterizing the effect of the mode mixture and the adhesive and adherends thicknesses on the fracture behavior of adhesive joints. In the second part of the thesis, the open challenges of existing cohesive element formulations for the simulation of interlaminar failure have been identified and discussed. A new cohesive element formulation has been proposed that faces some of the challenges identified.

The experimental data reduction method presented in Chapter 2 enables the characterization of large-scale fracture in adhesive joints by means of the MMB test. The proposed method has been verified in a delamination test campaign of AS4/8552 carbon/epoxy laminates against the LEFM-based results given by the method in the ASTM standard. The new method has been shown to provide accurate results with deviations of less than 7% compared to the LEFM-based method of the standard and, at the same time, it has been shown to not only require less input information, but also to have a wider range of applicability and to provide results with lower uncertainty. Unlike LEFM-based methods, the proposed method does not require the characterization of the elastic properties of the material or the testing machine compliance calibration. Crack length

monitoring or its estimation are also avoided. Instead, four rotation angles at load introduction points have to be measured, which can be done in real time. The measurement of the rotation angles is more suitable than crack length monitoring in those situations involving large fracture process zones, such as the characterization of adhesively bonded joints, where the position of the crack tip cannot be identified because of the fracture process zone length.

An experimental test campaign of the fracture toughness behavior of an FM-300 epoxy film adhesive in T800S/M21 carbon/epoxy adherends has been conducted. The results of this test campaign have been used in Chapter 3 to evaluate the suitability of LEFM-based data reduction methods for the characterization of adhesive joints. To do so, LEFM results have been compared to the results obtained by means of J-integral-based methods. The results given by LEFM-based data reduction methods have been shown to be heavily dependent on the length of the fracture process zone, presenting an increasing overestimation of the fracture toughness that ranges from 10% to 40% as the fracture process zone grows. Those geometries that imply larger fracture process zones, such as specimens with thicker adherends, result in the most substantial disagreement between LEFM and J-integral results. Similarly, larger differences between LEFM and the J-integral are observed under mode II with respect to mode I, as mode II generally involves larger fracture process zones. LEFM has been argued as not being suitable for the analysis of adhesive joints fracture, being early stages of crack growth the only scenario where LEFM could be expected to provide a reasonable estimation of the initiation fracture toughness.

In view of the previous conclusion, J-integral-based experimental data reduction methods have been used in Chapter 4 for measuring the fracture toughness and the cohesive law of the FM-300 epoxy film adhesive. The effect of the mode mixture and the adhesive and adherend thicknesses on both the fracture toughness and the cohesive law of the adhesive have been studied. DCB and ENF tests were performed for the characterization of pure modes I and II, respectively, and MMB tests were conducted for mixed mode, in conjunction with the experimental method proposed in Chapter 2. It has been observed that thinner specimens result in a higher fracture toughness of the joint for all the loading modes tested, although this ten-

dency is less marked for mixed mode loading. Similarly, thicker adhesive layers result in higher bond toughness under pure mode, whereas the differences are also less pronounced under mixed mode. These observations have been argued to be in agreement with other experimental and numerical works in the literature. The shape of the measured cohesive laws has been shown to be mainly defined by the mode mixity: failure is more brittle under mode I, whereas plasticity prior to damage progressively increases as the percentage of mode II increases. The remaining tractions that the interface is able to sustain are zero for mode mixtures of 50% and below and increase for high percentages of mode II, which can be explained by friction in the fractured interface. The effect of the adhesive and adherend thicknesses is also reflected in the measured cohesive laws. However, such an effect is modest compared to the influence of the mode mixity and its quantification is on the threshold of the existent experimental measurement capabilities. The limitations that still exist in the measurement of cohesive laws have been evidenced and discussed.

With regard to the simulation of adhesive joints by means of cohesive zone models, in Chapter 5 an assessment of three different cohesive element formulations in terms of energy dissipation under mixed mode has been undertaken. It has been shown that, under certain circumstances, some formulations do not correctly predict the amount of energy dissipated, which entails a lack of accuracy in the simulation results. It has been observed that the source of such erroneous energy prediction is not the computation of the mixed mode ratio, but rather the fact that the consistency of the cohesive element formulation depends on the mixed mode interpolation criterion used. The energy dissipation is correctly captured when a linear interpolation criterion in a $\mathcal{G}_I$ - $\mathcal{G}_{II}$ space is used, but it is not if the Benzeggagh-Kenane criterion is employed. However, for the cohesive element formulation proposed by Turon et al. [71, 88], a proper energy dissipation is ensured using the Benzeggagh-Kenane criterion and under any changing mixed-mode loading conditions, provided that an additional constraint that relates the interface properties is fulfilled. This constraint can be fulfilled by adjusting the penalty stiffness, which is a numerical parameter in zero-thickness cohesive elements, as a function of the properties of the interface.

The need to fulfill an additional constraint has been argued in Chapter 6 as being a limitation for the simulation of adhesive joints. The interface thickness needs to be modeled by means of finite-thickness cohesive elements, for which the interface stiffness is no longer a numerical penalty stiffness but the actual stiffness of the adhesive. In that context, the aforementioned constraint imposes a relationship between actually measurable interface properties and is not generally fulfilled. In Chapter 6, a new cohesive element formulation that overcomes this issue has been proposed. The proposed formulation relies on the decoupling of the interface penalty stiffness and the physical adhesive stiffness by considering a zero-thickness interface embedded within a linear-elastic adhesive. The proposed model has been validated against experimental data for DCB, ENF and MMB tests, which are the tests used to provide the material properties that feed the model, and for SLJ tests, for which a good agreement between the numerical and experimental results is obtained for varying adhesive thicknesses. The simulation results of the SLJ test are obtained without any nonphysical material inputs or any further calibration of the model.

Chapter 8

Suggestions for future research

8.1 J-integral experimental methods

Further research could be devoted to the development of J-integral-based experimental data reduction methods for the characterization of adhesive joints or any other large-scale fracture processes, including:

- ▷ Extending the existing J-integral closed-form solutions to large displacements and finite strains, which would allow the characterization of any material configuration entailing large deformations.

- ▷ Extending the existing J-integral closed-form solutions so they can be used in bimaterial interfaces, which would enable the characterization of adhesive joints in composite laminates made of dissimilar materials or layups.

- ▷ Applying J-integral methods to the characterization of the fatigue behavior of interfaces, as J can easily be monitored in real time and the test can be performed under constant J or ΔJ instead of load or displacement control.

- ▷ Developing the tools and procedures required to standardize the use of J-integral-based methods, which would allow large-scale testing on an industrial level.

8.2 Cohesive law measurement method

Certain limitations have been identified regarding the method used for measuring cohesive laws. It would be desirable to adapt the method in order to be able to measure the cohesive law not only during the formation of the fracture process zone, but also during any stage of crack growth. This would prevent the results from being conditioned by the heterogeneity or defects generated at the insert tip during the manufacturing process, e.g. resin pockets or material inclusions. It would also allow the study of the evolution of the cohesive law of the material as the crack grows.

8.3 Experimental characterization of adhesive joints

Further research could be conducted in the experimental investigation of adhesive joints fracture, such as:

- The characterization of environmental effects on adhesive joints fracture, which can be readily done by following the procedure outlined in this thesis.

- The characterization of viscoelastic effects of the adhesive, also by following a similar procedure to that of this thesis.

- Characterization of the fracture process zone at a microscale level by means of, for instance, a microscopic digital image correlation system. This would engender a clear understanding of the macroscopic observations with regard to the cohesive law, fracture toughness and mixed-mode fracture of the material.

- The study of the mixed mode-fracture of adhesive joints on a microscale level or, in other words, studying the fracture process zone in terms of mode mixity. Experimental evidence on this topic, albeit still missing, should determine how the mixed-mode ratio is defined in the numerical models that pursue the simulation of mixed-mode fracture.

8.4 Numerical simulation of adhesive joints

Some of the previously mentioned effects that could be further characterized can also be easily accounted for in the proposed cohesive element formulation. For instance, the adhesive elastoplastic or viscoelastic behavior can be accounted for by replacing Equations (6.9) and (6.10) with certain functions that should be defined from the experimental observations.

A reformulation of the cohesive zone model to account for the cohesive law shape evolution as a function of the mode mixity would be desirable. This would allow the experimental measurements to be directly incorporated into the numerical model and to reliably reproduce the fracture process zone behavior. In addition, further research on the incorporation of the experimentally investigated local mode mixity variation into the numerical models is still required.

It would be worth developing a finite-thickness cohesive element that independently encapsulates both the elastoplastic behavior of the bulk adhesive and its fracture process. This could be achieved by implementing a phantom-node-based formulation. The use of the phantom node method would enable the independent integration of the bulk adhesive and the interface, therefore suppressing the stress equivalence assumption made in the formulation of the cohesive model presented in this work. This in turn would overcome the computational adhesive thickness limitation of the model and would allow the independent simulation of plasticity and interface fracture in the adhesive without a significant increase in the computational effort.

Finally, significant research still needs to be devoted to reducing the computational effort associated to cohesive element modeling in order to further extend their use to an industrial framework where the element size requirements are very restrictive.

Part IV

Appendices

Appendix A

Published paper

Published paper

C. Sarrado, A. Turón, J. Renart, I. Urresti. “Assessment of energy dissipation during mixed-mode delamination growth using cohesive zone models”

AMADE, Polytechnic School, University of Girona, Campus Montilivi s/n, 17071 Girona, Spain

Ikerlan S. Coop., M. Arizmendiarrieta 2, 20500 Arrasate, Spain

Received 2 March 2012, Revised 5 July 2012, Accepted 9 July 2012, Available online 24 July 2012

http://dx.doi.org/10.1016/j.compositesa.2012.07.009

http://www.sciencedirect.com/science/article/pii/S1359835X12002102

Abstract

The use of cohesive elements to simulate delamination growth involves modeling the inelastic region existing ahead of the crack tip. Recent numerical and experimental findings indicate that the mixed-mode ratio varies at each material point within the inelastic region ahead of the crack tip during crack propagation, even for those specimens whose mixed-mode ratio is expected to be constant. Although the local variation of the mode mixity may adversely affect the predicted numerical results, most existing formulations do not take it into account. In this work, the mode-decomposed *J*-integral is implemented as a finite element post-processing tool to obtain the strain energy release rates and the mixed-mode ratio of the inelastic region as a whole, allowing the assessment of crack propagation in terms of energy dissipation and mixed-mode ratio computation. Different cohesive elements are assessed with this method.

Keywords

- B. Delamination;
- B. Fracture;
- C. Damage mechanics;
- C. Numerical analysis

[9] Sarrado C, Turon A, Costa J, Renart J. On the validity of linear elastic fracture mechanics methods to measure the fracture toughness of adhesive joints; 2015. Under review.

[10] Sarrado C, Turon A, Costa J, Renart J. An experimental analysis of the fracture behavior of composite bonded joints in terms of cohesive laws; 2015. Under review.

[11] Sarrado C, Turon A, Renart J, Costa J. Effect of adherend and adhesive thickness on the fracture thoughness and cohesive law of FM300 adhesive. In: 7th International Conference on Composites Testing and Model Identification (Comptest 2015). 2015,.

[12] Sarrado C, Turon A, Costa J, Renart J. Caracterizacin del efecto de los grosores de adherente y adhesivo en la fractura de uniones adhesivas. In: XI Congreso Nacional de Materiales Compuestos (Matcomp 2015). 2015,.

[13] Sarrado C, Turon A, Renart J, Urresti I. Assessment of energy dissipation during mixed-mode delamination growth using cohesive zone models. Composites Part A - Applied Science and Manufacturing 2012;43(11):2128–36.

[14] Sarrado C, Llanos I, Urresti I, Turon A. Reliability of cohesive zone models in terms of energy dissipation during mixed-mode delamination growth. In: 8th European Solid Mechanics Conference (ESMC 2012). 2012,.

[15] ABAQUS version 6.12: ABAQUS User's Manual, SIMULIA World Headquarters, 166 Valley Street, Providence, RI 02909, USA.; 2012.

[16] Sarrado C, Leone FA, Turon A. Finite-thickness cohesive elements for modeling thick adhesives; 2015. Under review.

[17] Leone FA, Sarrado C, Dávila CG, Girolamo D. Finite-thickness cohesive elements with physical stiffness properties. In: 1st International Conference on Mechanics of Composites. 2014,.

[38] Carlsson LA, Gillespie JW, Pipes RB. On the analysis and design of the end notched flexure (enf) specimen for mode-ii testing. Journal of Composite Materials 1986;20(6):594–604.

[39] Leffler K, Alfredsson KS, Stigh U. Shear behaviour of adhesive layers. International Journal of Solids and Structures 2007;44(2):530–45.

[40] Sørensen BF, Jorgensen K, Jacobsen TK, Ostergaard RC. DCB-specimen loaded with uneven bending moments. International Journal of Fracture 2006;141(1-2):163–76.

[41] Hogberg JL, Sørensen BF, Stigh U. Constitutive behaviour of mixed mode loaded adhesive layer. International Journal of Solids and Structures 2007;44(25-26):8335–54.

[42] Alfredsson KS, Hogberg JL. Energy release rate and mode-mixity of adhesive joint specimens. International Journal of Fracture 2007;144(4):267–83.

[43] Paris AJ, Paris PC. Instantaneous Evaluation of J and O-star. International Journal of Fracture 1988;38(1):19–21.

[44] Gunderson JD, Brueck JF, Paris AJ. Alternative test method for interlaminar fracture toughness of composites. International Journal of Fracture 2007;143(3):273–6.

[45] Nilsson F. Large displacement aspects on fracture testing with double cantilever beam specimens. International Journal of Fracture 2006;139(2):305–11.

[46] Stigh U, Alfredsson KS, Biel A. Measurement of cohesive laws and related problems. IMECE 2009: Proceedings of the ASME International Mechanical Engineering Congress and Exposition 2009;11:293–8.

[47] Huber O, Nickel J, Kuhn G. On the decomposition of the J-integral for 3D crack problems. International Journal of Fracture 1993;64:339–48.

[58] ISO 17025:2005, General requirements for the competence of testing and calibration laboratories, International Organization for Standardization, Geneva, Switzerland; 2005.

[59] Adams R, Coppendale J. Stress-strain behavior of axially-loaded butt joints. Journal of Adhesion 1979;10(1):49–62.

[60] Kinloch A, Shaw S. Fracture resistance of a toughened epoxy adhesive. Journal of Adhesion 1981;12(1):59–77.

[61] Daghyani HR, Ye L, Mai YW. Mode-l Fracture Behaviour of Adhesive Joints. Part I. Relationship Between Fracture Energy and Bond Thickness. Journal of Adhesion 1995;53(3-4):149–62.

[62] Pardoen T, Ferracin T, Landis C, Delannay F. Constraint effects in adhesive joint fracture. Journal of the Mechanics and Physics of Solids 2005;53(9):1951–83.

[63] Ikeda T, Yamashita A, Lee D, Miyazaki N. Failure of a ductile adhesive layer constrained by hard adherends. Journal of Engineering Materials and Technology, Transactions of the ASME 2000;122(1):80–5.

[64] Azari S, Papini M, Spelt J. Effect of adhesive thickness on fatigue and fracture of toughened epoxy joints - Part I: Experiments. Engineering Fracture Mechanics 2011;78(1):153–62.

[65] Wang R, Sinclair A, Spelt J. Strength of adhesive joints with adherend yielding: II. Peel experiments and failure criteria. Journal of Adhesion 2003;79(1):49–66.

[66] Marín L, Trias D, Badalló P, Rus G, Mayugo J. Optimization of composite stiffened panels under mechanical and hygrothermal loads using neural networks and genetic algorithms. Composite Structures 2012;94(11):3321–6.

[67] ISO 25217:2009, Adhesives – Determination of the mode 1 adhesive fracture energy of structural adhesive joints using double cantilever

beam and tapered double cantilever beam specimens, International Organization for Standardization; 2009.

[68] ASTM D7905/D7905M-14, Standard Test Method for Determination of the Mode II Interlaminar Fracture Toughness of Unidirectional Fiber-Reinforced Polymer Matrix Composites, American Society for Testing and Materials; 2014.

[69] Harper P, Hallett S. Cohesive zone length in numerical simulations of composite delamination. Engineering Fracture Mechanics 2008;75(16):4774–92.

[70] Soto A, González E, Maimí P, Turon A. Cohesive zone length of orthotropic materials under delamination; 2015. To be submitted.

[71] Turon A, Camanho PP, Costa J, Renart J. Accurate simulation of delamination growth under mixed-mode loading using cohesive elements: Definition of interlaminar strengths and elastic stiffness. Composite Structures 2010;92(8):1857–64.

[72] Ji G, Ouyang Z, Li G, Ibekwe S, Pang SS. Effects of adhesive thickness on global and local mode-I interfacial fracture of bonded joints. International Journal of Solids and Structures 2010;47(18-19):2445–58.

[73] Ji G, Ouyang Z, Li G. Effects of bondline thickness on Mode-II interfacial laws of bonded laminated composite plate. International Journal of Fracture 2011;168(2):197–207.

[74] Ji G, Ouyang Z, Li G. Effects of bondline thickness on Mode-I nonlinear interfacial fracture of laminated composites: An experimental study. Composites Part B: Engineering 2013;47:1–7.

[75] Ji G, Ouyang Z, Li G. On the interfacial constitutive laws of mixed mode fracture with various adhesive thicknesses. Mechanics of Materials 2012;47:24–32.

[76] AITM 1.0006, Determination of Interlaminar Fracture Toughness Energy Mode II, Issue 2, Airbus Industrie Test Method; 1994.

[77] Breitzman T, Iarve E, Cook B, Schoeppner G, Lipton R. Optimization of a composite scarf repair patch under tensile loading. Composites Part A: Applied Science and Manufacturing 2009;40(12):1921–30.

[78] Pagano NJ, Schoeppner GA. Delamination of polymer matrix composites: problems and assessment. (Ed.) Kelly, A; Zweben, D. Oxford (UK); 2000.

[79] Tay T. Characterization and analysis of delamination fracture in composites: an overview of developments from 1990 to 2001. Applied Mechanics Review 2003;56:1–32.

[80] Krueger R. The virtual crack closure technique: history, approach and applications. Tech. Rep.; NASA/CR-2002-211628; 2002.

[81] Needleman A. A continuum model for void nucleation by inclusion debonding. Journal of Applied Mechanics-Transactions of the ASME 1987;54(3):525–31.

[82] Tvergaard V, Hutchinson JW. The relation between crack-growth resistance and fracture process parameters in elastic plastic solids. Journal of the Mechanics and Physics of Solids 1992;40(6):1377–97.

[83] Xu XP, Needleman A. Numerical simulations of fast crack-growth in brittle solids. Journal of the Mechanics and Physics of Solids 1994;42(9):1397–&.

[84] Mi Y, Crisfield MA, Davies GAO, Hellweg HB. Progressive delamination using interface elements. Journal of Composite Materials 1998;32(14):1246–72.

[85] Ortiz M, Pandolfi A. Finite-deformation irreversible cohesive elements for three-dimensional crack-propagation analysis. International Journal for Numerical Methods in Engineering 1999;44:1267–82.

[86] Alfano G, Crisfield MA. Finite element interface models for the delamination analysis of laminated composites: mechanical and computational issues. International Journal for Numerical Methods in Engineering 2001;50(7):1701–36.

[87] Camanho PP, Dávila CG, de Moura MF. Numerical simulation of mixed-mode progressive delamination in composite materials. Journal of Composite Materials 2003;37(16):1415–38.

[88] Turon A, Camanho PP, Costa J, Dávila CG. A damage model for the simulation of delamination in advanced composites under variable-mode loading. Mechanics of Materials 2006;38(11):1072–89.

[89] Pinho S, Iannucci L, Robinson P. Formulation and implementation of decohesion elements in an explicit finite element code. Composites Part A: Applied Science and Manufacturing 2006;37(5):778–89.

[90] Jiang W, Hallett SR, Green BG, Wisnom MR. A concise interface constitutive law for analysis of delamination and splitting in composite materials and its application to scaled notched tensile specimens. International Journal for Numerical Methods in Engineering 2007;69:1982–95.

[91] Harper PW, Sun L, Hallett SR. A study on the influence of cohesive zone interface element strength parameters on mixed mode behaviour. Composites Part A: Applied Science and Manufacturing 2012;43(4):722–34.

[92] ANSYS version 11.0: release 11.0 Documentation, ANSYS, Inc.; 2007.

[93] Owen D, Fawkes A. Engineering fracture mechanics: numerical methods and applications. Swansea, UK: Pineridge Press; 1st ed.; 1983.

[94] Zhu Y, Liechti K, Ravichandar K. Direct extraction of rate-dependent traction-separation laws for polyurea/steel interfaces. International Journal of Solids and Structures 2009;46(1):31–51.

[95] Janssen M, Zuidema J, Wanhill R. Fracture mechanics. Spon Press; 2nd ed.; 2004.

[96] Benzeggagh ML, Kenane M. Measurement of mixed-mode delamination fracture toughness of unidirectional glass/epoxy composites with

mixed-mode bending apparatus. Composites Science and Technology 1996;56(4):439–49.

[97] Turon A, Dávila CG, Camanho PP, Costa J. An engineering solution for mesh size effects in the simulation of delamination using cohesive zone models. Engineering Fracture Mechanics 2007;74(10):1665–82.

[98] Turon A, González E, Sarrado C, Maimí P. Accurate simulation of delamination growth under mixed-mode loading using cohesive elements with mode-dependent penalty stiffness; 2015. Under review.

[99] Airoldi A, Baldi A, Bettini P, Sala G. Efficient modelling of forces and local strain evolution during delamination of composite laminates. Composites Part B: Engineering 2015;72:137–49.

[100] Schellekens J, De Borst R. On the numerical integrations of interface elements. International Journal for Numerical Methods in Engineering 1993;36(1):43–66.

[101] Bažant Z, Oh B. Crack band theory for fracture of concrete. Matriaux et Constructions 1983;16(3):155–77.

[102] Girolamo D. Progressive Damage Analysis of Bonded Composite Joints. Master's thesis; Delft University of Technology; 2012.

[103] da Silva L, Rodrigues T, Figueiredo M, de Moura M, Chousal J. Effect of adhesive type and thickness on the lap shear strength. Journal of Adhesion 2006;82(11):1091–115.